UNIVERSITY OF OKLAHOMA

GRADUATE COLLEGE

UNDERSTANDING TYPE IA SUPERNOVA DIVERSITY WITH PHOENIX

A DISSERTATION

SUBMITTED TO THE GRADUATE FACULTY

in partial fulfillment of the requirements for the

Degree of

DOCTOR OF PHILOSOPHY

By

JAMES M DERKACY
Norman, Oklahoma
2022

UNDERSTANDING TYPE IA SUPERNOVA DIVERSITY WITH PHOENIX

A DISSERTATION APPROVED FOR THE
HOMER L. DODGE DEPARTMENT OF PHYSICS AND ASTRONOMY

BY THE COMMITTEE CONSISTING OF

Dr. Edward Baron, Chair

Dr. Trina Hope

Dr. Nathan Kaib

Dr. Michael Struass

Dr. John Wisniewski

Acknowledgements

Good science does not happen in a vacuum. It is only possible through the support of family, friends, colleagues, and collaborators that we can produce our best work.

To my family – Thank you for creating an environment where my natural curiosity about the world around me was developed and nurtured and for all the love and support you have given me.

To Eddie – Thank you for welcoming me into your research group and for providing me the opportunities to develop into the scientist I am today, and for demonstrating how to be a mentor and researcher who cares just as much about the scientist as their scientific output.

To my committee – Thank you Nate, John, Mike and Trina for helping to guide me through the ups and downs of earning this degree, and for your examples of how to be great mentors and researchers.

To the SNNRT group – Thank you, everyone from the faculty (David) and post-docs (Dre and Vera), to the students both graduate (Jeremy, Malia, Lisa, Sarah, and Anthony) and undergraduate (Patrick, London, Zach, Sara, and many others) for for being such a wonderful group of people to work with and learn from, and for listening to the same practice talks over and over for the last two years.

To my collaborators – Thank you to everyone for their support and assistance in helping to put together the works that comprise this dissertation. Special thanks to Peter Brown, Peter Hoeflich, and Lifan Wang for their guidance and support over the last several years. Thank you to all of the POISE members, including Chris A, Chris B, Lluis, Eric, Kevin, Sahana, Jing, Nidia, Mark, Tony, Abi, Melissa, Ben, Max, Nick, and Shuvo for creating such a vibrant and welcoming collaboration, and without whom this work would not be possible.

To my friends and classmates – Thank you all for making the struggles of grad school enjoyable. I'm forever grateful for the late nights and weekends spent solving problems, conversations over tea and cookies, and general office shenanigans that occurred when we just needed to let loose. I couldn't have made it through without all of you.

Contents

Abstract

Type Ia Supernovae (SNe Ia) are important astrophysical objects. They produce roughly half of the iron group elements found in the universe, the energy they release drives the evolution of galaxies, and their high intrinsic luminosities allow them to be seen across cosmological distances. Through the width-luminosity relation (often called the Phillips relation), they can be used as "standardizable candles" to serve as cosmological distance indicators and were instrumental in the discovery of the accelerating expansion rate of the universe. However, despite decades of detailed study, many fundamental questions about these objects remain; including the exact nature of their progenitor systems and the mechanism(s) by which they explode.

UV spectra are unique probe of SNe Ia physics and their evolution in throughout the history of the universe, as much of the information about the properties of the progenitor star and the explosion mechanism are encoded in the outer layers of the ejecta; a region that ultraviolet spectra probe at later times than the optical. The ultraviolet properties of SNe Ia are much more diverse than in the optical and near infrared, and may vary with redshift. The ultraviolet properties of SNe Ia have the ability to help us unlock their true nature; but have historically been under-studied due to difficulties in obtaining observations in this wavelength regime. However, recent growth in the data sets of SNe Ia observed with the *Hubble Space Telescope* and the Neil Gehrels Swift Observatory (*Swift*), have illuminated the need for detailed modeling of this region in order to perform the differential comparisons necessary to further our understanding of these objects and improve their use as cosmological distance indicators.

In Part I, I discuss the theoretical foundations of this work. I briefly review the important aspects of spectral formation in the ultraviolet of SNe Ia, and introduce the two codes (`SYNOW` and `PHOENIX`) used to generate synthetic spectra of SNe Ia. I apply the spectra generated from these codes to the UV spectra of SN 2011fe and for the first time make line identifications in all the major ultraviolet features near maximum light, including the first ever identifications of C IV and Si IV in a SNe Ia spectrum. Then, using the suite of `PHOENIX` models, I explore the impact of luminosity variations on the ultraviolet spectra and discuss the connections I find between the ultraviolet and other wavelength regimes.

In Part II, I shift focus and discuss how differential comparisons in observational studies can further our understanding of SNe Ia. Chapter 4 details the science cases behind nearly five years of observations using the Astrophysical Research Consortium 3.5-m telescope at Apache Point

Observatory, including highlighting instances where my observations contributed to the advancement of our understanding of the underlying physics of all types of supernovae and their progenitors. Chapter 5 focuses on SN 2021fxy, a Type Ia supernovae observed extensively in multiple wavelength regimes by the Precision Observations of Infant Supernovae (POISE) collaboration, for which ultraviolet spectra were obtained with the *Hubble Space Telescope*. In comparing SN 2021fxy to the broader sample of spectroscopically normal SNe Ia with ultraviolet spectra from *HST*, I show that mid-ultraviolet flux suppression is a common feature of SNe Ia and discuss possible mechanisms that cuase this flux suppression and how they may be connected to different progenitors and explosion mechanisms. Additionally, I show that SN 2021fxy is substantially similar to another SN Ia with mid-ultraviolet suppression, SN 2017erp, and illustrate how luminosity variations between the two SNe Ia may be responsible for the observed flux differences between them.

CHAPTER 1

Introduction

Supernovae (SNe) are the cataclysmic endpoint of the life cycle of many stars. As cauldrons of nucleosynthesis, the elements created in their explosions chemically enrich the surrounding interstellar medium, and the explosions themselves help drive the evolution of the galaxies that host them. The importance of supernovae to astronomy is further enhanced by the ability to use supernovae as "standardizable candles", allowing them to serve as distance indicators across cosmological distances. The use of Type Ia supernovae (SNe Ia) for this purpose revealed the accelerating rate of expansion of the universe (Riess et al., 1998; Perlmutter et al., 1999). Recent studies have also explored using Type II supernovae (SNe II) for the same purpose (de Jaeger et al., 2017; Gall et al., 2018b).

1.1. The Diversity of Supernovae

Astronomical transients are primarily classified based upon their optical spectral properties; as different progenitor systems result in different combinations of elements appearing in the spectra. For supernovae, Figure 1.1 shows a simplified decision tree useful for distinguishing between the different types. First, one examines the spectra for hydrogen features, where upon the supernova is categorized as either a Type I (historically called hydrogen poor) or Type II (hydrogen rich) supernova. If the supernova is a Type I, it can be further classified based on the presence of silicon in its spectra, with SNe I with strong silicon features categorized as Type Ia SNe. Type I supernovae lacking strong silicon lines are further categorized based on the presence of helium lines in the spectra into Types Ib (helium rich), and Type Ic (helium poor). However, as observational samples sizes have continued to grow, evidence has shown that it is often difficult to distinguish between Type Ib and Ic SNe; therefore, they are often referred to collectively as Type Ib/c or stripped envelope supernovae (SESN). For SNe II, further classification requires time series photometry and spectroscopy. Example spectra for the various SNe types are shown in Figure 1.2. Brief summaries of the various types of SNe and the physics that govern their behavior can be found below. For a general overview of all types of supernova see Branch & Wheeler (2017).

1.2. Type Ia (Thermonuclear) Supernovae

Type Ia supernovae (SNe Ia) are the thermonuclear explosions of white dwarfs (WD) in a binary star systems.

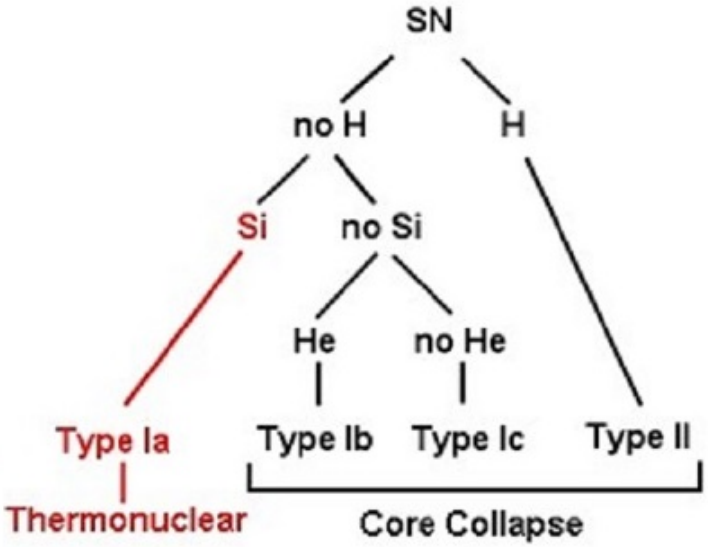

Figure 1.1: Basic decision tree for the spectral typing of supernovae.

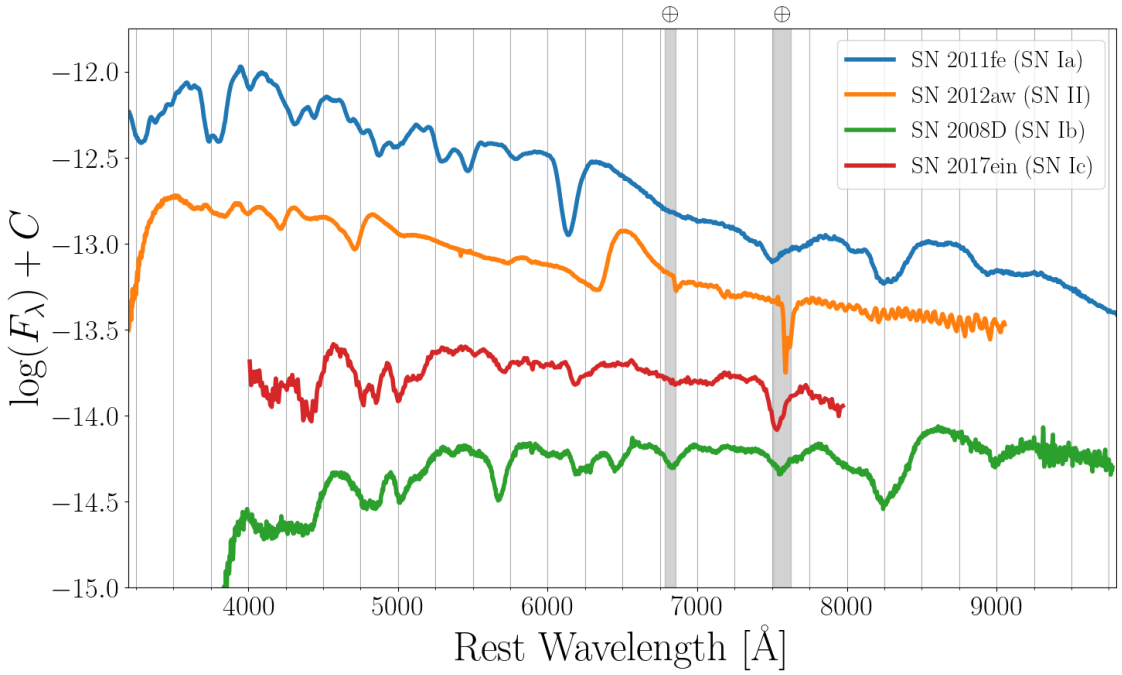

Figure 1.2: Example spectra of different supernova types near maximum light. References: SN 2011fe (Mazzali et al., 2014), SN 2017ein (Teffs et al., 2021), SN 2008D (Modjaz et al., 2009), SN 2012aw (Dall'Ora et al., 2014).

1.2.1. Photometric Properties

To first order, the light curve decay of a Type Ia supernova can be described by the nuclear decay chain of ^{56}Ni $\rightarrow$ ^{56}Co $\rightarrow$ ^{56}Fe, as described by the analytic solutions of Arnett (1982). Early time evolution of the light curve can be modeled by the "expanding fireball" hypothesis, which assumes a photosphere of constant temperature for a few days as the supernova ejecta expands homologously ($v = rt$) until the outer layers become optically thin.

Around maximum light, the $B - V$ colors of SNe Ia are approximately 0. However, as the supernova evolves it becomes redder, peaking roughly 30 days after max light before the color becomes bluer again as the supernova transitions to the nebular phase (Lira et al., 1998; Burns et al., 2011). Similar color relationships can be constructed for other combinations of bands, which can be used to help estimate the reddening of the supernova by the host galaxy (Burns et al., 2014). It is unknown however, if these relationships prefer one progenitor or explosion model over another as the true intrinsic colors of Type Ia's are still undetermined.

The most important quantity derived from photometric observations of Type Ia's is the decline rate of the light curve in the 15 days post maximum light in the B-band, or $\Delta m_{15}(B)$. This parameter is related to the mass of radioactive ^{56}Ni present within the supernova ejecta and is useful in standardizing the light curves of SNe Ia through the empirical Phillips (or width-luminosity) relation (Nugent et al., 1995; Höflich, 1995). Phillips (1993) found that SNe Ia with larger $\Delta m_{15}(B)$ were intrinsically brighter and bluer and that SNe Ia with smaller $\Delta m_{15}(B)$ were dimmer and redder at maximum light. Combined with measurements of other light curve parameters, $\Delta m_{15}(B)$ also allows for the standardization of the light curves for use as cosmological standard candles (Guy et al., 2005). While the Phillips relation can explain some of the variance between SNe Ia light curves arising from differences in the amount of ^{56}Ni synthesized in the explosion, it is unable to explain all of the observed diversity in SNe Ia, especially among their spectra.

1.2.2. Spectral Properties

SNe Ia are primarily identified by their lack of hydrogen features and the presence of strong silicon lines in their near maximum light spectra. In more sophisticated analyses, SNe Ia are defined by the presence of other so-called Intermediate Mass Elements (IME's) such as O, Ca, Mg, and S near maximum light. At later phases, they are dominated by iron group elements (IGE's) like Fe, Co, and Ni; in particular lines of Fe II and Fe III. It is from this time variation of the dominant spectral features that we know Type Ia supernova consist of a layered ejecta with the lighter IMEs primarily comprising the outer layers, while the heavier IGEs generally reside in the ejecta core. Some mixing of these elements must occur within the ejecta (likely during the turbulent nuclear burning phases just prior to explosion), as the transitions between the IME and IGE dominant phases occur smoothly as the photosphere of the supernova retreats farther into the ejecta.

Despite the apparent relative uniformity of SNe Ia, analyses of small variations in the shapes and strengths of features in large samples of SNe Ia have yielded surprising results about the diversity of Type Ia supernova. The Branch diagram uses the pseudo-equivalent widths of the Si II $\lambda 5972$ and $\lambda 6355$ to subdivide the sample into four groups which show similar properties when fit with the SYNOW code (Branch et al., 2006). The four groups are:

1. Core-normals (CN) - The proto-typical Type Ia SN, CN's defined primarily by the almost identical Si II $\lambda 6355$ feature on top of their otherwise homogeneous spectra. Each CN is well fit by a photospheric velocity of $\sim 12,000$ km s^{-1} and excitation temperatures near 10,000 K near max light.

2. Broad Lines (BL) - Broad lines are similar to core normals, except that their Si II $\lambda 6355$ lines are much broader and deeper, placing them farther to the right on the Branch Diagram. These features may appear broader due to the burning front extending to higher velocities in the ejecta than in CNs.

3. Cools (CL) - Cools have a characteristic large absorption between 4000-4400 Å due to the presence of Ti II lines, which increase in strength with lower temperatures at the photosphere. Cools are also less luminous than core-normals as well. The proto-typical cool SNe Ia is SN 1991bg.

4. Shallow Silicons (SS) - A self-explanatory name, the SS show shallower absorptions in the Si II $\lambda 5972$ and $\lambda 6355$ lines than the CNs. The SS's also have higher photospheric temperatures than core normals too. SN 1991T is the prototypical supernova of this class, but recent work has shown 1991T to be an extreme example of the class (M.M. Phillips et al., in prep).

Example spectra for the various Branch groups can be found in Figure 1.3. More recent works have shown that these initial groups are statistically robust, and may be related to differences in the underlying progenitor or different explosion mechanisms, which may form a continuum of SNe Ia properties instead of distinct sub-groups (Branch et al., 2006; Polin et al., 2019; Burrow et al., 2020).

1.2.3. Progenitor Scenarios

Using the knowledge gleaned from the spectral and photometric features of SNe Ia, the thermonuclear explosion of a carbon/oxygen (C/O) white dwarf was first proposed as a possible progenitor by Hoyle & Fowler (1960).

Modern models of SNe Ia are primarily permutations of a few different progenitor scenarios (single or double degenerate) and explosion mechanisms (detonation-to-deflagration transition,

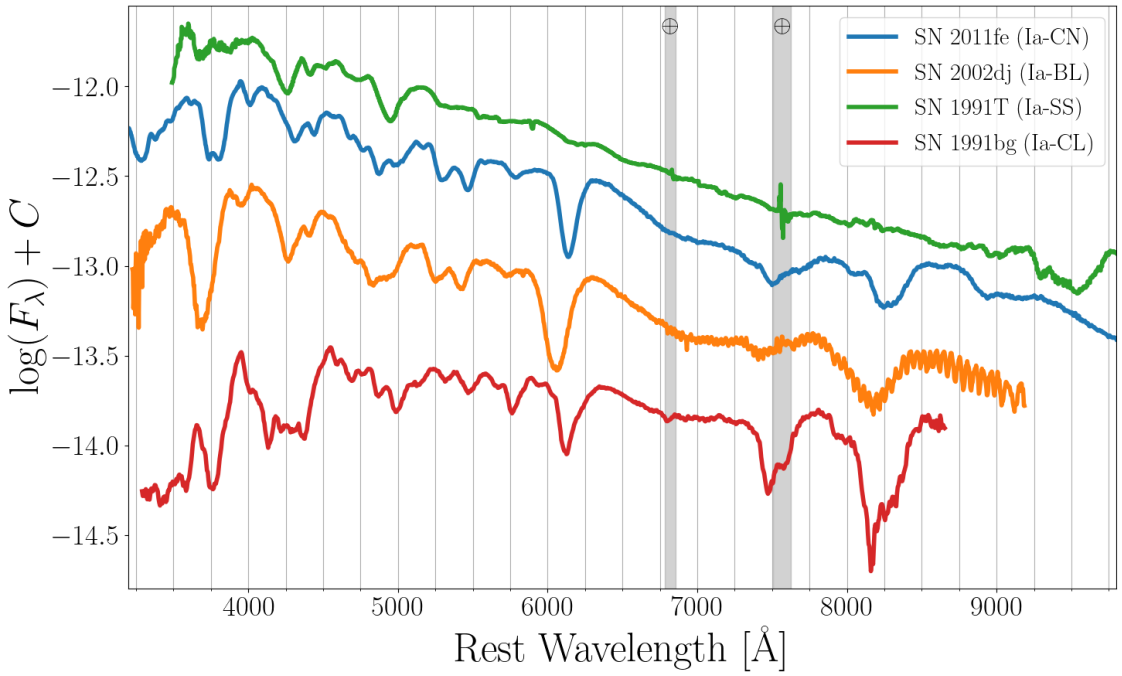

Figure 1.3: Example spectra showing the the distinctions between the different Branch groups.

double detonation, mergers, etc.). We briefly review some of the more successful models and their ability to replicate the observed SNe Ia diversity below.

1.2.3.1. Single Degenerate Scenario

The canonical model of the single degenerate scenario was first laid out in Whelan & Iben (1973). In this scenario, a binary system has evolved to the point where the more massive primary star has evolved into a massive white dwarf, and the less massive secondary star has evolved into a red giant star (RG). Through Roche Lobe overflow or a steady wind, the secondary star begins to transfer its mass back onto the primary star. As the mass of the primary approaches the Chandrasekhar mass (M_{ch} = 1.4 $M_{\odot}$), explosive carbon burning begins, which releases enough energy to unbind the star and create the supernova explosion.

However, the non-degenerate companion star need not be a red giant, as simply altering the orbital properties of the close binary system allows for a main sequence, a subgiant, or a He-star to accrete material onto the primary WD though Roche Lobe overflow or via a wind. Observational signatures of a SD progenitor scenario are expected to be detectable as narrow emission due to the interaction between companion star and its wind with the supernova ejecta (Maeda et al., 2014; Kutsuna & Shigeyama, 2015) or as hydrogen lines buried deep within the ejecta through material stripped from the companion during an interaction with the ejecta (Marietta et al., 2000; Kasen, 2010).

In the latter case, the interaction between the supernova ejecta and the companion star should produce a detectable bump in the early light curve. Simulations have indicated that the size of this bump is dependent on the observer's viewing angle, although the directionality of this dependence is unclear and detectability of the bump is debated (Kasen, 2010; Maeda et al., 2014; Kutsuna & Shigeyama, 2015). Some evidence of early excess emission has been detected in several SNe Ia, including SN 2017cbv (Hosseinzadeh et al., 2017), SN 2018oh (Li et al., 2019; Shappee et al., 2019; Dimitriadis et al., 2019), and SN 2021aefx (Ashall et al., 2022) although its origins are debated (Piro & Morozova, 2016; Dimitriadis et al., 2019; Shappee et al., 2019)

The first attempts at modeling the SN Ia explosion came in the form of the highly parameterized W7 model (Nomoto et al., 1984; Thielemann et al., 1986). W7 assumes a 1.0 $M_\odot$ WD accreting mass from its companion star at a rate greater than $\dot{M} \geq 4 \times 10^{-8}$ $M_\odot$ yr^{-1}, where the WD gains mass through frequent H/He flashes. Once the WD reaches the Chandrasekhar mass, central carbon burning begins in the form of a subsonic flame front, known as a deflagration. As the deflagration propagates outwards, the WD expands preventing complete burning throughout the entire star, which would leave only ^{56}Ni and He, instead resulting in the necessary IGE core surrounded by IMEs in the outer layers. The total yield of ^{56}Ni is between 0.5 $M_\odot$ and 0.7 $M_\odot$; sufficient to reproduce the observed light curves. However, in order for W7 to properly reproduce the observed near-max light spectra, mixing near the burning boundaries must occur.

More modern SD channel models often employ a "deflagration-to-detonation" (DDT) transition at a prescribed transition density in order to achieve the proper distribution of elements in the ejecta (Hoeflich et al., 1995, 2017). Recently, success in replicating this DDT transition both computationally and in the lab have shown a DDT to be a viable mechanism for triggering SNe Ia (Poludnenko et al., 2019).

1.2.3.2. Double Degenerate Scenario

The double degenerate (DD) scenario was simultaneously proposed by Iben & Tutukov (1984) and Webbink (1984), and is designed to address several short comings of the SD scenario. In the DD scenario, a close binary system evolves through several periods of mass transfer and common envelopes phases until a binary system of WDs with a total mass larger than the Chandrasekhar mass remains. Then, the orbit of the binary system decays via gravitational wave radiation before the two stars eventually merge and explode in a Type Ia SN.

Unlike the SD channel, DD progenitors do not require that the primary WD equal the Chandrasekhar mass. Thielemann et al. (1986) found that in WD's more massive than 1.1 $M_\odot$ surface helium detonations are strong enough to drive shockwaves to the core of the WD strong enough to ignite the central carbon. Rotationally supported WD's larger than the Chandrasekhar mass may exist for $\sim 10^7$ years after a merging event (assuming solid body rotation) until magnetic dipole

radiation slows the star's rotational period and core collapse ensues (Meng & Podsiadlowski, 2013). This range of scenarios allows for the same progenitor channel to easily reproduce both super and subluminous SNe Ia.

Another variation was the so-called double-detonation or edge lit scenario, where a sub-Chandrasekhar progenitor develops a helium shell (Livne & Glasner, 1990, 1991; Tutukov et al., 1992; Woosley & Weaver, 1994; Hoeflich & Khokhlov, 1996). In this model, when the helium shell reaches a mass of about 0.1 $M_\odot$, the helium detonates, driving a compression wave to the center of the C/O white dwarf, igniting its detonation. However, these models showed spectra that were far too blue (Hoeflich & Khokhlov, 1996; Nugent et al., 1997) as well as the possibility that they would create novae instead of supernovae (Yoon & Langer, 2004).

The most recent set variations of sub-Chandrasekhar mass SNe Ia via the "dynamically driven double-degenerate double-detonation" (or D6) model can accurately reproduce the observed spectroscopic and photometric properties of SNe Ia (Shen et al., 2018; Polin et al., 2019). In their models, Shen et al. (2018) find that a helium WD donor star can donate a small amount of mass during the merger process that will detonate on the surface, driving shocks inwards to the core of the WD igniting an off-center detonation which unbinds the star in a SNe Ia. In order to prevent complete burning, throughout the star a piecewise density profile is adopted that is similar to W7 in the outer layers, but with constant density cores. The insight here over the double detonation models is that helium ignition can occur via $^{12}C(\alpha,\gamma)^{16}O$, which is much faster than the triple alpha process.

Lower mass DD models are unable to completely burn their inner regions to nuclear statistical equilibrium, and therefore produce too few IGE's and too many IME's. WD's with an initial mass greater than or equal to 1 $M_\odot$ are able to produce the 0.56 $_\odot$ of ^{56}Ni, roughly what is necessary to replicate the light curve of a "normal" SN Ia, and approximately reproduce the observed velocity distribution of these elements. A non-insignificant amount of helium is produced in the core of the more massive models that might be detectable in nebular phase spectra, providing an important observational test for these models. This surface helium detonation also produces radioactive elements at the surface, which alter the observed light curve and colors at early times (Polin et al., 2019). The off-center detonations produce asymmetric ejectas, which require certain viewing angles in order to reproduce observed spectra (Shen et al., 2021).

Another variation of the double degenerate scenario is the so called violent merger scenario, first proposed by Rosswog et al. (2009). In this scenario, WDs in a dense stellar environment like a globular cluster have an increased chance of colliding with each other. During a collision, shock compression is strong enough to ignite the central carbon in the WD and produce a SNe Ia. Collisions between equal mass WD's of 0.9 $M_\odot$ were found to produce roughly the right amount of ^{56}Ni to reproduce normal SNe Ia. Mergers of WD's with masses as low as 0.6 $M_\odot$ could potentially reproduce some subluminous SNe Ia. This scenario does however introduce significant viewing

angle effects, as simulations show material escapes the system perpendicular to the impact surface and creates large asymmetries within the ejecta.

More recent works by Pakmor et al. (2010) and Pakmor et al. (2012) examined the situation where more massive, non-equal mass WD's merge violently. In these systems, the less massive WD is heavily disrupted and the primary rapidly accretes its matter over the course of a few orbital periods. This rapid accretion creates hot spots within the WD that trigger detonations before the stars have fully merged. Violent mergers of two WD's with ~ 0.9 $M_\odot$ masses are able to replicate the colors and spectra of subluminous explosions like SN 1991bg, although a merger involving He WD where the primary is still roughly 0.9 $M_\odot$ may be able to better reproduce the light curves without impacting the spectra (Pakmor et al., 2013). Meanwhile mergers of 1.1 $M_\odot$ and 0.9 $M_\odot$ WD's binaries are necessary to recreate normal Ia's (Pakmor et al., 2012). Both sets of models still have non-negligible viewing angle effects, but the overall asymmetry of the ejecta is lower, better matching the observed characteristics of Type Ia's (Patra et al., 2022).

1.2.3.3. Core Degenerate Scenario

The core-degenerate (CD) scenario, first proposed by Ilkov & Soker (2012) can be thought of as a middle ground between the SD and DD progenitor systems. In the CD scenario, the system evolves similarly to the DD system until the second common envelope phase. During this phase, it is suggested that the core of the secondary AGB star merges with the primary WD to create a Chandrasekhar mass or super-Chandrasekhar mass WD, which can be rotationally supported to achieve the necessary delay time distribution for SNe Ia. During the time that the WD is rotationally supported, the remaining envelope of the AGB star is dispersed as needed to allow for any potential CSM interactions.

To date, no detailed hydrodynamic or radiative transfer simulations have been performed studying the evolution of these systems to verify if they can in fact reproduce the observed properties of SNe Ia. However, the CD scenario remains an plausible, yet unproven theory on the origins of SNe Ia, and may show particular promise in explaining the small number of SNe Ia which show distinct signs of interaction with nearby H-rich CSM, including PTF-11kx (Soker et al., 2013).

1.3. Core-Collapse Supernovae

Core collapse supernovae (CC-SNe) are stellar explosion of massive stars ($M \gtrsim 8$ $M_\odot$) due to the inability of a star's core to support itself against gravitational collapse. In most cases, this collapse occurs because the star has successfully fused the fuel in its core all the way to iron, which cannot be fused to higher elements, and therefore is unable to produce the radiative pressure necessary to prevent gravitational collapse when the core of the star exceeds the Chandrasekhar mass ($M_{ch} = 1.4$ $M_\odot$). More exotic methods of triggering this gravitational collapse are rare, but

possible. This includes the "electron capture" process, where the degenerate O/Ne/Mg core of a star with a zero-age main sequence mass of $\sim 8 - 11$ $M_{\odot}$ undergoes electron capture just shy of reaching M_{ch}, reducing the electron degeneracy pressure supporting the star causing it to collapse (Nomoto, 1980; Nomoto et al., 1982; Nomoto et al., 1984; Nomoto, 1987).

1.3.1. Type II Supernovae

SNe II are the ultimate fate of most single, massive stars, and some massive stars in binary systems. Their spectra are characterized by prominent hydrogen Balmer lines. Historically, they have been further classified by the shape of their light curves into Type IIL and IIP. SNe IIL show light curves that decline linearly from peak, while SNe IIP have a "plateau" feature which occurs after maximum light, where the light curve declines slowly for ~ 100 days. Recent works examining large samples of SNe II have found that these classifications are largely historical, and that the two types are part of a larger continuum, where the light curve behavior is determined by the mass of the hydrogen envelope at the time of explosion (Anderson et al., 2014; Valenti et al., 2016). SNe II with low envelope masses will show light curves closer to the prototypical IIL, while SNe II with larger hydrogen masses are more likely to become SNe IIP.

More recently, further subclasses of SNe II have been suggested based on other spectroscopic properties. For objects which show narrow emission lines superimposed on the SNe II spectrum, they are classified as SNe IIn. These narrow lines originate in the circumstellar material ejected from the star in the years prior to explosion either from winds or other massive outbursts, which are shock heated through interaction with the supernova ejecta. Another variant of SNe II is the so-called SNe IIb, which exhibit a multi-peaked light curve where the early spectra show weak hydrogen lines, which fade away leaving behind a spectra that more closely resembles a SNe Ib as the supernova evolves. It is thought that these objects have small hydrogen envelope masses, where the mass may have been stripped by a binary companion as opposed to ejected from the star via winds or pre-supernova mass loss events.

1.3.2. Type Ib/c (Stripped Envelope) Supernovae

Type Ib/c are similar in nature to SNe II in that they are thought to arise from massive stars; however, at the time of explosion they have lost either their massive hydrogen (SNe Ib) or hydrogen and helium (SNe Ic) envelopes (Smith et al., 2011; Smith, 2014; Smartt, 2009b, 2015a; Stritzinger et al., 2018a) The exact mechanism by which these massive stars are stripped of their envelopes is unclear, but two leading theories are that they are stripped by strong stellar winds or by interaction in a close binary system (Smith, 2014; Pian & Mazzali, 2017; Bersten & Mazzali, 2017). Since SNe Ib still retain their helium envelope, helium lines feature prominently in their spectra; while having lost both their hydrogen and helium envelopes, SNe Ic are dominated instead by spectral

lines of other intermediate mass elements like oxygen, calcium, and sodium. However, given the difficulty of exciting helium at low temperatures, there have been suggestions that some SN Ic may still retain small He envelopes at the time of explosion.

1.4. Thesis Outline

This work takes a phenomenological approach to understanding the diversity of Type Ia supernova through the use of differential comparisons. Part I covers the theory portion of this work; which consists of the simulation of spectra with one-dimensional radiative transfer modeling with the `SYNOW` and `PHOENIX` codes, and how these synthetic spectra can help us connect observations to theoretical models of supernovae; enabling us to answer outstanding questions about their progenitor systems and explosion mechanisms. Chapter 3 presents the results of this work, focusing on the identification of spectral lines and formation of the spectra at ultraviolet wavelengths in SN 2011fe, which was first presented in DerKacy et al. (2020), and is shown here with minor edits for readability.

Part II presents the observational component of this work, including five years of observations collecting optical spectra of all types of supernovae with the ARC 3.5m telescope at Apache Point Observatory. Chapter 4 details the scientific questions under investigation by the two collaborations these observations were coordinated through, including questions related to the study of both thermonuclear and core collapse supernovae. Chapter 5 focuses on SN 2021fxy, a Type Ia supernovae observed by the POISE collaboration for which multiple epochs of ultraviolet spectroscopy from the *Hubble Space Telescope* were obtained. A version of this work will be submitted to MNRAS in the near future. Chapter 6 contextualizes the work of Chapters 3 and 5 within the broader literature on Type Ia supernovae, and presents a path forward for future studies to utilize differential comparisons to further investigate and understand the diversity of SNe Ia.

Part I

Theoretical Work

CHAPTER 2

Theoretical Foundations

2.1. UV Spectral Formation in Type Ia Supernovae

Ultraviolet (UV) spectra are a unique probe of SNe Ia physics and their evolution throughout the history of the universe. Much of the information about the properties of the progenitor star and the explosion mechanism are encoded in the outer layers of the SN Ia ejecta; a region that UV spectra probe at later times than the optical (Höflich, 2002). Despite the near uniformity of optical and NIR properties of normal SNe Ia, their ultraviolet properties are quite diverse. The best example of this diversity are the "twin" supernovae SN 2011fe and SN 2011by whose optical properties are nearly identical, but differ greatly in the UV (Foley & Kirshner, 2013). Additionally, multiple studies have found variations in the UV spectra of SNe Ia with redshift suggesting that the progenitor properties may change over time (Ellis et al., 2008; Foley et al., 2012; Maguire et al., 2012). UV spectra are an under-studied resource to answer many unresolved questions on the physics of SNe Ia.

The observed UV spectrum is determined primarily by the combination of three factors: (1) the progenitor metalicity, (2) the density structure, and (3) the bolometric luminosity of the SN. The amount of metals in the outer layers of the SN ejecta correlate with the strength of the line blanketing, resulting in progenitors with larger metalicities having lower flux values in the UV (Lentz et al., 2000; Foley & Kirshner, 2013). SNe Ia density profiles can be roughly approximated by power laws, with those SNe with steeper density gradients (e.g. smaller power law exponents) producing smaller flux values and less prominent spectral features (Sauer et al., 2008; Hachinger et al., 2013; Mazzali et al., 2014). Finally, luminosity studies indicate that increasing the overall luminosity of the SN results in greater flux in the UV, as well as changes in the location and strength of spectral features (Walker et al., 2012), although this interpretation is complicated by the changing of the underlying model.

2.2. Spectral Synthesis Codes

2.2.1. PHOENIX

PHOENIX is a generalized, multi-purpose stellar atmosphere and radiative transfer code. It is capable to calculating synthetic spectra from both 1-D and 3-D hydrodynamic models, in both local thermodynamic equilibrium (LTE) and full non-local thermodynamic equilibrium (NLTE). PHOENIX has successfully been used to simulate stellar spectra (Passegger et al., 2016, 2020), supernovae (Bongard et al., 2008; Baron et al., 2012, 2015), and exoplanet atmospheres (Peacock

et al., 2019; Lothringer et al., 2020).

The synthetic spectra in this work were calculated using `PHOENIX/1D` version `18`. In this mode, `PHOENIX` requires a 1-dimensional hydrodynamic model of a supernova explosion as input, including physical parameters such as density, temperature, velocity and elemental abundance profiles. The radiative transfer equation is then solved along characteristic rays in spherical symmetry including special relativistic effects.

Each model atom includes primary NLTE transitions, which are used to calculate the level populations and opacity, however, all the opacity is included even if the levels of those lines are not in the model atom. These weaker lines are treated in LTE using the true NLTE occupation of the ground state. This opacity implicitly affects the rate equations via their effect on the solution to the transport equation (Hauschildt & Baron, 1999) and ensures that no line transition is excluded. For ions not treated in NLTE the line opacities are treated with the equivalent two-level atom source function, using a thermalization parameter, $\alpha = 0.10$ (Baron et al., 1996). The effects of ionization due to non-thermal electrons produced from the γ-rays produced from the radioactive decay of ^{56}Ni synthesized during the supernova explosion are included. The ions treated in NLTE are He I-II, C I-IV, O I-III, Ne I, Na I-II, Mg I-III, Si I-IV, S I-III, Ca II, Ti II, Cr I-III, Mn I-III, Fe I-III, Co I-III, and Ni I-III. These should encompass all the ions that have features that significantly form the observed spectral features in SNe Ia.

The atmospheres are iterated to energy balance in the comoving frame; while we neglect the explicit effects of time dependence in the radiation transport equations, we do implicitly include these effects, via explicitly including PdV work and the rate of gamma-ray deposition in the generalized equation of radiative equilibrium and in the rate equations for the NLTE populations. The outer boundary condition is the total bolometric luminosity in the observer's frame, and is the main tunable parameter in the simulations. The inner boundary condition is that the flux at the innermost zone is given by the diffusion equation. Converged models require 256 optical depth points to correctly obtain the Si II λ6355 profile. The model is simulated at several different target luminosities, after which the spectra are examined and the best fit determined, again via"chi-by-eye".

The models calculated in the work were calculated using the resources of the OU Supercomputing Center for Education & Research (OSCER) at the University of Oklahoma (OU), the National Energy Research Supercomputer Center (NERSC), which is supported by the Office of Science of the U.S. Department of Energy under Contract No. DE-AC03-76SF00098 and at the Höchstleistungs Rechenzentrum Nord (HLRN). We thank all these institutions for generous allocations of computer time.

2.2.2. SYNOW

SYNOW is a highly parameterized spectral synthesis code designed to simulate supernova spectra during the photospheric phase. It relies on a set of simple assumptions including, (1) spherical symmetry, (2) homologous expansion ($v \propto r$), (3) a sharp photosphere which emits a black body continuum, and (4) that the lines formed within the atmosphere are the result of resonance scattering that is treated in the Sobolev approximation. SYNOW does not calculate ionization ratios, nor excitation ratios, and does not perform continuum transport.

The purpose of SYNOW is to assist observers in the identification of spectral lines in supernova spectra, and in estimating the approximate velocity range within the SN ejecta where an ion resides. As such, the code accepts a user defined input file, with several global and ion specific parameters. The global parameters include: the photospheric velocity (v_{phot}), the blackbody temperature (T_{bb}), the velocity extent of the SN ejecta (v_{max}), the minimum optical depth (τ_{min}), and the velocity resolution (Δv). Important parameters for the individual ions included in the fit are: the fastest and slowest velocities of the ion in the ejecta (v_{max}, v_{min}), the e-folding velocity of the ion (v_e), the excitation temperature of the ion (T_{exec}), and the photospheric optical depth of the reference line (τ), which is typically the strongest optical line for a given ion.

From this list of inputs, SYNOW calculates the supernova spectra, resulting a spectrum of blended P-Cygni features superimposed on the blackbody continuum. The optical depths of lines other than the reference line are calculated assuming LTE excitation. The line optical depths decrease radially according to $\tau(v) = \tau(v_0)e^{-(v-v_0)/v_e}$. The best fitting models are again determined by eye. Examples of the spectra produced by SYNOW can be found in Chapters 3, 4 and 5.

CHAPTER 3

Ultraviolet Spectral Formation Near Maximum Light in SN 2011fe

This chapter is a modified version of DerKacy et al. (2020), which was published in *The Astrophysical Journal*, with minor revisions, including the removal of the abstract, to improve readability.

3.1. Introduction

The ultraviolet (UV) spectrum of Type Ia supernovae (SNe Ia) is important for understanding the nature of the explosion, since it both forms throughout the supernova atmosphere (Bongard et al., 2008) and probes the outermost layers (Lentz et al., 2000; Hoeflich et al., 2017). Variations in the UV spectra with redshift have been observed (Ellis et al., 2008; Foley et al., 2012; Maguire et al., 2012). Foley & Kirshner (2013) used a comparison of the "twins" SNe 2011by and 2011fe to deduce a variation in progenitor metallicity between the two supernovae, using the models of Lentz et al. (2000) to infer that progenitors of SNe 2011by and 2011fe were supersolar and subsolar, respectively. Brown et al. (2015) found that they could reproduce the same results as those of Foley & Kirshner (2013) using only photometry obtained by the Neil Gehrels Swift Observatory, hereafter *Swift*. However, they found that the UV flux levels of the Lentz et al. (2000) models were far too high, due to the structure of W7 model (Nomoto et al., 1984). Recently, Pan et al. (2020) used grism spectroscopy of a sample of SNe Ia obtained with *Swift* and correlated it with the progenitor metallicity. Using *Swift* photometry, this result has been challenged (Brown & Crumpler, 2020).

Several studies have identified UV features in SNe Ia using a variety of models and methods, but few line identifications are consistent across these works (Table 3.1 lists the identified features from the literature). Branch & Venkatakrishna (1986) used an early version of the parameterized `SYNOW` code to identify features in the near-UV of an IUE spectrum of SN 1981B at -2 days relative to maximum light. Kirshner et al. (1993) analyzed the first high-quality near-maximum light spectrum of a Type Ia; a combined IUE and HST spectrum of SN 1992A at +5 days. Using a parameterized synthetic LTE spectrum of a delayed-detonation explosion model, they were able to identify many of the mid-UV features, although some identifications are described as tentative. Hachinger et al. (2013) studied the HST spectrum of SN 2010jn at -0.3 days. Using an updated version of the Monte Carlo spectrum-synthesis code of Mazzali & Lucy (1993), they calculated synthetic spectra using the density profiles of the W7 model (Nomoto et al., 1984) and the WDD3 delayed-detonation model from Iwamoto et al. (1999) with abundances determined via abundance

tomography. Mazzali et al. (2014) (hereafter M14) performed a similar analysis to Hachinger using the WDD1 delayed-detonation model of Iwamoto et al. (1999) on a time series of HST spectra of SN 2011fe covering from -13.1 to +40.8 days, including the first spectrum to have significant coverage of the far-UV (+3.4 days).

Other factors influencing the UV spectra of SNe Ia, such as density and model luminosity, have also been investigated. Using much of the same methodology as Hachinger et al. (2013) and M14, Sauer et al. (2008) altered the power law index of the density profile in the outer layers of the W7 model, concluding that steeper density profiles result in more UV flux and a better match to observed UV spectra than those with shallower density profiles; all without producing large changes in the optical spectra. Walker et al. (2012) varied the luminosity of their models, finding that high luminosity models produce more UV flux, but more featureless UV spectra. The interpretation of these results is made more complex since they simultaneously changed the density structure of their models when varying the luminosity.

We present synthetic spectra from SYNOW and PHOENIX which are used to identify all major features from the far-UV to the near-UV in the +3.4 day HST spectrum of SN 2011fe first presented in Mazzali et al. (2014). A suite of PHOENIX spectra are then used to further examine the impact of different mechanisms that combine to form the UV spectrum, and to determine the temperature dependence of multiple features, which may be useful in constraining physical parameters within the ejecta. Section 3.2 outlines the models and spectral synthesis codes used in this work, with the line identifications from these spectra presented in Section 3.3. Section 3.4 further examines line formation mechanisms that play an important role in the UV. Section 3.5 places these results into the broader context of work on UV spectra of Type Ia SNe. Section 3.6 summarizes our conclusions.

3.2. Spectral Modeling

This work makes use of two different spectral synthesis codes, SYNOW and PHOENIX, capable of making line identifications in supernova spectra. Both codes rely on different assumptions and underlying physics to synthesize the spectra, providing a useful check on the other and improving our confidence in each line identification. The two codes are briefly summarized below.

3.2.1. SYNOW

SYNOW is designed to simulate supernova spectra and relies on simple assumptions that describe the supernova during the photospheric phase, including: spherical symmetry, homologous expansion ($v \propto r$), a sharp photosphere that emits a blackbody continuum, and lines formed via resonance scattering, which are treated in the Sobolev approximation. SYNOW does not perform continuum transport; nor does it calculate ionization ratios or solve rate equations. Its primary purpose is to account for multiple line scattering so that it can be used in the empirical spirit to make line

identifications, estimate the photospheric (or pseudo-photospheric) velocity, and roughly determine the velocity interval within which each ion is detected. The synthetic supernova spectrum generated by SYNOW consists of blended P-Cygni profiles (consisting of an unshifted emission component with a blueshifted absorption component) superimposed on the blackbody continuum.

For each ion included in the fit, the optical depth of a reference line at one velocity (typically the photospheric velocity) is a fit parameter, and the optical depths of the other lines of the ion at that velocity are calculated assuming a Boltzmann excitation temperature T_{exc}. Typically, the strongest optical line of an ion is chosen as the reference line. To limit the parameter space of the fit, T_{exc} is chosen to have the same value for each ion, 8000 K for the fit shown here. All line optical depths decrease exponentially with velocity, according to $\tau(v) = \tau(v_0)e^{-(v-v_0)/v_e}$, where the e-folding velocity v_e is generally taken to be 1000 km s^{-1}. Therefore, the important parameters of the fit are the photospheric velocity v_0, the optical depths of the ion reference lines, the velocity extent of each ion, and the e-folding velocity v_e of each ion. The fit is optimized by eye, as is standard within the community. More information on SYNOW can be found in Jeffery & Branch (1990) and Branch et al. (2005, 2006).

3.2.2. PHOENIX

This work makes use of a generalized 1-D delayed detonation (DD) model first presented in Domínguez et al. (2001) which reproduces the light curves and spectra of Branch-normal supernovae and was previously shown to well match the pre-maximum light spectra of SN 2011fe in Baron et al. (2015) (specifically, we use the prompt DDT model whose density structure is shown in their Figure 1). The model starts with a C/O white dwarf taken from the core of an evolved 5M$_\odot$ main-sequence star. This core approaches the Chandrasekhar mass through accretion, and an explosion is spontaneously triggered when the central density reaches 2.0×10^9 g cm^{-3}. The deflagration-to-detonation transition occurs at a density of 2.3×10^7 g cm^{-3}. The metallicity of the model is $Z_\odot/20$ where the metallicity is defined as the ratio of the iron abundance to the solar iron abundance. The abundance structure of the model is shown in Figure 3.1. Here, we recalculate the spectra using PHOENIX at 23 days after explosion, corresponding to the +3.4 day HST spectrum of SN 2011fe first presented in M14.

PHOENIX/1D version 18 is a general purpose stellar atmospheres program. It solves the radiative transfer equation along characteristic rays in spherical symmetry including all special relativistic effects. PHOENIX/1D solves the non-LTE (NLTE) rate equations. The effects of ionization due to non-thermal electrons produced from the γ-rays produced from the radioactive decay of ^{56}Ni synthesized during the supernova explosion are included. The ions treated in NLTE are He I-II, C I-IV, O I-III, Ne I, Na I-II, Mg I-III, Si I-IV, S I-III, Ca II, Ti II, Cr I-III, Mn I-III, Fe I-III, Co I-III, and Ni I-III. These should encompass all the ions that have features that significantly form

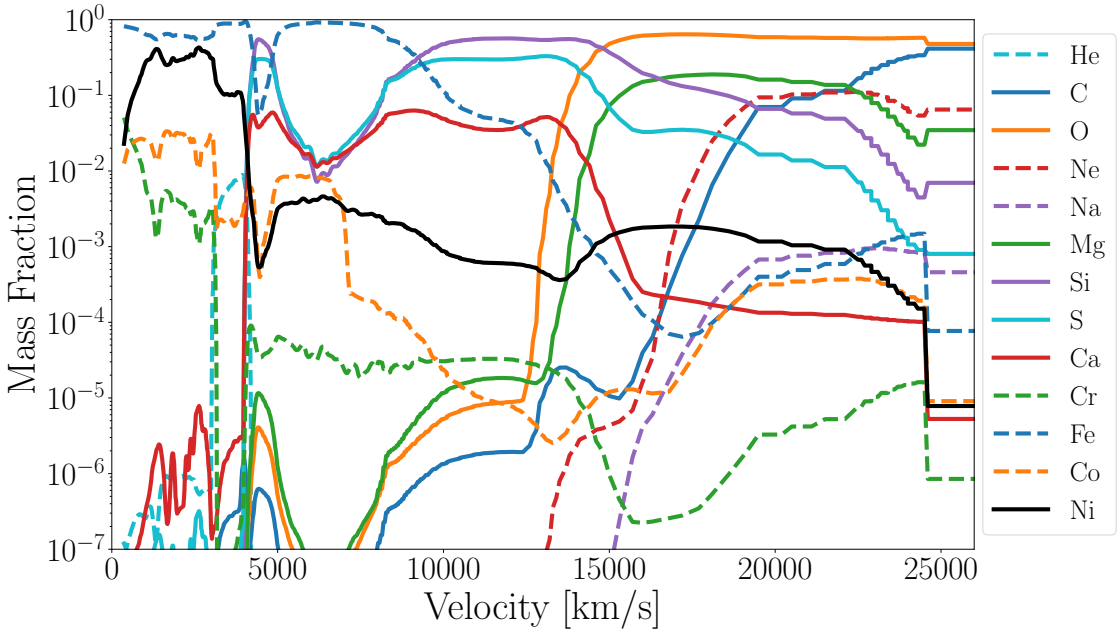

Figure 3.1: Final distribution of elements in the DD model as a function of velocity. All abundances are held constant above 25,000 km s^{-1}.

the observed spectral features in SNe Ia.

Each model atom includes primary NLTE transitions, which are used to calculate the level populations and opacity, however, all the opacity is included even if the levels of those lines are not in the model atom. These weaker lines are treated in LTE using the true NLTE occupation of the ground state. This opacity implicitly affects the rate equations via their effect on the solution to the transport equation (Hauschildt & Baron, 1999) and ensures that no line transition is excluded. For ions not treated in NLTE the line opacities are treated with the equivalent two-level atom source function, using a thermalization parameter, $\alpha = 0.10$ (Baron et al., 1996). The atmospheres are iterated to energy balance in the comoving frame; while we neglect the explicit effects of time dependence in the radiation transport equations, we do implicitly include these effects, via explicitly including PdV work and the rate of gamma-ray deposition in the generalized equation of radiative equilibrium and in the rate equations for the NLTE populations.

The outer boundary condition is the total bolometric luminosity in the observer's frame, and is the main tunable parameter in the simulations. The inner boundary condition is that the flux at the innermost zone (here $v = 700$ km s^{-1}) is given by the diffusion equation. Converged models require 256 optical depth points to correctly obtain the Si II λ6355 profile. The model is simulated at several different target luminosities, after which the spectra are examined and the best fit determined, again via"chi-by-eye".

Baron et al. (2015) use `PHOENIX/1D` version `16`, however the changes from version `16` to

Table 3.1. Previous UV Line Identifications

λ (Å)	1981B (-2 d)[a]	1992A (+5/6 d)[b]	2010jn (+4.8 d)[c]	2011fe (+0.1/+3.4 d)[d]
3300	Co II	-	Co II, Co III, Fe III	Co III, Fe III
3090	Fe II	-	-	Si III, Co III, Fe III
3010	-	Fe II, Co II, Si III	-	Si III, Co III, Fe III
2820	-	*Mg II*, Fe II	Fe II, Mg II, Fe III	Co III, Fe III
2650	-	Mg II, Fe II	-	Mg II, Fe II
2470	-	Fe II	-	Fe II, Co II
2250	-	Fe II	-	Fe II, Co II, Ni II
1950	-	*Cr II*	-	-
1580	-	-	-	-
1430	-	-	-	Si II, Co II, Fe III
1290	-	-	-	-

Note. — Line identifications that are described as tentative/weak by the original authors are italicized.

References. — Branch & Venkatakrishna (1986); [b]Kirshner et al. (1993); [c]Hachinger et al. (2013); [d]Mazzali et al. (2014)

version `18` are confined to the `PHOENIX`/3D mode, updates to the molecular line lists (not included in either the previous or current calculations) and various bug fixes.

3.3. Line Identifications

Guided by the previous line identifications in near maximum-light spectra of Type Ia SNe outlined in Table 3.1, we generate synthetic spectra to fit the +3.4 day HST observations of SN 2011fe. Our goal is to provide a complete set of line identifications for the spectral features in the near max-light UV spectra of Type Ia SNe, and in particular to address the disagreement over whether singly or doubly ionized iron group elements (IGEs) like Fe and Co are responsible for UV feature formation.

3.3.1. SYNOW Line ID's

Figure 3.2 shows the `SYNOW` spectrum and corresponding line identifications. Overall the `SYNOW` spectrum fits the observations well, although the lines are too strong in some mid-UV features. Compared to previous line identifications in near-max light UV spectra of Type Ia SNe (see Table 3.1), the identifications of UV features differ significantly in the both the near and far-UV.

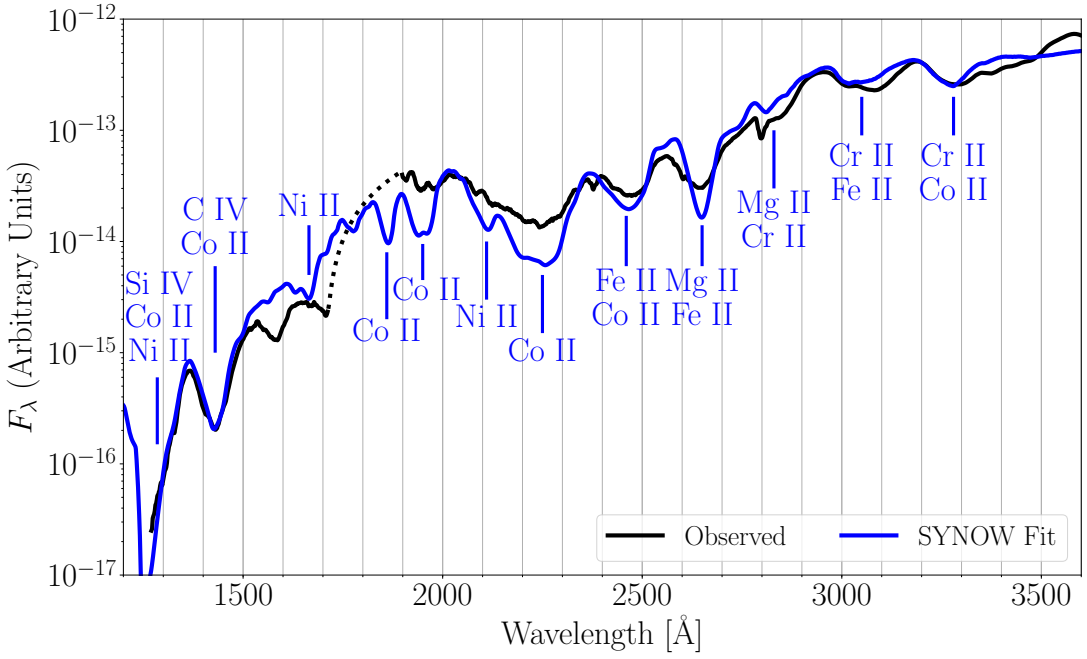

Figure 3.2: SYNOW Fit with line identifications (in blue) as compared to HST observations (black). The gap in the spectrum from $\sim 1700 - 1900$ Å (dotted black line) is due to a gap in the wavelength coverage of HST. As such, any line identifications within or bordering this region should be considered tentative.

For the first time, Cr II is identified in the near max-light UV spectrum of a Type Ia, and the features centered around ~ 3300 Å $\sim 3090/3010$ Å and ~ 2820 Å features.[1] Additionally, the contributions from Fe and Co throughout the UV are attributed solely to the singly ionized states, not partially or wholly to the double ionized states as found previously. In the mid-UV, we find better agreement with previous work, where the prominent features are identified as blends primarily of Fe II, Co II, and Ni II, with the ~ 2820 Å and ~ 2650 Å features requiring contributions from Mg II lines. In the far-UV, the main features are caused by the strong resonance lines of C IV and Si IV blended with weaker Co II and Ni II lines as the primary iron group element contributors.

3.3.2. `PHOENIX` Line ID's

Previously, line identifications made with `PHOENIX` were determined via "single-ion spectra", where the converged model has all line opacities artificially set to zero, except for the ion of interest (Bongard et al., 2008). However, in the UV line blanketing from IGEs and blending of strong lines of intermediate mass elements (IMEs), unburned material, and IGEs in the UV contribute to the formation of the broad UV spectral features making the use of single-ion spectra difficult.

[1] M14 identify Cr II in both the near-UV features at early times, but argue that these features change to blends of Fe III and Co III around -7 days

Instead, we adopt the inverse approach, setting the line opacities in our ion of interest to zero and looking for changes in the flux near the spectral features by subtracting the spectra without the ion of interest from the full fit. While spectra are not additive in this manner, this approach provides us with the minimal contribution of the strong lines for each ion of interest to the spectrum. Another relatively minor complication is that PHOENIX iterates the scattering problem when generating spectra so the mean intensity J, is readjusted for the new (diagnostic) opacity and source function. Since the opacity changes less in the inverse single-ion approach than in the single-ion approach, the inverse approach should be preferable for this particular effect. The relative line strengths of "inverse single-ion spectra" for the ion of interest will be underestimated in blended features due to photons scattering into the other lines comprising the blend. Locally normalized spectra (Jeffery et al., 2007) are used in the line identification process to account for the flux change of over four orders of magnitude from the near to far-UV. We only identify lines with a residual greater than 0.1 in order to avoid identifying weak lines that contribute to the line blanketing in the region but not the feature itself. While this choice of residual value is somewhat arbitrary, residuals less than 0.1 are hard to distinguish when visually comparing spectra with and without the ion of interest, and typically do not change the line shapes when excluded from the best fit spectrum (see the weak Cr II lines within Figure 3.5 for example).

Figure 3.3 shows the line identifications in the UV according the PHOENIX inverse single-ion spectra plotted in Figure 3.4 and Figure 3.5. Overall, the model replicates the observed spectrum well in the near and far-UV, but overestimates the flux levels in the mid-UV.

Near-UV features are blends of IGEs including Fe II and Co II with the exception of the $\sim$ 2820 Å feature which includes a contribution from Mg II ($\lambda\lambda 2929, 2937$). In the mid-UV, features are similarly due to Fe II and Co II, again with a contribution from Mg II ($\lambda\lambda 2796, 2803$) to the $\sim$ 2650 Å feature. There is also an isolated Ni II feature at $\sim$ 2080 Å. The $\sim$ 2470 Å and $\sim$ 2650 Å features have the correct shape but are blueshifted relative to the observations. M14 also had difficulties in fitting sections of the UV spectrum with their WDD1 model, with the mid-UV fit showing a similar blueshift in the feature minima, albeit with flux values that were too low. This suggests that these blueshifts in the mid-UV feature minima are inherent in all delayed-detonation models, possibly due to the shape of the density profiles in the regions where these features form. The likely cause of the mid-UV flux differences are differing metallicities in the models ($0.5Z_{\odot}$ in M14 compared to $0.05Z_{\odot}$ here). This would support the conclusions of Foley & Kirshner (2013) that 2011fe and 2011by differ in flux in the mid-UV due to differing metallicities. However, full exploration of the impacts of varying the metallicity in delayed-detonation models is beyond the scope of this work.

In the far-UV, blends are much more complicated, with lines from Fe II and Ni II blending with a complex of Mg II lines with rest wavelengths of $\sim$ 1480 Å and Si II($\lambda\lambda 1527, 1533$) near the

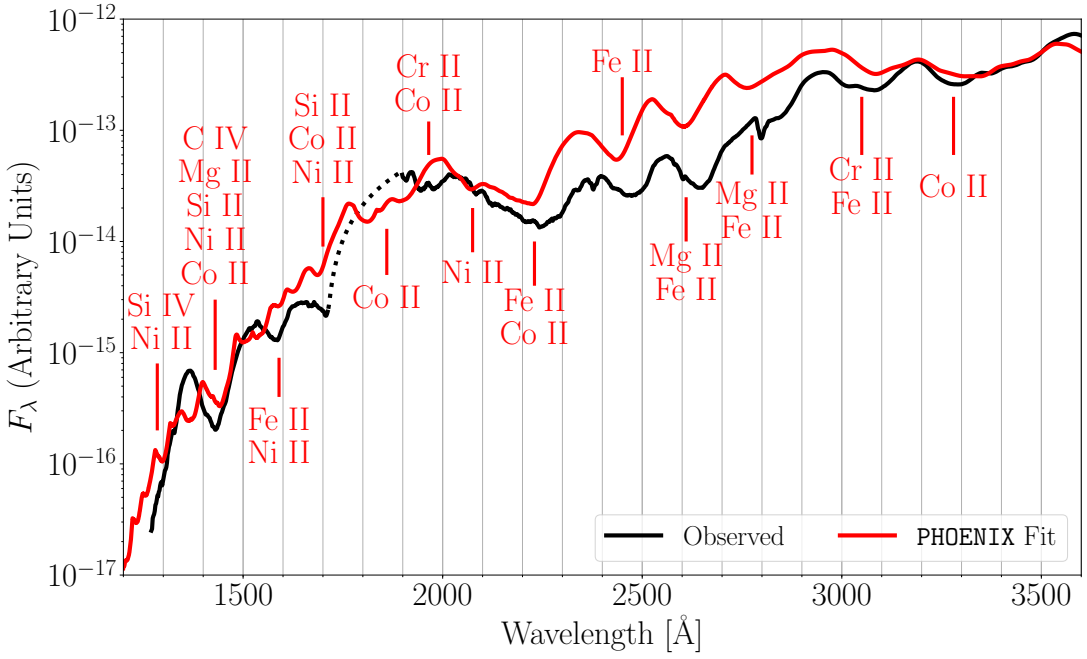

Figure 3.3: Same as Figure 3.2, but with the PHOENIX best fit and line identifications (in red). Features in the far-UV are noticeably more complex than those in the SYNOW fit, and include more ions making significant contributions to the line blending.

resonance lines from highly ionized species like C IV ($\lambda\lambda 1548, 1551$) and Si IV ($\lambda\lambda 1394, 1403$). Determining the location of the C IV and Si IV resonance lines from the minimum of the residual yields velocities of $22,700$ km s^{-1} and $19,300$ km s^{-1}. Similarly, the Si II and Mg II UV features are also formed in the outer layers of the ejecta with velocities of $21,600$ km s^{-1} and $18,000$ km s^{-1}, $18,600$ km s^{-1}, and $20,200$ km s^{-1} for the $\sim$ 1480 Å, $\lambda\lambda 2796, 2803$, and $\lambda\lambda 2929, 2937$ lines respectively. This indicates that the UV resonance lines can be an important probe of the nature of the outermost part of SNe Ia ejecta. Particularly the C IV line can give information on both the carbon abundance and the highest velocity of the ejecta, providing clues to the SNe Ia environment.

To our knowledge C IV and Si IV have never before been identified in a SN. While lines of singly and triply ionized C and Si are seen, very little, if any doubly ionized lines are identified in the UV. Unlike the doubly ionized states, where the paired valence electrons increase the excitation energies and force the resonance lines into the unobservable UV, the triply ionized states have only one easily excited valence electron, which allows the resonance lines to be located in the far-UV. All other lines of the triply ionized state are high excitations and therefore unobserved.

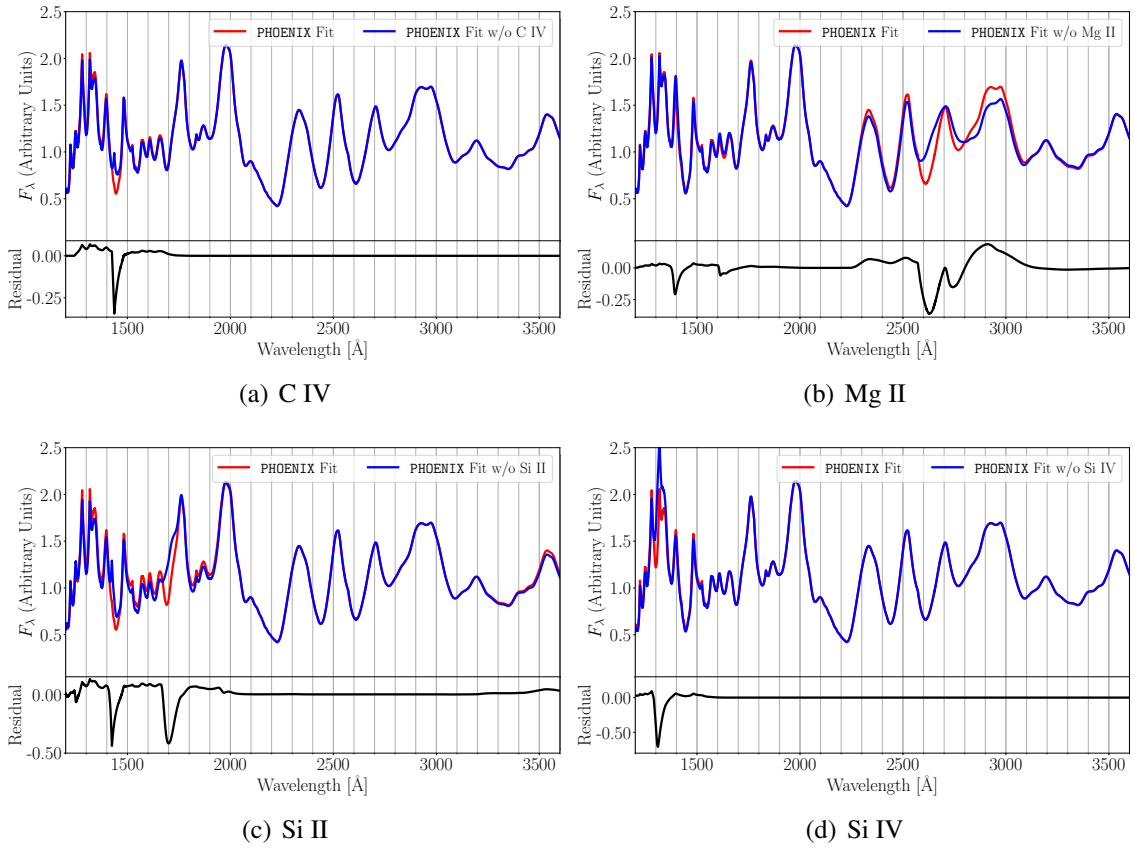

(a) C IV (b) Mg II

(c) Si II (d) Si IV

Figure 3.4: Residual plots of unburned material and intermediate mass elements that contribute to feature formation in the UV. The top panel of each plot shows the locally normalized UV spectra of the full PHOENIX fit (in red) over plotted with the PHOENIX fit without the ion of interest (blue).

3.3.3. Agreement between SYNOW and PHOENIX Line ID's

In general, the line identifications from the SYNOW and PHOENIX fits agree with each other, with a few exceptions. In the near-UV, both fits agree that the observed features are due to blends mainly consisting of Fe II and Co II. However, the PHOENIX model disagrees that Cr II is a significant contributor to the $\sim$ 2790 Å and $\sim$ 3300 Å features. While a Cr II line is present at the $\sim$ 3300 Å in the residual in Figure 3.5, the line at this location is too weak to be considered a detection. This is perhaps due to the relatively small amount of Cr present in the model, but may also be due to line blanketing or NLTE effects included in PHOENIX but not SYNOW. Both synthetic spectra find that the mid-UV can be modeled by blends of Mg II, Cr II, Fe II, and Co II, although there is some disagreement over the specific compositions of individual blends (ex. Fe II and Co II in the $\sim$ 2470 Å and $\sim$ 2250 Å features). Both fits also find support for an isolated Ni II feature at $\sim$ 2080 Å. In the far-UV, both fits agree on the necessity of C IV and Si IV to fit the observed features, however they disagree slightly on the weaker components of the blends, with the PHOENIX fit showing evidence of Si II, Mg II and Ni II in the $\sim$ 1430 Å blend, while not finding

significant Co II in the $\sim$ 1290 Å feature. Throughout the UV, both the SYNOW and PHOENIX fits find doubly ionized iron group species make no significant contributions to any features.

3.3.4. Model Agreement in Optical and NIR

An important test for the validity of delayed-detonation models is the ability to simultaneously reproduce observed spectra across a large wavelength range. Figure 3.6 shows the best fit model is able to match the observed spectrum not only in the UV, but the optical and NIR as well. While the model is able to reproduce the spectrum in the UV and optical, there is a consistent flux excess in the NIR, extending to 2.5 microns. Using the same model, Baron et al. (2015) were able to replicate the optical and NIR spectra (see their Fig. 11) at max light but did not attempt to simultaneously fit the UV, which suggests the underlying model is limited in its ability to recreate the spectra in all three regions at once. This particular model seems to produce the Ca H+K line significantly stronger than observed, which is likely due to the structure of the explosion model itself. Potential causes of these flux mismatches are further explored in Subsection 3.4.3.

3.4. Other Spectral Formation Mechanisms

3.4.1. Photoionization Edges

At the threshold wavelength for a bound-free transition, the opacity jumps, since redward of that wavelength the opacity in that transition is zero, and as one reaches the threshold energy, the opacity is finite. This jump in opacity is not dissimilar to what happens in a line, and thus at the threshold wavelength of bound-free (photoionization edges), one sees P-Cygni like features, with only continuum opacity and all line transitions ignored (Baron et al., 1999). These photoionization edges are easily seen in "continuum-only spectra", which are generated in a manner similar to "single-ion spectra" but with the opacities of all lines artificially set to zero, leaving only the bound-free and free-free processes to determine the opacity. The continuum-only spectra of Bongard et al. (2008) show in the W7 model near maximum light several photoionization edges form blue-wards of 2000 Å (see their Figure 5).

Examining the ionization energies of elements present in the model reveals two potential sources of the edges. The first is ionization of C and O from low excitation states in the outer layers of the ejecta. The second is ionization from higher excitation states of Fe II located deep within the ejecta. We create continuum-only spectra of our DD model, shown in Figure 3.7 with panel (a) showing the wavelengths of ionization edges from C I, C III, and O II; while panel (b) shows the ionization locations of Fe II. All photoionization edges in our model form in the far-UV, and some are coincident with the features that form at $\sim$ 1430 Å and $\sim$ 1290 Å. In both cases, not all excited states correspond to an observed edge in the model, and several edges seen in the model may in fact be combinations of edges from different ions (ex. the edge at $\sim$ 1450 Å is located near ionizations

of C I, O II, and Fe II).

3.4.2. Line Blanketing

Line blanketing from IGE's has long been thought a dominant factor in determining the flux levels in the UV spectra of Type Ia SNe. Utilizing PHOENIX's ability to artificially remove elements from the spectra by setting the opacities of specific elements to zero, we create an IGE-only spectrum, containing only the lines of Cr I-III, Mn I-III, Fe I-III, Co I-III, and Ni I-III to determine the importance of this effect. The IGE-only spectrum is shown in Figure 3.8 compared to the best fit spectrum. In the near and mid-UV, the IGE only-spectrum is able to reproduce almost exactly the observed features and flux levels, excluding the contribution of Mg II in the mid-UV and the emission peak around 3200 Å. The tight agreement of the IGE-only spectrum with that of the full fit suggests that the IGE's are the primary drivers of spectral formation in this region, and measurements of this region can provide insight into quantities related to the velocity extent of iron group elements as well as their abundances.

However, in the far-UV the flux of the IGE-only fit slowly deviates from that of the full fit until it is an order of magnitude too high, indicating that lines from unburned and partially burned material in the outermost layers of the ejecta play an important role in the formation of this region of the spectrum. Further insights into this material may be gained from additional observations of Type Ia spectra in the far-UV.

3.4.3. Temperature Dependencies

Several spectral features, both in the optical and ultraviolet demonstrate strong temperature dependence in our models. We briefly describe a few of these ultraviolet features here, while a more complete analysis of all temperature dependent features in our models from ultraviolet to near-infrared is left to future work (J. DerKacy, et al., in prep). We should note that we use temperature in a very general sense to denote variations in the spectral energy distribution and ionization state throughout the atmosphere. Our models, are highly NLTE and thus one cannot capture either the state of the radiation field or the ionization state of the ions with one simple quantity, temperature.

To better understand this temperature dependence we created several runs of our underlying DD model, each with a different target luminosity. The underlying density and abundance structure was held constant in each run. Changing the target luminosity between runs alters the temperature structure, opacities, and ionization balance of the runs, while they are iterated to radiative equilibrium. The most temperature sensitive regions of the spectra are the far-UV, where variations are seen in both the overall flux level and the C IV blend near 1430 Å, and the mid-UV Fe II blends near ~ 2470 Å and ~ 2750 Å, and the full UV spectrum are shown in Figure 3.9.

The most noticeable difference in the spectra appears in the far-UV where the flux level of the spectra varies by three orders of magnitude across the runs. This drastic change in flux is caused by the changing ratio of Fe III/Fe II above the photosphere, as seen in Figure 3.11. Because Fe II is more efficient at redistributing flux from blue to red than Fe III, runs with lower temperatures that have a higher fraction of Fe II in the outer layers have lower UV flux levels and increased NIR fluxes. The variations in the NIR spectra can be seen in Figure 3.10. As the temperature in the outer layers is increased, the the UV (and especially far-UV) flux begins to deviate more from the observed spectrum while the NIR flux levels slowly come into agreement with observations.

3.5. Discussion

The ability of the model to match either the UV or NIR spectra, but not both, in addition to the optical spectra suggests several potential changes that may help to bring the model into better agreement with the observations. One potential change is to adjust the model's metallicity. This adjustment may prove difficult however, as any potential decrease in UV flux due to increased metallicity must be balanced against any increases in flux that result from higher opacities pushing the photosphere farther out in the ejecta and higher temperatures in the outer layers altering the ionization balance of the outer layers; in particular the Fe III/Fe II ratio. This is the subject of future work, where we will self-consistently study the metallicity dependence and compare to a broad range of observed SNe Ia.

Secondly, an incorrect distribution of ^{56}Ni could also play a role in the flux mismatch. Broad wavelength coverage can provide clues as to the velocity extent of ^{56}Ni (Ashall et al., 2019a,b). From the SN 2011fe light curve Piro (2012) concluded that ^{56}Ni was required in the outer $0.1 < M < 1 \times 10^{-3}$ of the supernova, however, Baron et al. (2015) found that ^{56}Ni at such high velocities did not affect the spectra, but they were focused on the optical and infrared and not the UV.

Finally, the density structure of the model, which beyond 18,000 km s^{-1} closely approximates an $n = 7$ power-law, may not accurately describe the density profile in the outer layers. Sauer et al. (2008) were able to produce similar results in their simulations of W7 by varying the power law exponent above 15000 km s^{-1}. Models with steeper density gradients produced lower flux values in the far-UV as they had a lower Fe III/Fe II ratio. However, the increased density in the outer layers result in smoother, almost featureless spectra. Models with shallower density gradients produced higher flux values due to high Fe III/Fe II ratios and appropriate spectral features. Taken together with our results, this suggests that temperature and density variations in the outer ejecta layers are degenerate with respect to the far-UV spectra. However, we stress that the full investigations of these effects needed to break this degeneracy are beyond the scope of this work.

The variation in the Fe III/Fe II ratio also partially explains the velocity shift in the Fe II blends in the mid-UV. As the amount of Fe II at higher velocities decreases with the increased temperature,

the Fe II lines form deeper in the ejecta at lower velocities, bringing the model into better agreement with the observed velocities of the feature. This change in the wavelength of the Fe II feature forming the blend at ~ 2650 Å could also be the result of the higher temperature favoring a different combination of Fe II lines in the region. Additionally, the higher temperatures drive an increase in the strength and width of the emission peak of the Mg II feature at ~ 2650 Å due to $\lambda\lambda 2796, 2803$. This in turn causes the absorption minima of the ~ 2820 Å feature to appear redder, in better agreement with the observations. Figure 3.12 shows the evolution of the Fe II and Mg II residuals with increasing temperature.

3.6. Conclusions

We fit the UV spectrum SN 2011fe at +3.4 days after maximum light with synthetic spectra generated by both SYNOW and PHOENIX (with a DD model) to provide line identifications for all major features. Both codes generally agree in their identifications, with both the near and mid-UV spectra comprised of blends of Cr II, Fe II, Co II and Ni II. Features in the far-UV are formed by strong resonance lines of C IV, Si II, and Si IV combined with the now less dominant lines from singly ionized IGE's that dominate the rest of the UV spectra. Leveraging the ability of PHOENIX to generate "single-ion spectra", we further investigate the impact of other spectral formation mechanisms on the UV spectra. We find several photoionization edges coincident with the far-UV features which significantly contribute to determining the flux level in this region. We also examine an IGE-only spectrum, which is able to reproduce both the features and flux levels of a significant portion of the UV spectrum, further confirming the utility of mid-UV measurements as a probe of IGEs in Type Ia SNe. Finally, using a suite of PHOENIX models with different target luminosities, we identify several regions of the UV spectrum with strong temperature dependence. In the far-UV, the Fe III/Fe II ratio in the outermost portion of the ejecta changes rapidly with temperature and results in a flux levels that vary by almost four orders of magnitude across the models. In the mid-UV, the features centered at 2250 Å and 2470 Å, which are too fast in DD models, begin to recede in velocity and better match observations.

DD models both here and elsewhere have shown the ability to replicate the spectra of Type Ia SNe in the UV and future work using DD models which implicitly account for metallicity and density variations are needed to investigate the UV diversity of Type Ia SNe in greater detail.

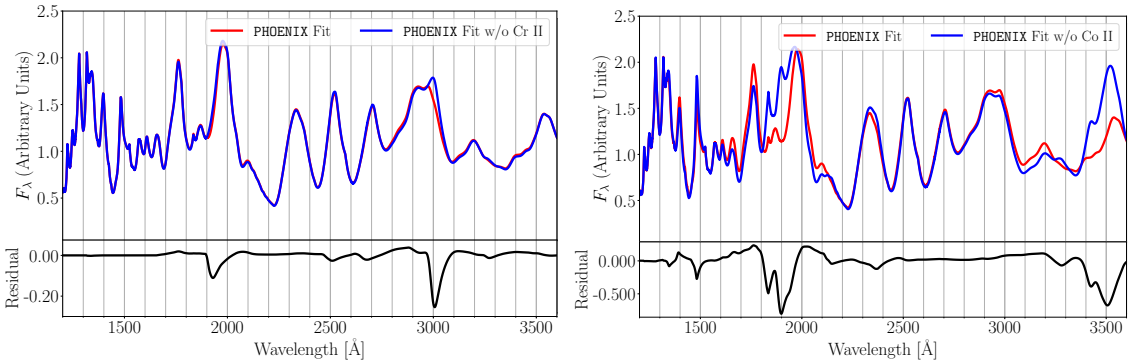

(a) Cr II

(b) Co II

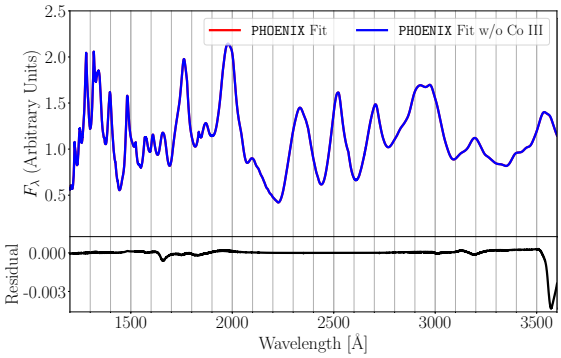

(c) Co III

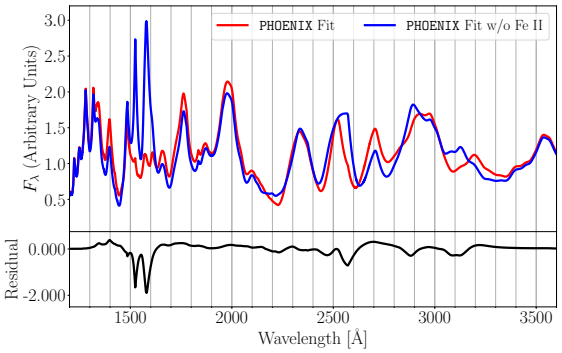

(d) Fe II

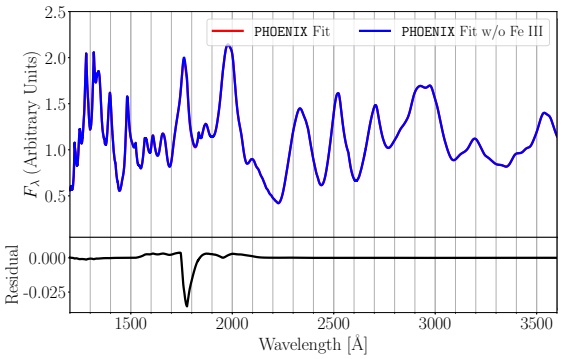

(e) Ni II

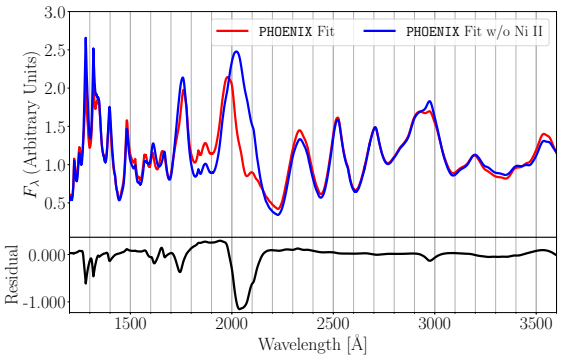

(f) Ni III

Figure 3.5: Same as Figure 3.4 but for the iron group elements.

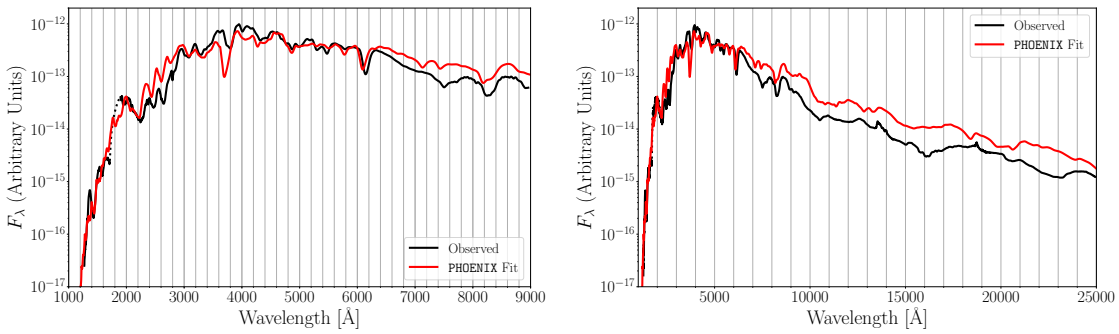

(a) (b)

Figure 3.6: The best fit PHOENIX spectrum at day 23 (in red) compared to observations (black) spanning from the far-UV to near-IR. The target luminosity of the model is 2.76×10^{42} erg s^{-1}. By including the UV in addition to the optical in the determination of the best fit spectrum, the optical fit is marginally worse than models where only the optical spectrum is considered in determining the best fit. Differences can primarily be seen in the flux levels near the Ca II H & K and NIR-triplet features.

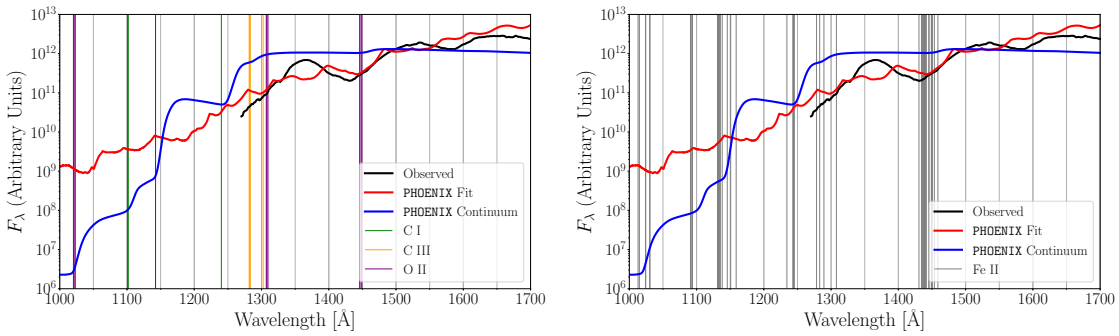

(a) (b)

Figure 3.7: Full PHOENIX fit (red), compared to observations (black) and the continuum-only fit (blue) scaled to the observed flux at 1500 Å. Photoionization edges due to C I (green), C III (orange), and O II (purple) are noted with vertical lines in panel (a). Panel (b) shows the same plot, with only Fe II photoionization edge locations in grey. The plots have been extended to show additional photoionization edges imprinted on the continuum fit beyond the wavelength range of the observed spectrum. The photoionization edges which are not easily visible in the full fit, are coincident with and contribute to the feature formation in the far-UV.

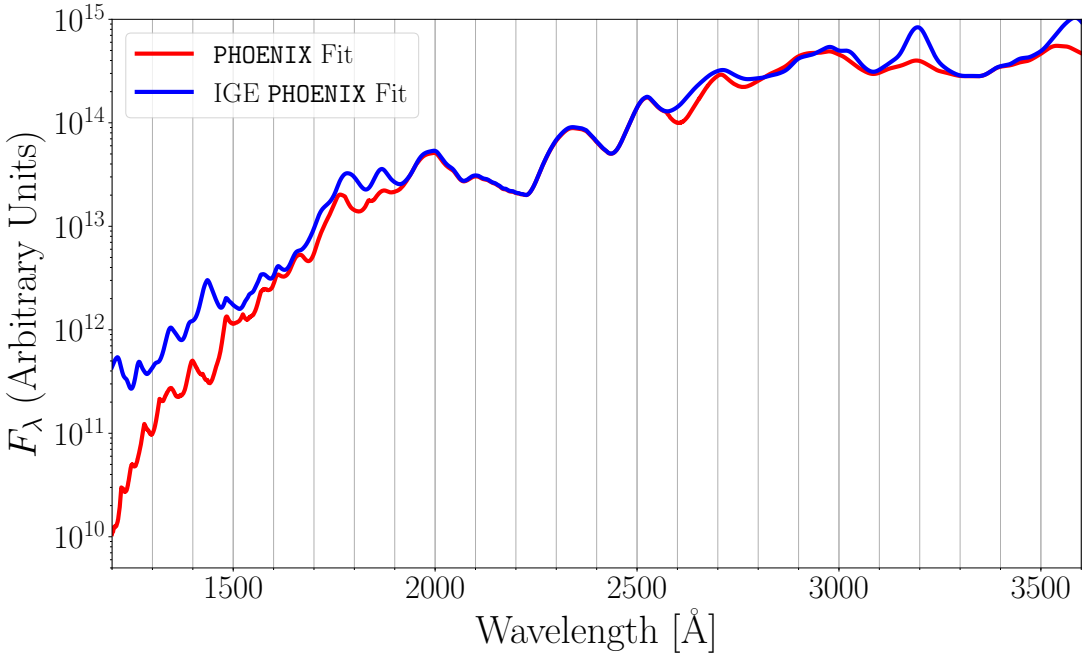

Figure 3.8: The full fit PHOENIX spectrum (red), compared to the best fit model with only IGE (Cr I-III, Mn I-III, Fe I-III, Co I-III, Ni I-III) lines included (blue).

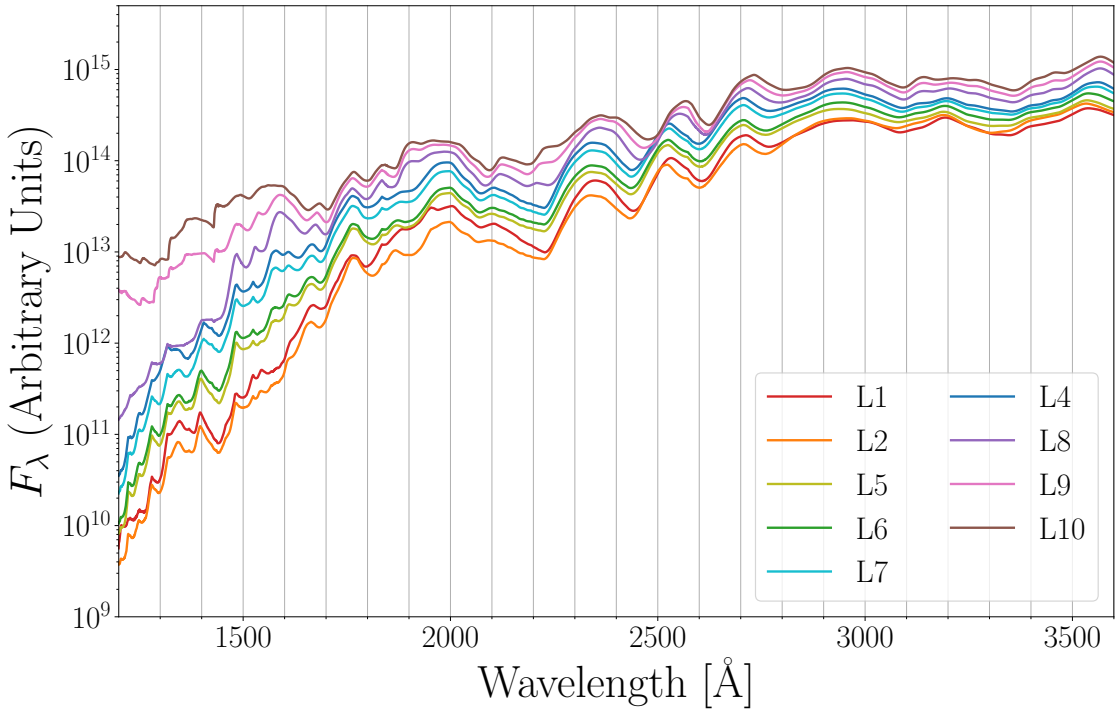

Figure 3.9: The suite of PHOENIX models with different target luminosities showing the evolution of the UV spectrum with temperature. The L6 model is the best fit model. The target luminosities of the models (in erg s^{-1}) are - L1: 7.50×10^{42}, L2: 7.90×10^{42}, L5: 8.29×10^{42}, L6: 8.69×10^{42}, L7: 9.08×10^{42}, L4: 9.47×10^{42}, L8: 1.03×10^{43}, L9: 1.11×10^{43}, and L10: 1.18×10^{43}. The temperatures at the electron scattering optical depth $\tau_{\rm std} = 2/3$ are L1: 12.1×10^3 K, L2: 12.2×10^3 K, L5: 12.0×10^3 K, L6: 12.3×10^3 K, L7: 12.2×10^3 K, L4: 12.2×10^3 K, L8: 12.1×10^3 K, L9: 12.3×10^3 K, L10: 12.4×10^3 K. Due to variations in the ionization state which causes variations in the position of $\tau_{\rm std} = 2/3$ and the NLTE nature of the ionization states, the temperatures are not perfectly monotonic, showing the extent of the deviation of the models from LTE.

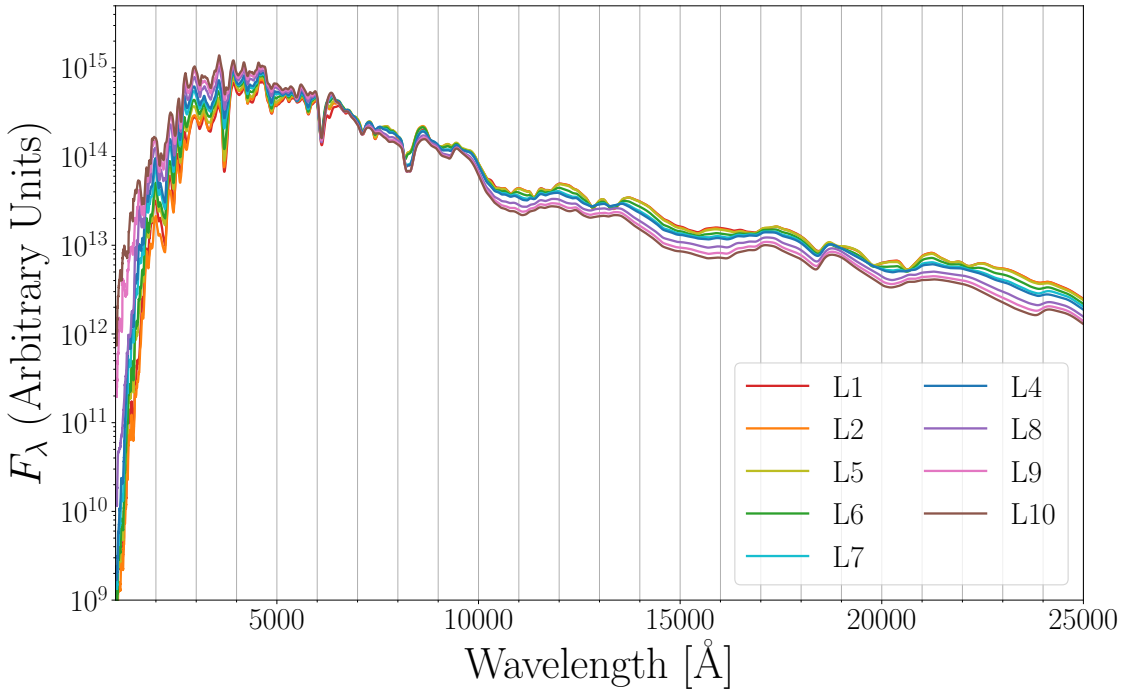

Figure 3.10: Same as Figure 3.9 but showing NIR instead.

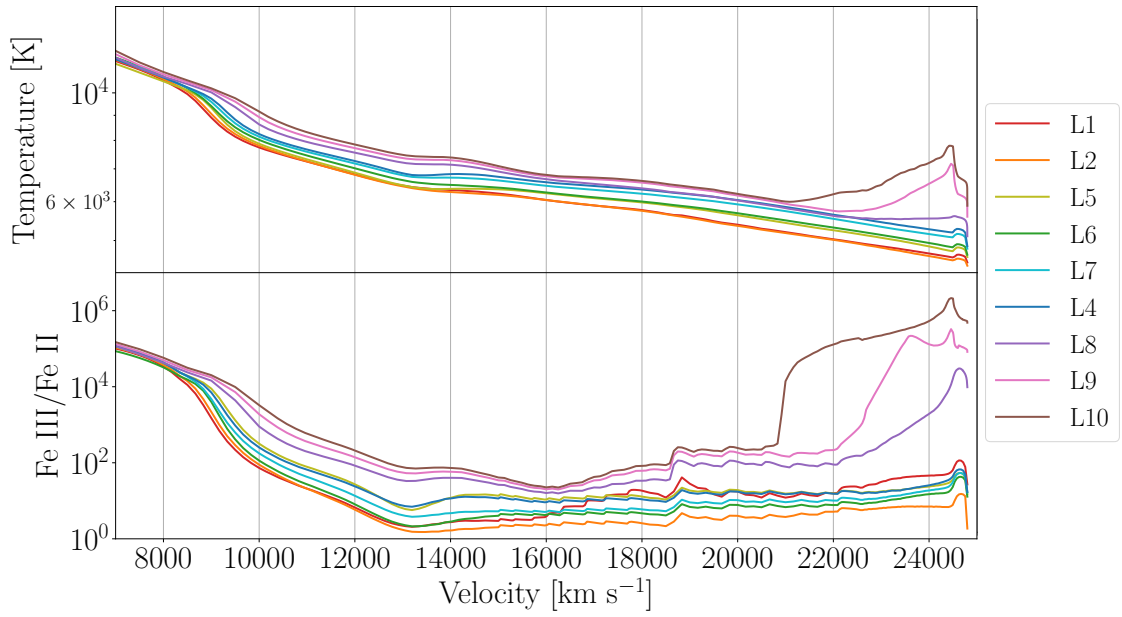

Figure 3.11: The top panel shows the temperature structure of the various models, while the bottom panel shows the ratio of Fe III/Fe II. Below 7000 km s^{-1} all the models have nearly identical temperature structures and ionization balances.

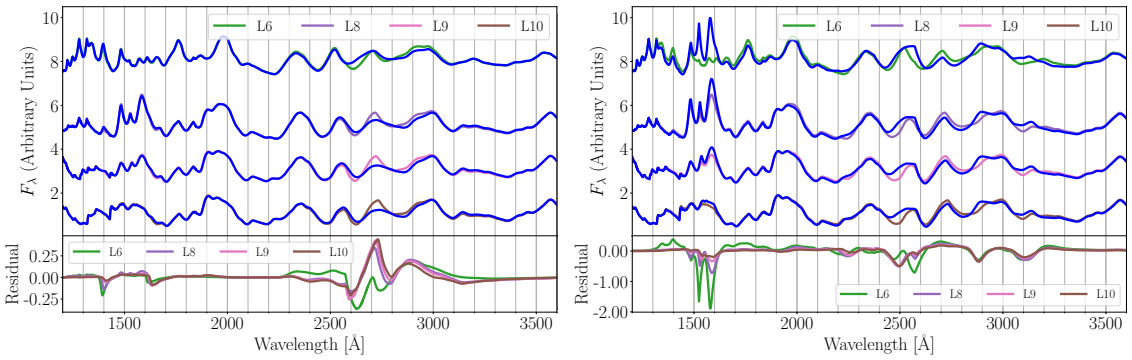

(a) Mg II (b) Fe II

Figure 3.12: Residual plots of Mg II and Fe II as in Figure 3.4 and Figure 3.5 for the L6 (green), L8 (purple), L9 (pink), and L10 (brown) models. The blue line overlaying each model fit is the inverse single-ion spectrum for Mg II (panel a) or Fe II (panel b) for that run luminosity. Residuals between the model and inverse single-ion spectra share the same coloring as the model in the top panel.

Part II

Observational Work

CHAPTER 4

Observational Basics

4.1. Early Observations with POISE

Supernovae (SNe) are the cataclysmic endpoint of massive stars and white dwarfs. As cauldrons of nucleosynthesis, SNe provide the interstellar medium with most of the metallic mass while their enormous kinetic energies ($\sim 10^{51}$ ergs) drive galaxy evolution. With their high intrinsic peak luminosity, SNe serve as excellent cosmological distance indicators to map out the expansion history of the universe. Much of what we know about the physics of SNe and their progenitors is based on observations of objects obtained well past explosion. To expand our understanding of SNe origins, we need rapid-cadence observations obtained in the first few hours-to-days after explosion. These very early phase observations are required to derive key explosion parameters, delineate between leading explosion models, and study the local environment of these cosmic SNe.

4.1.1. Type Ia Supernovae

Only a dozen published normal SNe Ia have been caught within 3 days of explosion and have (B-V) colors (Stritzinger et al., 2018b). The early light curves of these objects reveal significant diversity, including early blue light light-curve bumps, different power law rises, and a bimodality in their intrinsic (B-V) color evolution. Possible explanations of this diversity include: the collision of SN ejecta with a non-degenerate companion, interaction between the SN ejecta and circumstellar material, composition/opacity differences between explosions, different distributions of high-velocity ^{56}Ni, and different progenitor scenarios. However, without spectra, our ability to distinguish between these scenarios is minimal. With spectra in the first few days post-explosion we can detect the outer ($10^{-5} - 10^{-2}$M$_{\odot}$) ejecta to make precise kinetic energy measurements, ascertain the chemical structure, and better understand the accreting surface layer and the physics of its detonation to produce a SN Ia.

4.1.2. Stripped Envelope Supernovae

It is still debated whether stripped-envelope supernovae (SE-SNe) can lose their outer H/He rich envelopes through the stellar winds from massive stars, or if a binary system is required. Observations of some stripped-envelope (Types Ib, Ic, IIb) core-collapse SNe discovered within days of explosion exhibit an initial decrease in luminosity attributed to a rapid cooling phase as the SN adiabatically expands and cools, followed by the rise to primary maximum that takes two or

more weeks. As shown in Stritzinger et al. (2020), only four SNe Ib discovered to date have cooling tails to which models of early time shock cooling combined with radioactive energy deposition can be compared. By increasing this sample of SNe Ib with observed cooling tails, we can use these fits to provide estimates of the progenitor radii, ejecta masses, and ^{56}Ni masses, all of which can be used to expand our understanding of the pre-SN masses and, hence, zero-age-main-sequence masses of the progenitors. Interestingly, the present small sample contains a range of progenitor masses; only with a larger sample might gaps that point to different progenitor systems become apparent. We are keen to expand the current sample size of young SNe Ib, and early spectra are essential to investigate if the outer layers of SNe Ic contain He, and measure the progenitor radii and ejecta masses.

4.1.3. Type II Supernovae

SNe II are the explosions of massive stars ($> 8M_{\odot}$) that have retained a significant portion of their hydrogen envelope. Early photometric (Morozova et al., 2017) and spectroscopic (Yaron et al., 2017) data indicate that many SNe II are surrounded by dense circumstellar material which is connected with increased winds and outflows of massive stars near the end of their lifetimes. The origin of this increasingly violent activity is unknown, with possible sources being unstable burning (Smith & Arnett, 2014) or the driving of wave by convective burning (Fuller, 2017). Multiple spectra within the first 4-5 days after explosion are necessary to detect signatures of three stages of interest: (1) the light flash, which lasts several hours post-explosion, (2) reionization, which lasts hours to several days past explosion, and (3) the hydrodynamical shock front, which can last up to 4 days past explosion (Soumagnac et al., 2019). There is very sparse data at these early phases and spectra are needed for understanding the outer structure, kinematics, and composition of these progenitor stars to provide constraints on the origin of the surrounding circumstellar material, and help develop a more complete picture of how the interiors of massive stars evolve near the end of their lives.

4.1.4. Observational Strategy

The objective of the POISE collaboration is to obtain rapid-cadence, early-phase observations to expand our understanding of supernova explosions and progenitors. The candidates will come primarily from the Zwicky Transient Factory (ZTF) (Bellm et al., 2019) and ATLAS (Tonry et al., 2018) transient surveys. A machine-learning-based alert broker "ALeRCE" (Automatic Learning for the Rapid Classification of Events), developed by collaborators at the Universidad de Chile, will sift through the ZTF (and eventually ATLAS) alert stream to categorize and rank the candidates. To exclude all evolved SNe, we require each candidate to have a non-detection within the previous 2 nights with a detection limit of 20.5 mag. These new candidates are ranked by ALeRCE, whose early

classifier has a 68% success rate at identifying SNe, will be ingested into the 1-m Swope queue via the CSP marshal to obtain images in all of $uBVgri$. This step of Swope pre-screening will confirm the candidate, provide early colors for a preliminary classification, and generate an up-to-date finding chart. In combination with photometry from the search survey, we can determine if the candidate is rising. Candidates that pass the Swope screening will be observed spectroscopically using a global network of telescopes in multiple bandpasses through time acquired by collaboration members. Our contribution to this telescope time is roughly two half-nights each quarter on the APO 3.5m telescope using DIS and KOSMOS to obtain optical spectra. Bright, high-priority objects may also be observed in the NIR using TripleSpec. Our first priority during each APO night is to observe any targets new to the queue that evening, followed by any young, rapidly evolving targets. The remaining time is dedicated to longer term follow-up efforts to contextualize the early time observations by comparing them to the long-term evolution of other well observed objects in the literature. Figure 4.1 shows a flow chart of how the target identification and pre-screening processes would work with Las Campanas resources. Swope will be able to detect all SN candidates with $\delta \lesssim +30$ from ZTF and ATLAS. Objects with $\delta \gtrsim -30$ can be observed from APO, thus we expect significant footprint overlaps between APO and Las Campanas.

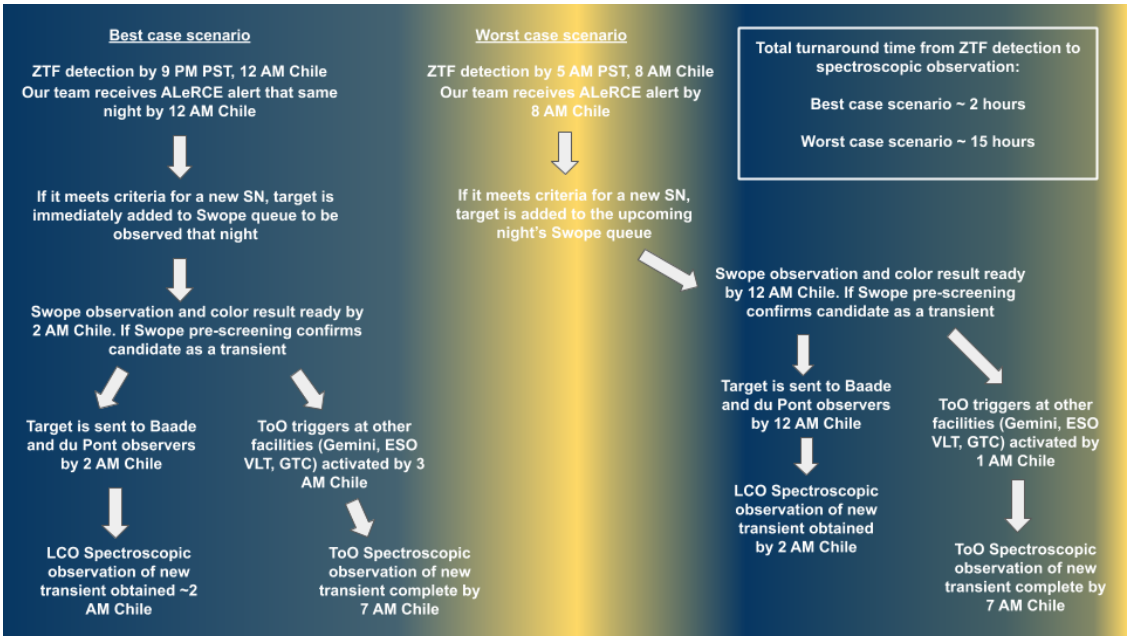

Figure 4.1: Flow chart showing the steps from the discovery of a SN candidate, to pre-screening from the Swope telescope, and to a first spectroscopic observation.

We anticipate being able to obtain spectra with S/N of 15-20 with roughly two hours of total exposure time (one hour each for the blue/red ends of the spectrum), which is sufficient to detect the dominant features of the spectra at this time. Using the Blue VPH Grism with the left slit position

(3700-6200 Å) and the Red VPH Grism with the central slit position (5800-9400 Å) will give a total wavelength coverage of 3700-9400Å, covering all the features of interest between the Ca II H & K lines and the NIR triplet. The increased throughput of KOSMOS-II compared to DIS should allow us to obtain spectra to apparent magnitudes of $\sim 19.5 - 20.0$ mag, which well matches the 20.5 mag lower detection limit of the candidates.

4.2. Nebular Phase Observations

4.2.1. Nebular Spectra of Type Ia Supernovae

Although type Ia supernovae (SNe Ia) have been used to reveal the accelerating expansion of the universe and the presence of dark energy, the explosion mechanism and progenitor systems of these events are still debated. Late-time spectra can help to distinguish between different scenarios. At $\gtrsim 200$ days after peak brightness, a SN Ia enters the nebular phase when the ejecta material becomes optically thin and photons from the far side can travel through to the observer. At this time the spectrum is dominated by forbidden emission lines of iron group elements, such as those of [Fe II], [Fe III], [Co II], [Co III], and [Ni II], which reflect the composition of the inner ejecta regions and provides a unique diagnostic tool for SN Ia explosion models. Emission lines of these species are well covered with the B400/R300 DIS gratings. Several scientific utilities of nebular-phase spectra for SNe Ia exist, including:

1. A direct measure of the ^{56}Ni mass from the FWHM of the strong emission line [Fe III] λ4701, which does not always agree with the ^{56}Ni mass derived from the peak luminosity via Arnett's Law. (Mazzali et al., 2007; Scalzo et al., 2014; Childress et al., 2015; Graham et al., 2015).

2. A test of asymmetric explosion through the relationship between the photospheric velocity evolution and nebular line velocities like those of [Fe II] λ7155 and [Ni II] λ7378 (Maeda et al., 2010). This is, however, challenged by the evidence that the observed diversity is related to the birthplace environments of spectroscopically normal SNe Ia (Wang et al., 2013).

3. Several blends of forbidden cobalt and iron species between 5000-7000 Å can demonstrate bimodality in the transitional and nebular phases, which has been interpreted as direct observational evidence supporting a violent merger of two WD's as the progenitors of Type Ia SNe (Dong et al., 2015; Vallely et al., 2020). However, detailed analysis of nearby nebular phase Type Ia spectra indicate that many of the blended features that appear during the early nebular phase are complex interactions between permitted and forbidden lines of iron group elements that vary with time (Friesen et al., 2017).

4. Searches for embedded hydrogen swept up from the interaction between the ejecta and a non-degenerate companion star shortly after explosion at low velocities (Tucker et al., 2020).

Currently, roughly 70 SNe Ia have nebular spectra, as SNe Ia nearby enough to be bright during the nebular phase are rare. However, wide-field surveys like ATLAS, ASASSN, TNTS (Tsinghua-NAOC transient survey), and PTSS (PMO-Tsinghua Supernova Survey) are finding more nearby SNe in recent years. Various surveys now discover over 70 SNe Ia with z < 0.02 each year combined, with typical luminosities of $\sim$ 19.0 mag in the V band 200 days after maximum light. Spectra of this brightness are obtainable by the APO 3.5-m telescope and DIS. Meanwhile, our collaborating partners at Tsinghua University will collect the early-time photometric and spectroscopic data for these nearby SNe Ia using telescopes with smaller apertures in China. A larger sample with both well-observed early time and nebular-phase spectra can help make further clarification about the origin of the spectral diversity and understand the presence of long-lived radioactive species and the influence of magnetic fields trapping charged particles in the remnant.

4.2.2. Nebular Spectra of Type II Supernovae

SNe II represent the most common subtype of stellar explosions, constituting more than half of all SNe (Li et al., 2011). They are typically divided into those with a light curve that plateaus (IIP) and those that decline linearly (IIL). It is still debated whether this diversity in light curve evolution is related to the mass of the progenitor stars, and whether the less common SNe IIL might be also the explosions of red supergiants. The progenitors of type II supernova are believed to be supergiants, which can be obtained by examining pre-explosion images (Li et al., 2007; Smartt, 2009a) or comparing model predictions with the subsequent cooling curve (Rabinak & Waxman, 2011). As with SNe Ia, nebular spectra of SNe II can be also a powerful tool to constrain the nature of the progenitor stars. At late phases, the line profiles can be used to model the chemical stratification of the ejecta at the time of explosion, and can also reveal the geometry of the explosion and the presence of clumps of material in the ejecta. Additionally, the presence of narrow lines are clear evidence of interaction with material released during the evolution of the star.

There is good agreement between the nebular phase spectra of SN 2012aw and a KEPLER model of $M_{ZAMS} = 15$ M$_\odot$ progenitor star (Jerkstrand et al., 2014). The analysis of synthetic spectra shows that the intensity of a few, relatively isolated lines such as [O I] $\lambda\lambda$6300,6364, Mg I] λ4571, and Na I D $\lambda\lambda 5895, 5889$ in the late-time spectra increases with the mass of the progenitor (Jerkstrand et al., 2015; Valenti et al., 2016) This becomes particularly interesting for SNe with detected progenitors, as the independent estimate of the main-sequence mass from nebular modeling can test the prediction from the progenitor luminosity. That will be a great chance to test stellar evolutionary models and explosive nucleosynthesis theory. Jerkstrand et al. (2015) used this relation to show that most SNe II had a progenitor of mass ≤ 17 M$_\odot$, consistent with direct detection in archival imaging (Smartt, 2015b). This lack of massive SN II progenitors is called the *Red Supergiant Problem*. Further progress in understanding the progenitors of SNe II is dependent on

quality nebular spectra for objects that span the diversity in SNe II. This is now possible thanks to modern wide-field surveys discovering more nearby events and our early-phase monitoring campaign with Tsinghua 0.8-m telescope, NAOC 2.16-m telescope, and LCOGT as part of the SN Key Project, among other all sky surveys.

4.3. High Priority, Unusual, and Exotic Transients

At any given time, there are several transients observable in the sky that are of high value to the broader community. Often, which objects are high-priority is determined by the object's proximity to us, and/or how tightly we can constrain the time of their explosion via a last non-detection from an all-sky survey like ASAS-SN, PanSTARRS, ATLAS, etc. However, objects can be elevated in importance based on whether they receive follow-up in multiple wavelength regimes (e.g. radio, X-ray, gamma rays), received special follow-up with other competitively scheduled instruments (e.g. *Hubble Space Telescope, Kepler Space Telescope)*, or were discovered or associated with multi-messenger signals like those from gravitational waves or neutrino detectors. However, most targets that receive special attention do so because the first few observations reveal behavior that does not cleanly fit into our current understanding of the diversity of transient events. These objects may also be members of newly discovered classes of transients such as Ca-rich transients or "Fast Blue Optical Transients" (FBOTs) for which more data is necessary to categorize their diversity. While not the primary focus of our time requests, several objects that I observed during my time allotments were observed due to these factors, including SN 2018oh and SN 2019ehk, resulting in data contributions to multiple published papers.

4.4. Facilities and Instruments

All of my observations were conducted with the ARC 3.5-m Telescope at Apache Point Observatory (hereafter the APO 3.5m). Through the internal time allocation committee here at OU, I was awarded 43 half-nights of observations over the course of roughly 5 years as part of the departments membership in the Astrophysical Research Consortium, which owns and operates the 3.5-m telescope at APO.

The main purpose of my observations was to acquire optical spectra in service of the science goals outlined in Sections 4.1 and 4.2 using the two spectrographs at APO: the Dual Imaging Spectrograph (DIS) and the repurposed Kitt Peak-Ohio State Multi-Object Spectrograph (KOSMOS). For extremely bright and high-priority objects, we also scheduled observations with the near-infrared spectrograph, TripleSpec. However, due to poor observing conditions these NIR observations failed to yield any scientifically useful data. A brief description of each instrument and its data reduction procedure is provided below.

4.4.1. Dual Imaging Spectrograph (DIS)

The Dual Imaging Spectrograph[1] was the workhorse optical spectrograph for APO 3.5m for many years. Originally designed by Jim Gunn at Princeton and modified by Jeff Morgan and Peter Doherty at University of Washington, the instrument is a dual channel, medium resolution ($R \sim 1000-7000$) spectrograph. A dichoric with a transition value of ~ 5350 Å splits the incoming light into blue and red channels, allowing both halves of the spectrum to be acquired simultaneously.

Our preferred instrumental set-up utilized the default low-resolution grating pair (B400/R300), in combination with the 1.5" slit to provide full coverage of all the important optical lines in supernovae spectra at all epochs, and some coverage into the NIR. After the data are reduced, high quality spectra have a useful coverage from roughly 3400-9800 Å.

The reduction procedure for data acquired with DIS follows the general guidelines for long-slit spectra reduced with IRAF[2]. The data is first overscan corrected and trimmed to remove unilluminated portions of the chip. The data are then bias corrected using the average of a series of zero second exposure images. The images are then flat-field corrected using a set of normalized flat-field images illuminated by a bright quartz lamp. Data are the corrected for cosmic ray hits using the L.A. Cosmic[3] package (van Dokkum, 2001). Spectra are then extracted and wavelength calibrated using a set of arc lamp spectra, which were obtained at the same telescope position as the supernova to minimize flexure in the instrument. Relative flux calibration is performed using spectra of spectrophotometric standards observed the same night at similar airmass to the supernovae. At this point, the two channels can optionally be combined into a single spectra using the overlaping region near the dichoric value to adjust for any offset in the flux calibration.

4.4.2. Kitt Peak Ohio State Multi-Object Spectrograph (KOSMOS-II)

Originally built by The Ohio State University for the 4-m Mayhall telescope at Kitt Peak Observatory, the Kitt Peak Ohio State Multi-Object Spectrograph (KOSMOS[4]) is now on loan to Apache Point Observatory for use on the 3.5-m telescope as a replacement for the older DIS instrument.

At the time of our observations, the instrument was available in a shared risk mode while the final stages of commissioning are finished. As such we experimented with several observational set-ups to determine the optimal set-up for our projects. Our observations with KOSMOS utilized both the 1.18" and 2.10" reflective slits, combined with both the Blue VPH and Red VPH gratings.

[1] https://www.apo.nmsu.edu/arc35m/Instruments/DIS/

[2] IRAF is distributed by the National Optical Astronomy Observatories, which are operated by the Association of Universities for Research in Astronomy, Inc., under cooperative agreement with the National Science Foundation (NSF).

[3] http://www.astro.yale.edu/dokkum/lacosmic/

[4] https://www.apo.nmsu.edu/arc35m/Instruments/KOSMOS/userguide.html

In this set-up, the blue grating produced observations from 3800-6200 Å while the red grating permitted observations covering 5600-9400 Å.

Data from KOSMOS were reduced in following the same procedure as those acquired with DIS, with minor changes to account for the differences in the detector properties of the two instruments.

4.4.3. TripleSpec

TripleSpec[5] is the APO 3.5m's cross-dispersed near-infrared spectrograph. The instrument covers a wavelength rage from $0.95 - 2.46$ μm across five spectral orders.

Observations are performed with the 1.1" slit, corresponding to an spectral resolution of $R = 3500$. Because of the bright sky emission lines from OH and H_20 molecules in the Earth's atmosphere, observations are conducted following the standard ABBA nodding procedure. This procedure places the object at one of two locations (location A or location B) along the slit for exposures averaging no more than 5 minutes. This limit is necessary because the atmospheric emission line are only stable for a few minutes before their strength changes significantly enough to render image subtraction techniques used to remove them ineffective. When done properly, the image subtraction will remove the atmospheric emission, leaving only the object spectra, which can then be combined to produce the observed spectra of the science target. This reduction is performed using the Triplespectool, which is based on the `Spextool` package developed by Michael Cushing for use with the Spex instrument at the Infra-Red Telescope Facility (IRTF). Provided the appropriate calibration images, including bias frames, flat-fielding images, and reference spectra of A0V stars located nearby the science target, Triplespectool will produce one-dimensional, telluric absorption corrected, absolute flux calibrated spectra.

4.5. List of Observations

Table 4.1 lists the results of the 43 nights of observational time for optical and occasional near-infrared spectroscopy on the ARC 3.5m telescope at Apache Point Observatory. During these observations, we collected 125 spectra of 92 unique SNe, resulting in contributions to 12 published papers, with several more currently in preparation. The science case for each set of observations is also listed, corresponding to the details provided in Sections 4.1 and 4.2 of this chapter.

[5] https://www.apo.nmsu.edu/arc35m/Instruments/TRIPLESPEC/

Table 4.1. List of Observations

Date	Science Case	Instrument	Objects Observed
2017-08-20A	Nebular	DIS	SN 2017drh, 2017eaw, 2017egb
2017-08-24B	Nebular	DIS	SN 2017cjt, 2017eaw, 2017ekr, 2017fgc
2017-11-23B	Nebular	DIS	SN 2017egm, 2017emq, 2017gpn, 2017hpu, SN 2017ifh
2017-12-20A	Nebular	DIS	SN 2017fgc, 2017gas, 2017glx, 2017gww, SN 2017hpa
2018-02-09A	Nebular	DIS	SN 2017gmr, 2017hpa, 2018if, 2018oh
2018-05-04B	Nebular	DIS	SN 2018oh, 2018pc, 2018zd, 2018bek
2018-05-05A	Nebular	DIS	SN 2018gk, 2018ast, 2018aye, 2018bek
2018-11-03A	Nebular	DIS	SN 2018zd, 2018zf, 2018fpb, 2018hgd, SN 2018hoy
2018-12-09B	Nebular	DIS	SN 2018zd, 2018hmx, 2018hna, 2018hti, SN 2018ivc
2019-01-08B	Nebular	DIS	SN 2018evt, 2018hfg, 2018hfm
2019-05-07B	Nebular	DIS	SN 2019va, 2019ehk, 2019ein
2019-05-31A	Nebular	DIS	SN 2018evt, 2018hfg, 2019np, 2019ein
2019-08-24B	Nebular	DIS	SN 2018zf, 2018hti, ASASSN-18ey (XRB)
2019-09-25B	Nebular	DIS	SN 2018hti, 2018lkg, 2019muj, 2019pxo, SN 2019osl
2019-09-29A	Nebular	DIS	SN 2018zf, 2019neq, 2019nud, 2019pgo
2019-12-25B	Nebular	DIS	No Observations; Poor Weather
2019-12-28B	Nebular	DIS	No Observations; Poor Weather
2020-03-19B	POISE/Nebular	DIS	SN 2019yvq, 2020ekk, 2020enm
2020-03-20A	POISE/Nebular	DIS	No Observations; Poor Weather
2020-03-27B	POISE	DIS	Observatory Closed Due to Pandemic
2020-04-18B	POISE	DIS	Observatory Closed Due to Pandemic
2020-04-26B	POISE	DIS	Observatory Closed Due to Pandemic
2020-06-02A	POISE	DIS	No Observations; Poor Weather
2020-06-04B	POISE	DIS	SN 2020jhf, 2020kyx, 2020lao*

Table 4.1 (cont'd)

Date	Science Case	Instrument	Objects Observed
2020-07-26B	POISE/Nebular	DIS	SN 2018zf, 2019vxm, 2020nxt
2020-08-23B	POISE/Nebular	DIS	SN 2018zf, 2019vxm, 2020rqk
2020-09-20A	POISE/Nebular	DIS	SN 2018zf, 2020szr, 2020tlf
2020-10-14B	POISE/Nebular	DIS	SN 2020ssf, 2020svn, 2020szr, 2020udy, SN 2020uxz*
2020-10-21B	POISE/Nebular	DIS	SN 2020ssf, 2020svn, 2020szr, 2020udy, SN 2020uxz*
2020-10-25B	POISE/Nebular	DIS	No Observations; Poor Weather
2020-11-09B	POISE/Nebular	DIS	SN 2020ssf, 2020svn, 2020uxz*
2021-02-07A	POISE	DIS	SN 2020adow, 2021bjz, 2021bxu*, SN 2021bzm, 2021cad
2021-02-12A	POISE	DIS	No Observations; Poor Weather
2021-03-11B	POISE	DIS	No Observations; Poor Weather
2021-04-05A	POISE	DIS/TripleSpec	SN 2021dbg, 2021dov, 2021fxy*, 2021gno*, SN 2021hiz
2021-04-12B	POISE	DIS	SN 2021emc, 2021foa, 2021fxy*, 2021gno*, SN 2021hem, 2021hiz
2021-10-26B	POISE	DIS	SN 2021rhu, 2021aatd, 2021abze
2021-12-08B	POISE	DIS/KOSMOS	SN 2021adlv
2021-12-27A	POISE	KOSMOS	No Observations; Poor Weather
2022-03-02B	POISE	KOSMOS	SN 2022dtv, 2022eaf
2022-03-06A	POISE	KOSMOS	SN 2022crv*, 2022dtv, 2022eaf, 2022eat
2022-04-02B	POISE	KOSMOS	SN 2022frl*, 2022frq
2022-04-24A	POISE	KOSMOS	SN 2022crv*, 2022frl*, 2022hrs*

Note. — *Objects for which co-authored papers are in preparation

4.6. Summary of Published Observations

The following section contains brief summaries highlighting the impacts of the data contributions from my observations to several published works for which I received co-authorship.

4.6.1. SN 2018oh

Associated Publications: Li et al. (2019); Dimitriadis et al. (2019); Shappee et al. (2019)

SN 2018oh (ASASSN-18bt) is Type Ia supernova discovered by the ASAS-SN collaboration on 2018 February 4.41 (MJD=58456.41) (Brown et al., 2018). In addition to being a nearby SNe Ia ($z \sim 0.011$), SN 2018oh was discovered within the active field of the *Kepler Space Telescope* as part of its *K2* mission. While *Kepler's* primary mission is to continually monitor patches of the sky to look for transiting exoplanets with a thirty minute cadence, it also provides unprecedented observations of astrophysical transients like SN 2018oh which happen to appear in its current field of view. The resulting light curve provides the most accurate constraints on of the time of first light, and the most detailed observations of the early light curve for any SNe Ia to date.

It is from this detailed early light curve that we discover that SN 2018oh is part of small group of SNe Ia with a so-called early-time excess, where the observed fluxes exceed those expected under the simple "fireball" explosion model (Arnett, 1982). As one of only a few objects to date with early enough photometry to detect this early excess, SN 2018oh was the subject of great interest in the supernova community. Through our APO time, we obtained two spectra of SN 2018oh, one of which was published in Li et al. (2019), as part of a community wide collaboration consisting of three papers to characterize both the observed properties and explain the source of the early excess emission.

As part of Li et al. (2019), which characterizes the photometric and spectroscopic properties of SN 2018oh, I performed SYNOW fitting to identify and characterize the appearance of C II lines near maximum light in the optical spectra of SN 2018oh. A modified version of Figure 13 from Li et al. (2019) showcasing these fits is shown in Figure 4.2.

These fits illustrate that C II is present prior to maximum light, starting in the -8.5d spectra. However, by maximum light, the C II becomes so weak as to be virtually unidentifiable. After maximum light, the C II feature begins to strengthen again and is present through the $+8.0$d spectrum.

The simultaneously published papers of Dimitriadis et al. (2019) and Shappee et al. (2019) used the *Kepler K2* photometry to investigate the source of the early time excess, coming to different conclusions. Dimitriadis et al. (2019) find that while all three major early excess models (^{56}Ni mixing, CSM interaction, and interaction with the binary companion star) are generally able to

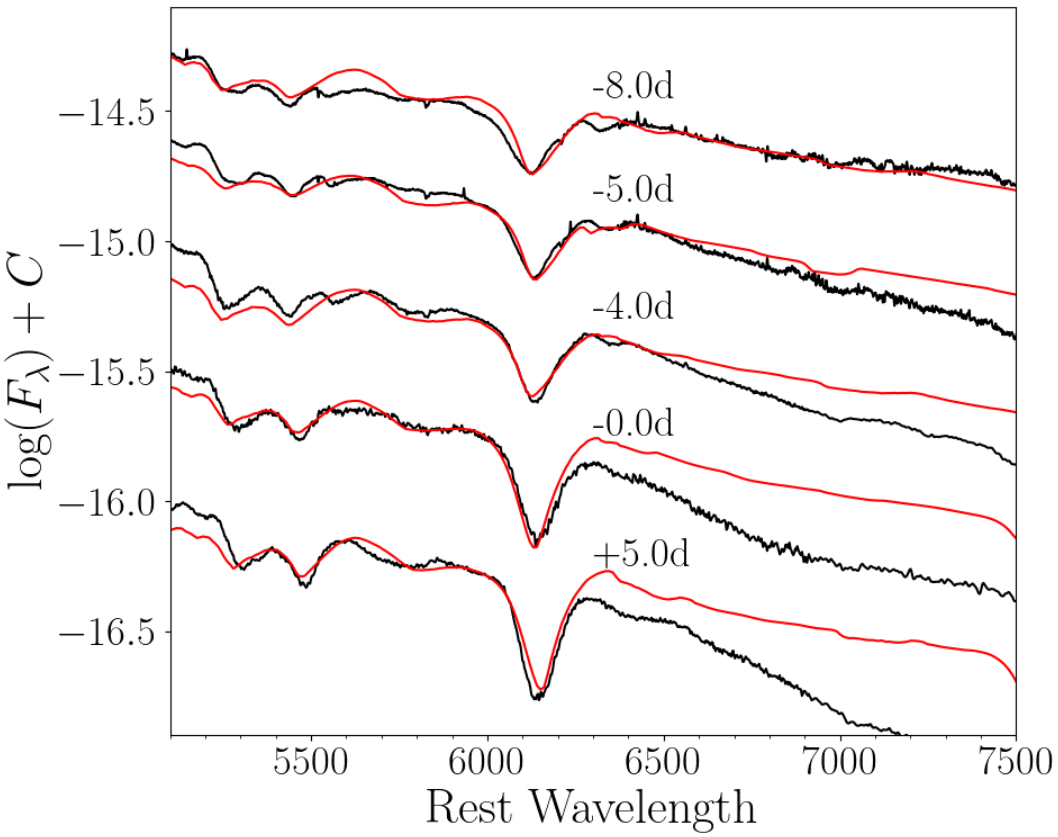

Figure 4.2: SYNOW fits to optical spectra of SN 2018oh, centered on the C II λ6580 line.

reproduce the early light curve, they find the best agreement with a $1 - 6$ $M_\odot$ companion star at a separation of 2×10^{12} cm, dependent on viewing angle, which would indicate that SN 2018oh arose from the single-degenerate channel. Shappee et al. (2019) instead favor a model with enhanced ^{56}Ni mixing, with the outer 0.05 $M_\odot$ of the ejecta having a ^{56}Ni fraction of 0.15-0.2. In order to match other aspects of the early photometry, SN 2018oh must arise from a double detonation model with a small amount of radioactive material near the surface. To date, late time observations meant to distinguish between these two potential progenitor scenarios have favored a double degenerate progenitor system (Tucker et al., 2019).

4.6.2. SN 2017ein

Associated Publications: Xiang et al. (2019)

SN 2017ein was a nearby ($z = 0.0027$) Type Ic supernova (SN Ic) which was discovered less than a day after the estimated explosion. The early photometry and spectroscopy in these first few days after explosion detail a small amount of excess emission, which is interpreted as cooling from the shock breakout, and allows us to estimate the size of the progenitor star and the ejecta mass of the SN. Additionally, the host galaxy, NCG 3938, was previously observed by *HST*, allowing the archival photometry to be searched for evidence of the progenitor star, from which independent estimates of the properties of the progenitor star can be obtained. While the low resolution of the *HST* data prevents a conclusive determination of the nature of the underlying source identified in the pre-explosion images, the combination of the ejecta estimate from shock breakout modeling ($M_{ej} \sim 1 M_\odot$, $R_{progenitor} = 8 \pm 4 R_\odot$), favor a compact Wolf-Rayet star or a star in a binary system.

We contributed one spectrum of SN 2017ein, taken $+90.0$ days after explosion ($+73.6$ days after B-band maximum). This spectra can be found in Figure 9 of Xiang et al. (2019). At this epoch, the spectrum is characterized by prominent Na I, O I and numerous Fe II lines.

4.6.3. SN 2018ivc

Associated Publications: Bostroem et al. (2019)

SN 2018ivc is another nearby supernova ($z = 0.0034, d = 10.1$ Mpc), which was discovered within a few days of explosion, and has archival *HST* images of the host galaxy prior to the supernova explosion. No source is identified in these pre-explosion images. Multi-band follow-up of the supernova revealed a linearly declining light curve which changes slope several times in the first ~ 40 days after discovery. X-ray observations from the Chandra X-ray Observatory reveal a emission from the same location as the supernova, indicating that the supernova is likely undergoing interaction with nearby circumstellar material. This is confirmed by early spectroscopic observations

which reveal a blue continuum with several narrow features, including H_α, H_β, and He I lines. Roughly a week after explosion, broad features revealed SN 2018ivc to be a Type IIL SN. Beginning with our APO observations $+18.1$ days after explosion, high velocity features begin to appear in the spectra in the H_α, H_β, and He I $\lambda5876$ and Ca II NIR triplet features; further confirming the presence of CSM. The full APO spectrum can be seen in Figure 4 of Bostroem et al. (2019), and the high velocity features present in the spectra are highlighted in Figure 9.

When the upper limits of the pre-explosion *HST* images are combined with the optical spectra, they restrict the progenitor to be relatively low mass ($M < 8$ M$_\odot$) at the time of explosion, assuming the progenitor was a single star. The presence of strong He lines, which are not always present in SNe II, indicate the the progenitor likely had much of its envelope stripped prior to explosion. Since massive stars are more likely to form in binary systems, and their interaction can enhance mass loss, if stars in binary systems are considered possible progenitors, the progenitor may be as massive as $M < 12$ M$_\odot$ at the time of explosion.

4.6.4. SN 2019ehk

Associated Publications: Jacobson-Galán et al. (2020)

SN 2019ehk is a Ca-rich transient which exploded in the nearby galaxy M100 ($d \sim 16.2$ Mpc), which was discovered less than a day after explosion, and for which pre-explosion imaging from *HST* exists. This early discovery and the ensuing rapid, multi-wavelength follow-up make SN 2019ehk the best observed Ca-rich transient to date. Observations reveal a rapid rise to a first peak with concurrent detection from the Chandra X-ray observatory. The light curve then rapidly declines before rising to a secondary peak. Spectroscopic observations at early times reveal flash-ionized H and He lines, further confirming the presence of CSM interaction. Our -3.0 day spectra from APO is similar to other near-maximum spectra of SN 2019ehk and other Ca-rich transients in the literature, with strong He I, Ca II, and O I lines, and strong line blanketing in the blue half of the optical from Ti II, Fe II and Fe III lines. The full spectrum can be found in Figure 12 of Jacobson-Galán et al. (2020).

The totality of the observations restrict the progenitor of SN 2019ehk to a narrow range. Modeling of the optical properties reveal that $M_{ej} \approx 1$ M$_\odot$ with $M_{CSM} = 1.5 \times 10^{-3}$ M$_\odot$ at a radius of $R_{CSM} = 4 \times 10^{13}$ cm. The upper limit is from the pre-explosion *HST* imaging rule out single massive stars with mass > 8 M$_\odot$, and only allow for massive stars in a binary system with masses between $9.5 - 10$ M$_\odot$ or low mass He-stars which have had their envelopes stripped. Spectral differences compared to SNe Ia rule out most C/O WD explosion models, except for those where a low mass (M $\approx 0.5 - 0.6$ M$_\odot$) C/O WD explodes within the debris of another recently disrupted C/O WD or a hybrid He/C/O WD. Further observations and modeling of Ca-rich transient systems

is necessary to help narrow down the possible progenitor scenarios.

4.6.5. SN 2018hti

Associated Publications: Lin et al. (2020)

SN 2018hti a Type I superluminous supernova (SLSN-I), originating in an unnamed low-metalicity dwarf galaxy at $z = 0.0612$. SLSN are characterized by their high absolute luminosities, which can be 10-100 times brighter than SNe Ia. Like other varieties of SNe, they are classified as Type I (H-deficient), and Type II (H-rich) based on their optical spectra. It is assumed that these two types of SLSNe arise from different progenitor populations, and have different power sources that drive their evolution. We contributed two nebular phase spectra of SN 2018hti to Lin et al. (2020), one taken $+255.8$ days after explosion, and another at $\sim +288$ days, which went unpublished due to low signal, as the supernova faded below our detection threshold at APO. The 255.8 day, for which only red channel data was obtained, shows prominent [O I] and [Ca II] lines, as well as narrow H_α lines from the host galaxy. This spectrum can be found in Figure 3 of Lin et al. (2020).

Modeling of the light curve reveal that a magnetar model with a magnetic field of 1.8×10^{13} G and a rotational energy $E_{rot} = 8 \times 10^{51}$ erg embedded in a 5.8 $M_\odot$ ejecta can reproduce the observed data. Assuming an average mass magnetar, the pre-explosion mass of the C/O star was roughly 7.2 $M_\odot$. This implies a single star progenitor with ZAMS mass of $\sim 16 - 25$ $M_\odot$ or a star in a binary system with mass > 25 $M_\odot$. These derived values generally of the ejecta, and the low metalicity host agree with other well observed SLSNe-I. New all sky surveys like ZTF and the Vera C. Rubin Observatory's LSST should reveal many more SLSNe which will allow us to better understand the diversity and properties of SLSNe.

4.6.6. SN 2018zd

Associated Publications: Zhang et al. (2020)

SN 2018zd is a Type II supernova with several unique properties that make it difficult to classify in the SNe II landscape. It was discovered an estimated ~ 3 hours after explosion by amateur astronomer Koichi Itagaki, with the first spectrum taken another 3 hours after discovery. Other observations from amateur astronomers in a clear filter of the host galaxy NGC 2146 reveal a possible detection roughly 1 day prior, with a deeper non-detection limit in-between the possible detection and the discovery; suggesting that the object is both quite young and experienced a shock break-out prior to discovery. Early spectra revealed a blue continuum with several narrow, flash ionized lines, including N V $\lambda\lambda 4334, 4641$, He II $\lambda 4686$, $\lambda 4860$, and C IV $\lambda\lambda 5801, 5812$, $\lambda 7110$. These early spectra also show marginal detection of narrow H_α lines in the first few spectra, which

become stronger over time, indicating that CSM interaction begins soon after explosion. Based on these lines, SN 2018zd was classified as a Type IIn.

Photometric observations of SN 2018zd reveal a linearly declining light curve, reminiscent of a SN IIL. However, nebular phase spectra, of which we contributed two spectra from APO taken $+248$ and $+284$ days after explosion, suggest that SN 2018zd behaves similarly to SN IIP. These spectra can be found in Figure 3 of Zhang et al. (2020). When these and other nebular phase spectra are compared to the nebular phase models of Jerkstrand et al. (2012), they suggest that the progenitor was a massive star with a mass on the lower end of the $12 - 15 M_{\odot}$ range. This low progenitor mass estimate, and the disagreement between photometric and spectroscopic data, and the early time flash ionization features suggest that SN 2018zd may lie on the border of the IIL/IIP classification divide, or possibly be related to more exotic stellar explosions like electron capture supernovae. Ultimately, events like SN 2018zd provide an important opportunity to better understand the diversity of SNe II.

4.6.7. SN 2018hfm

Associated Publications: Zhang et al. (2022a)

SN 2018hfm is a somewhat unusual SN II, which exploded in a nearby dwarf galaxy with a subsolar (~ 0.5 $Z_{\odot}$) metalicity. It experienced a ~ 3 mag drop in the optical bands roughly 50 days after explosion as it transitioned from the plateau phase to a underluminous tail phase. Just before this transition occurs, a small bump appears in the g and V bands, which spectra taken during before, during, and after reveal is due to the formation of a broad, boxy, and asymmetric H_{α} line. This boxy H_{α} feature comes to define the later phase spectra, along with a similarly boxy and asymmetric [Ca II] emission line, including our APO spectra taken at $+97.3$ days after explosion, and likely arises from the SN ejecta interacting with nearby circumstellar material. The spectrum can be seen in full in Figure 3 of Zhang et al. (2022a), with more detailed characterizations of the line profiles found in Figures 12, 15, and 16.

Through the combination of modeling of the bolometric light curve and the line profiles of the H_{α} and [Ca II] lines that dominate the late time spectra, we are able to extract information about the characteristics of the supernova eject. From the light curve models, it is estimated that SN 2018hfm has a low ejecta mass ($M_{ej} =\sim 1.3$ $M_{\odot}$), with very little synthesized ^{56}Ni. The asymmetric line profiles offer the chance to investigate the amount of early dust formation in SN 2018hfm; as SN II are expected to be major contributors to the dust found in galaxies. The simple models estimate that the amount of dust produced by the ejecta increased from $\sim 10^{-6}$ $M_{\odot}$ at $+66.7$ days to $\sim 10^{-4} - 10^{-3}$ $M_{\odot}$ at $+389.4$ days; which is in agreement with the estimates of dust estimates in other SN II at similar phases.

4.6.8. SN 2019va

Associated Publications: Zhang et al. (2022b)

SN 2019va is a SN IIP, with some abnormal characteristics in its V-band light curve. The "plateau" phase of the light curve, which can last until roughly 100 days after explosion, has an unusually low decline rate of -0.02 ± 0.02 mag (100 d)$^{-1}$ relative to other SN IIP. Additionally, in the days before SN 2019va transitions out of the plateau phase and into the tail phase, the pseudo-bolometric light curve shows a small bump, indicating the presence of an additional power source beyond the energy released by H recombination. Spectroscopically, SN 2019va is similar to other SN IIP with low decline rates during the plateau phase. We contributed one spectra at $+114.7$ days relative to the inferred explosion date, which occurs right as the SN transitions between the plateau and tail phases. This spectra can be found in Figure 3 of Zhang et al. (2022b). While the spectra still has prominent Balmer features like spectra taken during the plateau phase, strong Na I and other metal lines have become prominent in the blue portions of the optical; an indicator that the SN has a low metalicity progenitor (Dessart et al., 2014; Anderson et al., 2016). This is supported by the inferred host galaxy metalicity determined from spectroscopic observations (0.46 ± 0.06 $Z_{\odot}$).

Modeling of the plateau phase of the light curve reveals that SN 2019va has a larger ^{56}Ni mass (0.088 ± 0.018 $M_{\odot}$) than 90% of SN II examined by Rodríguez et al. (2021). Using the η_{Ni} parameter of Nakar et al. (2016), which measures the relative influence of ^{56}Ni on the plateau phase, we find that SN 2019va has the second largest value ($\eta_{Ni} = 0.80$) of the 39 SN IIP sampled in this paper. Other SN IIP with large values of η_{Ni} and similar photometry and spectra also appear to reside in low metalicity hosts. However, further observations of SN IIP in low metalicity hosts are needed to increase the sample size before a definite connection can be established.

4.7. Other Results

4.7.1. Classification Reports

Our observations have also led to the classification of two supernovae; SN 2018bek and SN 2021bxu. Prompt follow-up observations of new SN targets provide two services to the community. The first is that the classification spectra allow for the SN to be included as a data product for any surveys which capture the SN in their observations. The second is to assist the community in best allocating their follow-up resources based upon the science questions they are actively investigating.

The first target we classified was SN 2018bek from observations at APO on the night of 2018-05-05. Combined with the observations of our collaborators that same night at other facilities, SN 2018bek was classified as a young SN II based on its blue continuum and weak, broad hydrogen

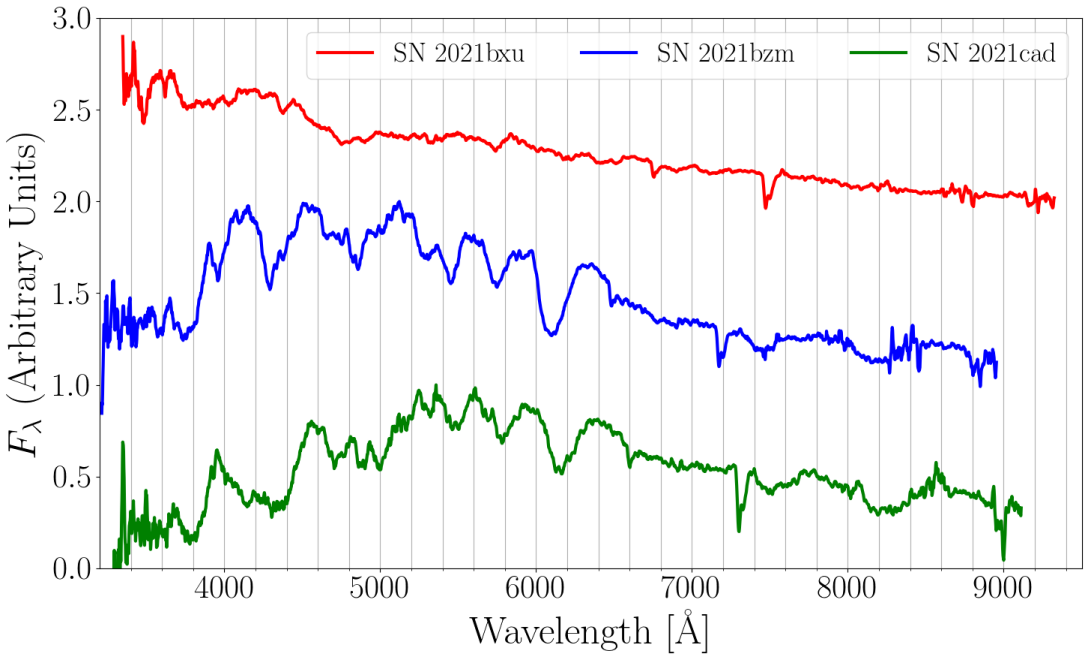

Figure 4.3: Optical spectra of SNe 2021bxu, 2021bzm, and 2021cad. All three targets were observed on the night of 2021-02-07, and were unclassified at the time of observation. SN 2021bxu was classified as a young SN IIb, while SN 2021bzm was classified as a SN Ia and SN 2021cad was classified as a 91bg-like SN Ia based on the broad, flat Ti II absorption feature between $\sim 4000 - 4400$ Å.

Balmer lines.

The second target we classified through our APO observations was SN 2021bxu from observations taken on 2021-02-07. The spectrum is reminiscent of a blue continuum, with a break at ~ 4725Å. Weak features corresponding to H and He lines identified using `SYNOW`. Using the spectral classification program Muthukrishna et al. (2019, `DASH`), we find $> 99\%$ agreement between the spectra of SN 2021bxu and other Type IIb supernova objects between -18 and -14 days prior to maximum light, including SNe 1993J and 2011fu. Given the young age of the supernova, it is possible this break in the spectrum is an indication that the SN was undergoing shock breakout at the time of the observations (DerKacy, 2021).

SN 2021bxu is currently the subject of a POISE collaboration follow-up paper led by a graduate student at the University of Hawaii.

4.7.2. SN 2019ein

SN 2019ein is a SNe Ia we observed twice with APO during May of 2019. SN 2019ein was classified as a "broad-line" (Ia-BL) within the Branch classification scheme by (Burke et al., 2019), who also noted the unusual broad, blueshifted, and high velocity features in their classification

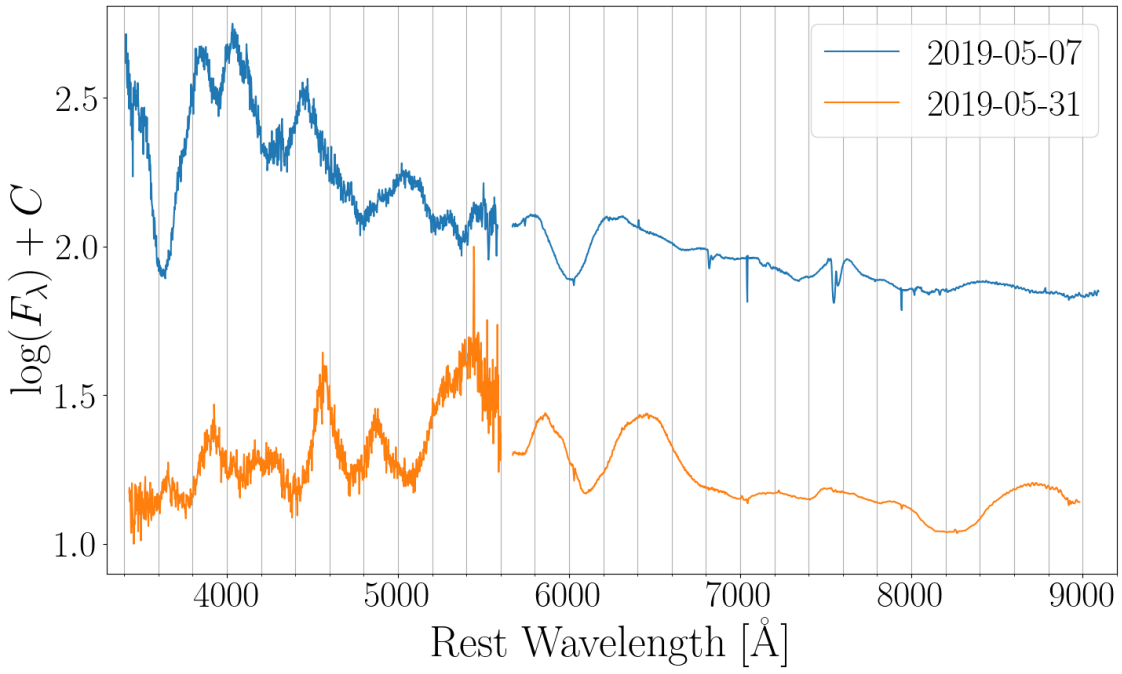

Figure 4.4: Optical spectra of SN 2019ein taken on the nights of 2019-05-07 (blue) and 2021-05-31 (orange).

spectrum. The cause of this blueshift, which causes SN 2019ein spectra to resemble a Doppler shifted version of a "core-normal" spectra, is currently the focus of two papers using different codes. Z. Yarbrough et al. (in prep) examines the the physical differences necessary to produce this blueshift using `SYNOW`, while J. DerKacy et al. (in prep.) examines the physical differences between two models proven to reproduce the CN (Baron et al., 2015; DerKacy et al., 2020) and BL (Baron et al., 2012) spectral characteristics using `PHOENIX`. A summary of this work is presented in Appendix A. For further reading on SN 2019ein, the photometric and spectroscopic properties of SN 2019ein have been well studied by Kawabata et al. (2020) and Pellegrino et al. (2020).

CHAPTER 5

SN 2021fxy: Mid-Ultraviolet Flux Suppression is a Common Feature of Type Ia Supernovae

This chapter is a version of DerKacy et al. (2022), which is currently under review. It has been modified from the submitted version to improve readability, including removal of the paper abstract.

5.1. Introduction

Type Ia supernovae (SNe Ia) are important astrophysical objects because of their utility as "standardizable candles" for cosmological studies. The empirical Phillips relation (Phillips, 1993; Phillips et al., 1999) allows them to serve as cosmological probes, revealing the accelerating expansion rate of the universe (Riess et al., 1998; Perlmutter et al., 1999). While it is well established that SNe Ia are explosions of a primary carbon and oxygen (C/O) white dwarf in binary systems (Hoyle & Fowler, 1960), the full nature of the progenitor system, including the nature of the secondary star, is still unclear (for a review see Maoz et al., 2014). In the single-degenerate (SD) scenario, the companion is either a main-sequence star or an evolved, non-degenerate companion like a red giant or He-star. Through accretion, the white dwarf approaches the Chandrasekhar mass, and eventually explodes via a deflagration-to-detonation transition (Hoeflich et al., 1995; Höflich, 2002, 2006). In the double-degenerate (DD) scenario, the companion is also a white dwarf, where the combined mass of the system equals or exceeds the Chandrasekhar mass and the explosion is triggered by the merger of the two WDs (Iben & Tutukov, 1984; Webbink, 1984). In dense stellar environments like globular clusters, the interaction of the two WD's may happen "violently", resulting in a collision of the two WD's before they are able to fully merge (Rosswog et al., 2009; Pakmor et al., 2010, 2012). However, these violent mergers produce ejecta that are more asymmetric than observed SNe Ia (Chu et al., 2022; Livneh & Katz, 2022; Patra et al., 2022). More recent models have suggested that SNe Ia may potentially originate from the merger of a WD with the core of an evolved star (the so-called core-degenerate scenario) (Kashi & Soker, 2011; Soker et al., 2014), or alternatively from the detonation of He on the surface of a sub-Chandrasekhar mass WD (Thielemann et al., 1986; Shen et al., 2018; Polin et al., 2019).

Near maximum light there are several different schemes to characterize the observed diversity of SNe Ia. Branch et al. (2006) subdivide SNe Ia into four groups: core-normal (CN), shallow silicon (SS), broad line (BL), and cool (CL); based upon the pseudo-equivalent widths (pEWs) of the Si II $\lambda 5972$ and $\lambda 6355$ lines in their spectra near maximum light. Recent work with larger samples have

shown these groups to be statistically robust (Burrow et al., 2020) and are potentially related to differences in the progenitor systems and/or explosion mechanisms (Polin et al., 2019). Wang et al. (2009) divide SNe Ia into "Normal" and "High Velocity (HV)" groups based on the velocity of the Si II absorption minimum near B-band maximum light, with the HV objects showing redder $B-V$ colors and less scatter in peak luminosity and luminosity decline rate (Δm_{15}) relative to Normal SNe Ia. Benetti et al. (2005) divide the SNe Ia population into "Faint", "LVG" and "HVG" groupings based on the combination of their decline rate in B-band and the rate of change in their Si II velocity.

Early observations are key to determining the connections between the observed SNe Ia diversity and different progenitor scenarios and explosion mechanisms. Early observations can probe the physical properties of the system, including constraints on the size of the WD progenitor (Nugent et al., 2011; Bloom et al., 2012) or the type of secondary star (Kasen, 2010; Maeda et al., 2014). Early photometric observations of nearby SNe Ia discovered within hours of explosion have revealed that some SNe Ia (such as SNe 2017cbv, 2018oh, 2019np, and 2021aefx) show an early excess or "blue bump" at early times (Hosseinzadeh et al., 2017; Li et al., 2019; Sai et al., 2022; Ashall et al., 2022; Hosseinzadeh et al., 2022). However, there are multiple potential origins of these early time excesses, including outward mixing of ^{56}Ni in the ejecta (Piro & Morozova, 2016; Shappee et al., 2019), production of radioactive material in the detonation of the helium shell (Dimitriadis et al., 2019; Polin et al., 2019), interaction with the companion (Kasen, 2010; Maeda et al., 2014; Dimitriadis et al., 2019), and rapid velocity evolution of broad, high-velocity spectroscopic features (Ashall et al., 2022). Attempts to probe the companion interaction in the radio have yet to detect a companion interaction, but have yielded information on the nearby circumstellar environment in the first days after explosion and provided constraints on the wind properties of the progenitor (Lundqvist et al., 2020; Hosseinzadeh et al., 2022)

Color curves derived from these early observations of SNe Ia within the first few days after explosion reveal at least two different populations, distinguishable by their $B-V$ behavior (Stritzinger et al., 2018b). Of the two most populous groups, one group of SNe Ia starts out blue and stays blue, while the other group start out red and rapidly become bluer and become indistinguishable from those that started out blue roughly 6 days after first light. This behavior is not replicated in $g-r$ colors (Bulla et al., 2020). Observations within these first few days after explosion probe the outermost ejecta layers where differences between models of SNe Ia are largest. For example, a SD DDT model is expected to have unburned carbon, oxygen, and potentially silicon in the outermost layers (Hoeflich et al., 2017) compared to the large amounts of ^{44}Ti and ^{56}Ni which are the expected by-products of models relying upon surface helium detonations (Jiang et al., 2017). In the models of Polin et al. (2019) these by-products produce significant line blanketing, resulting in red colors at early times.

SNe Ia diversity increases as one moves from optical to ultraviolet (UV) wavelengths. Photometrically, SNe Ia can be divided into two groups based on their NUV colors; the NUV-blue group, whose members have low velocity gradients of their Si II $\lambda 6355$ lines and conspicuous C II lines, and the NUV-red class, whose members have more diverse Si II velocity gradients and typically lack the C II lines (Milne et al., 2013). The fraction of events belonging to each group varies by redshift, making it difficult to incorporate UV data of SNe Ia into cosmological analyses (Milne et al., 2015; Brown et al., 2017). Spectroscopically, SNe Ia can show drastic differences in the UV despite being almost identical in the optical and NIR. The best example of this is the "twin" SNe 2011by and 2011fe (Foley & Kirshner, 2013). Theoretical efforts to better understand UV spectral formation have focused on the impacts of three key variables: (1) metallicity – increases in the progenitor metallicity strengthen line blanketing in the UV and result in lower fluxes (Lentz et al., 2000), (2) density structure – shallower density profiles produce UV spectra with lower flux values and fewer features (Sauer et al., 2008; Hachinger et al., 2013; Mazzali et al., 2014), and (3) luminosity – which induces temperature variations that change both the shape of the underlying continuum and the strength, shape, and location of spectral features (Walker et al., 2012; DerKacy et al., 2020).

In this work, we present observations and analysis of SN 2021fxy, an NUV-red SNe Ia discovered roughly 2 days after explosion and for which we obtained multiple *HST*/STIS UV spectra in addition to a comprehensive multi-band follow-up effort by the Precision Observations of Infant Supernova Explosions (POISE, Burns et al. (2021)) collaboration. Section 5.2 details these photometric and spectroscopic follow-up observations, followed by a detailed analysis in Section 5.3, including comparisons to the sample of spectroscopically normal SNe Ia with *HST* UV spectra near maximum light. In Section 5.4 we compare SNe 2021fxy and 2017erp, both of which are well-observed NUV-red SNe Ia with *HST*/STIS spectra, and who show nearly identical optical properties. We discuss the potential causes of their observed differences in the context of the UV diversity of SNe Ia and what they reveal about the origins of this diversity. We summarize our conclusions in Section 5.5.

5.2. Observations

5.2.1. Discovery

SN 2021fxy was discovered on 2021-03-17T17:23:37.0 by Koichi Itagaki at $m = 16.9$ mag in a clear filter (Itagaki, 2021), and classified as a young SN Ia the following night (Jha et al., 2021). SN 2021fxy is located at $\alpha = 13^h13^m01^s.570$, $\delta = -19°30'45''.18$, which is $19''.8$ North and $8''.1$ East from the center of the host galaxy, NGC 5018. The most constraining last non-detection comes from ASAS-SN on 2021-03-15T10:56:43.584 in the g band at $g > 17.946$ mag, which was

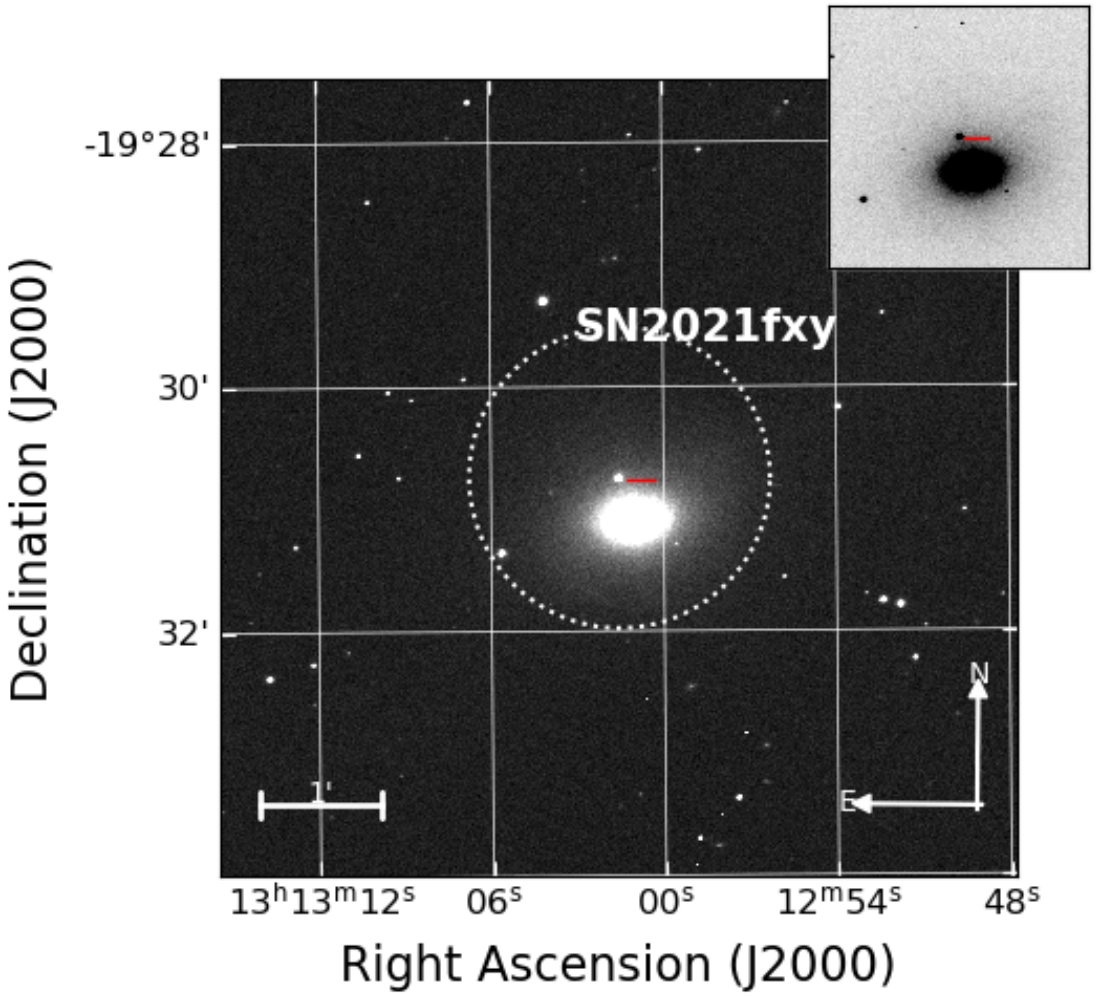

Figure 5.1: An r-band image of NGC 5018 taken with the Swope 1-m telescope at Las Campanas Observatory, Chile. SN 2021fxy is highlighted in both the main panel and the false-color inset with a red dash.

retrieved from the ASAS-SN Sky Patrol Database[1] (Shappee et al., 2014; Kochanek et al., 2017). This implies SN 2021fxy was discovered no later than 2.27 days after explosion, assuming there is no dark phase.

NGC 5018 is classified as an E3 according to de Vaucouleurs et al. (1991), at a redshift $z = 0.0094$ (Rothberg & Joseph, 2006). Correcting the velocities for local motions based on Mould et al. (2000) and assuming a $H_0 = 73$ km s^{-1} Mpc^{-1} (Riess et al., 2021), this redshift results in a Hubble flow distance of 38.4 ± 2.7 Mpc, corresponding to a distance modulus of (m-M) $= 32.92 \pm 0.15$ mag. SN 2021fxy is at least the second SNe Ia hosted by NGC 5018, along with the well-studied 2002bo-like SN 2002dj (Pignata et al., 2008) and SN 2017isq, a SN Ia discovered roughly one month after maximum light for whom NGC 5018 is the closest potential host at an estimated separation of 30 kpc (Tonry et al., 2017; Benetti et al., 2017).

5.2.2. Photometric Follow-up

5.2.2.1. Ground-based Photometry

The POISE collaboration began a multi-band ($uBVgri$) follow-up campaign of SN 2021fxy using the Swope 1-m telescope at Las Campanas Observatory at 2021-03-18T02:43:41.088, just 0.39 days after discovery, placing our first observations no later than 2.66 days after last non-detection. During the early rise, two sets of observations were taken per night to capture rapid, intra-night evolution. Roughly one week after discovery, the cadence was reduced to one set of observations per night. Observations from the Swope were reduced and analyzed according to the procedures of Krisciunas et al. (2017) and Phillips et al. (2019).

Some post-maximum photometric observations in $BVgri$ bands were taken using the Las Cumbres Observatory global 1-m telescope network as part of the Aarhus-Barcelona FLOWS project.[2] This data was reduced with the BANZAI pipeline (McCully et al., 2018) and calibrated using the local sequence photometry from the Swope observations, assuming zero color terms.

Photometry from both telescopes in their natural system are presented in Section 5.6. The photometry has also been S-corrected (Stritzinger et al., 2002) to the CSP-I natural system, and is used throughout the photometry plots in this paper. This S-corrected photometry is also presented in Section 5.6. In $BVgri$ bands, the magnitude of the S-corrections is quite small ($\lesssim 0.01$ mag). However, in the u band, the S-correction grows larger with time, eventually growing to ~ 0.04 mag $+12$ days after maximum light. More details on the S-corrections can be found in Section 5.6.

[1] https://asas-sn.osu.edu/
[2] https://flows.phys.au.dk/

5.2.2.2. *Swift* Photometry

Swift observations were first triggered as part of the Swift GI program "Maximizing Swift's Impact With The Global Supernova Project" (PI: Howell). Observations began on 2021-03-18T05:55:47. Due to the brightness of the underlying host galaxy, some optical observations were made in a hardware mode with a faster readout to reduce the effect of coincidence loss. Photometry was computed with the the Swift Optical Ultraviolet Supernova Archive (SOUSA; Brown et al., 2014) pipeline using the 2020 update to the time-dependent sensitivity and aperture corrections calculated in 2021. No subtraction of the host-galaxy flux has been performed due to the lack of pre-explosion images.

5.2.3. Spectroscopic Follow-up

5.2.3.1. Optical Spectroscopy

Optical spectroscopic follow-up observations, covering -6.0 days to $+45.8$ days relative to the epoch of B-band maximum were made with a global network of telescopes and instruments, including DIS on the Apache Point Observatory 3.5-meter telescope, which is owned and operated by the Astrophysical Research Consortium (ARC 3.5m), ALFOSC on the Nordic Optical Telescope (NOT) by the NUTS2 collaboration[3], the Supernova Integral Field Spectrogaph (SNIFS) on the University of Hawaii 2.2-meter telescope, and both the Magellan Inamori Kyocera Echelle (MIKE) and the Low Dispersion Survey Spectrograph (LDSS3) instruments on the Landon T. Clay (Magellan) Telescope at Las Campanas Observatory. A classification spectrum taken with the Robert Stobie Spectrograph (RSS) on the South African Large Telescope at -14.0 days was obtained from TNS and is also shown here (Jha et al., 2021).

Spectra taken with the ARC 3.5m were reduced using standard IRAF[4] methods including bias subtraction, flat fielding, cosmic ray removal using L.A. Cosmic[5] package (van Dokkum, 2001), and flux calibration from a spectrophotometric standard star taken at a similar airmass that same night. The SNIFS spectrum is traced, extracted, and calibrated with custom Python routines (Tucker et al., in prep) and atmospheric attenuation is corrected using the results of Buton et al. (2013). The spectrum taken with Magellan/MIKE was processed through a combination of IRAF echelle tasks and the "mtools"[6] package, specially developed by Jack Baldwin for the reduction of MIKE spectra. A flux standard obtained during the same night of the observations was used as flux calibrator. Flux calibration was also checked with a low resolution Magellan/LDSS3 spectrum of SN 2021fxy

[3] https://nuts.sn.ie/

[4] IRAF is distributed by the National Optical Astronomy Observatories, which are operated by the Association of Universities for Research in Astronomy, Inc., under cooperative agreement with the National Science Foundation (NSF).

[5] http://www.astro.yale.edu/dokkum/lacosmic/

[6] http://www.lco.cl/?epkb_post_type_1=iraf-mtools-package

Table 5.1. Log of spectroscopic observations

Date (UT)	MJD	Epoch[a]	Obs. Range (Å)	Telescope/Instrument
2021 Mar 18.1	59291.11	−14.0	3496-9372	SALT/RSS[b]
2021 Mar 25.1	59299.09	−6.0	3398-9674	NOT/ALFOSC
2021 Mar 29.8	59302.83	−2.3	1600-5600	*HST*/STIS
2021 Apr 01.6	59305.55	+0.4	1600-5600	*HST*/STIS
2021 Apr 02.4	59306.38	+1.3	3400-9840	APO/DIS
2021 Apr 02.4	59306.43	+1.3	6905-25701	IRTF/SpeX
2021 Apr 03.1	59307.05	+2.0	3397-9673	NOT/ALFOSC
2021 Apr 04.3	59308.30	+3.2	3400-9840	APO/DIS
2021 Apr 06.2	59310.21	+5.1	3400-9840	APO/DIS
2021 Apr 08.4	59312.43	+7.3	1600-5600	*HST*/STIS
2021 Apr 08.5	59312.49	+7.4	3787-9100	UH88/SNIFS
2021 Apr 12.1	59316.11	+11.0	3400-9683	NOT/ALFOSC
2021 Apr 13.3	59317.31	+12.2	3400-9864	APO/DIS
2021 Apr 17.1	59321.13	+16.0	3439-9412	Magellan (Clay)/MIKE
2021 Apr 17.2	59321.24	+16.1	3816-10632	Magellan (Clay)/LDSS3
2021 Apr 19.6	59323.56	+18.4	6909-25714	IRTF/SpeX
2021 Apr 20.0	59324.04	+18.9	3401-9639	NOT/ALFOSC
2021 Apr 20.1	59324.11	+19.0	3707-9290	Magellan (Clay)/LDSS3
2021 May 03.9	59337.93	+32.8	3398-9653	NOT/ALFOSC
2021 May 10.2	59344.24	+39.1	6868-25384	IRTF/SpeX
2021 May 16.9	59350.91	+45.8	3689-9687	NOT/ALFOSC

Note. — [a] Relative to B-band maximum of MJD$= 59305.12$. [b] Retrieved from TNS (Jha et al., 2021).

obtained during the same night as the MIKE observation.

5.2.3.2. HST Spectroscopy

UV spectroscopy of SN 2021fxy with the *Hubble Space Telescope* (HST) equipped with STIS using the mid-UV G230L and the near-UV/optical G430L gratings was triggered by the program "Red or Reddened Supernovae? Understanding the Ultraviolet Differences of Normal Standard Candles" (PI: Brown; ID: 16221). Observations were scheduled for 29/30 Mar, 01 Apr, 03 Apr, and 08 Apr. Some observations on 01 Apr and all 03 Apr were unusable because of a guide star acquisition failure. Reduced spectra were obtained from the Mikulski Archive for Space Telescopes (MAST[7]). The multiple spectra from both grisms were combined using a weighted average within a bin of 5 Å.

5.2.3.3. NIR Spectroscopy

The near-infrared (NIR) spectra of SN 2021fxy were obtained with the SpeX (Rayner et al., 2003) spectrograph installed on the 3.0-m NASA Infrared Telescope Facility (IRTF) on three epochs (2021-04-02, 2021-04-19 and 2021-05-10). The spectra were taken in both the PRISM and SXD mode with a slit size of 0.5×15". The spectra were taken using the classic ABBA technique, and were reduced utilizing the `Spextool` software package (Cushing et al., 2004). The telluric absorption corrections were done using the `XTELLCOR` software. The log of NIR spectroscopic observations is given in Table 5.1.

5.3. Analysis

5.3.1. Light Curve Analysis

The full multi-band light curves are shown in Figure 5.2, with the $uBVgri$ photometry presented in the CSP natural system. The full log of observations is presented in Section 5.6. Using SuperNovae in Object Oriented Python (SNooPy, Burns et al., 2014), we fit the light curves, with the fits shown in Figure 5.2. We find that SN 2021fxy reaches a B-band maximum of 13.57 ± 0.01 mag on $t_{max} = 59305.12 \pm 0.34$ days, corresponding to 14.39 days after discovery. The color-stretch s_{BV} is found to be 0.99 ± 0.03, which is consistent with a normal-bright SN Ia. The estimated distance modulus is estimated as $\mu = 32.86 \pm 0.08$, which is consistent with the estimate derived from the host redshift in Section 5.2. The host extinction is estimated as $E(B-V)_{host} = 0.018 \pm 0.06$ mag.

An examination of the early $B - V$ color evolution , as shown in Figure 5.3, reveals that SN 2021fxy follows the "red" evolutionary track, as defined by Stritzinger et al. (2018b). SN 2021fxy's classification as a "shallow-silicon" object within the Branch scheme (see Sect. 5.3.2) would make

[7] https://science.nasa.gov/astrophysics/astrophysics-data-centers/multimission-archive-at-stsci-mast

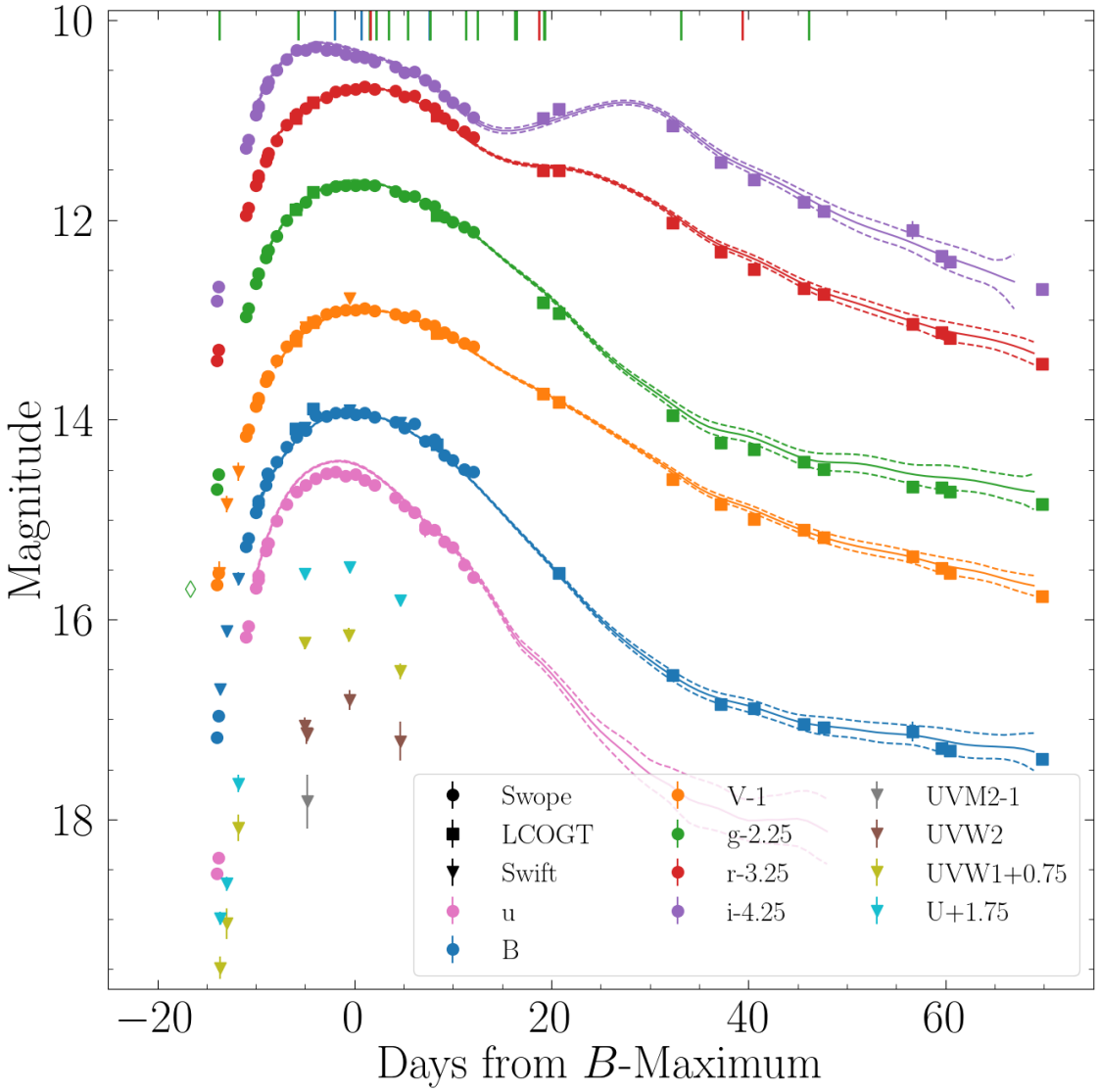

Figure 5.2: Multi-band light curves of SN 2021fxy. $uBVgri$ data from the Swope 1-m telescope are shown in circles, $BVgri$ data from Las Cumbres Observatory Global Telescope 1-m network in squares, and $UVW2$, $UVM2$, $UVW1$, U, and B data from *SWIFT/UVOT* in triangles. The last non-detection from ASASSN is noted with an open diamond. Epochs of UV (blue), optical (green), and NIR (red) spectra are marked along the top axis. SNooPy fits to the $uBVgri$ photometry are plotted (solid lines), with 1-σ errors (dashed lines).

it the first known spectroscopically normal SS object to follow the "red" track, as all the normal SS/91T-like objects in the Stritzinger et al. (2018b) sample follow the "blue" track.

The color evolution in the UV compared to other SNe Ia with *HST* UV spectroscopy is shown in Figure 5.4. Due to the low number of Swift observations, spectrophotometry is performed on the *HST*/STIS spectra. SN 2021fxy is found to be an NUV-red object in the Milne et al. (2013) scheme, and shows evolution similar to other NUV-red objects SNe 2013dy, ASASSN-14lp, and 2017erp.

5.3.2. Spectroscopic Analysis

5.3.2.1. Optical Spectra

The optical spectral sequence of SN 2021fxy is shown in Figure 5.5. The earliest optical spectrum at -14.0 days shows high velocity in both the Si II $\lambda6355$ and Ca II NIR triplet features at $-18,200$ and $-27,400$ km s^{-1} respectively, as measured from the minimum of the absorption troughs. At -6.0 days, the high velocity Si II has mostly faded, leaving only the photospheric component, while the high velocity Ca II remains prominent, particularly the NIR triplet, until roughly $+12$ days, before fully disappearing around $+19$ days. The Si II $\lambda6355$ line has a noticeably flat emission peak, indicating that the Si is detached from the photosphere (Jeffery & Branch, 1990). The spectra otherwise resemble that of a typical "Branch-normal" SNe Ia, as shown in Figure 5.6.

High-resolution spectra at +16.1 days from the MIKE spectrograph on the Landon T. Clay (Magellan) telescope reveal four distinct Na I D doublets along the line of sight to the supernova in the Milky Way. The pseudo-equivalent width of the galactic Na I D lines is 0.524 ± 0.002Å, which implies an extinction of $E(B-V)_{MW} = 0.058 \pm 0.039$ according to Eq. (9) of Poznanski et al. (2012), compared to the $E(B-V)_{MW} = 0.084$ derived from the Schlafly & Finkbeiner (2011) re-calibration of the Schlegel et al. (1998) dust maps, assuming an $R_V = 3.1$. No absorption from Na I D is seen at or near the redshift of NGC 5018, implying that there is negligible host reddening of SN 2021fxy (Phillips et al., 2013).

Velocity measurements of several key SN Ia features were made using the Measure Intricate Spectral Features In Transient Spectra (`MISFITS`) package[8] and are shown in Figure 5.8. Fitted spectra are first smoothed using the FFT low-pass filter method described in Marion et al. (2009). Next, a raw error spectrum is calculated from the difference between the unsmoothed and smoothed spectra, before it is then smoothed using a Gaussian kernel, resulting in a final error spectrum where the the 1σ error spectrum encompasses 68% of the absolute value of the raw error spectrum. Measurements of the feature minima are then made by fitting the minimum value of the smoothed spectrum over a user-defined range. A Markov Chain Monte Carlo (MCMC) method is used to generate a new instance of the smoothed spectrum and repeat this measurement 1000 times, with the overall error determined from the adding the measurement error (as defined by the 1σ spread from

[8] https://github.com/sholmbo/misfits

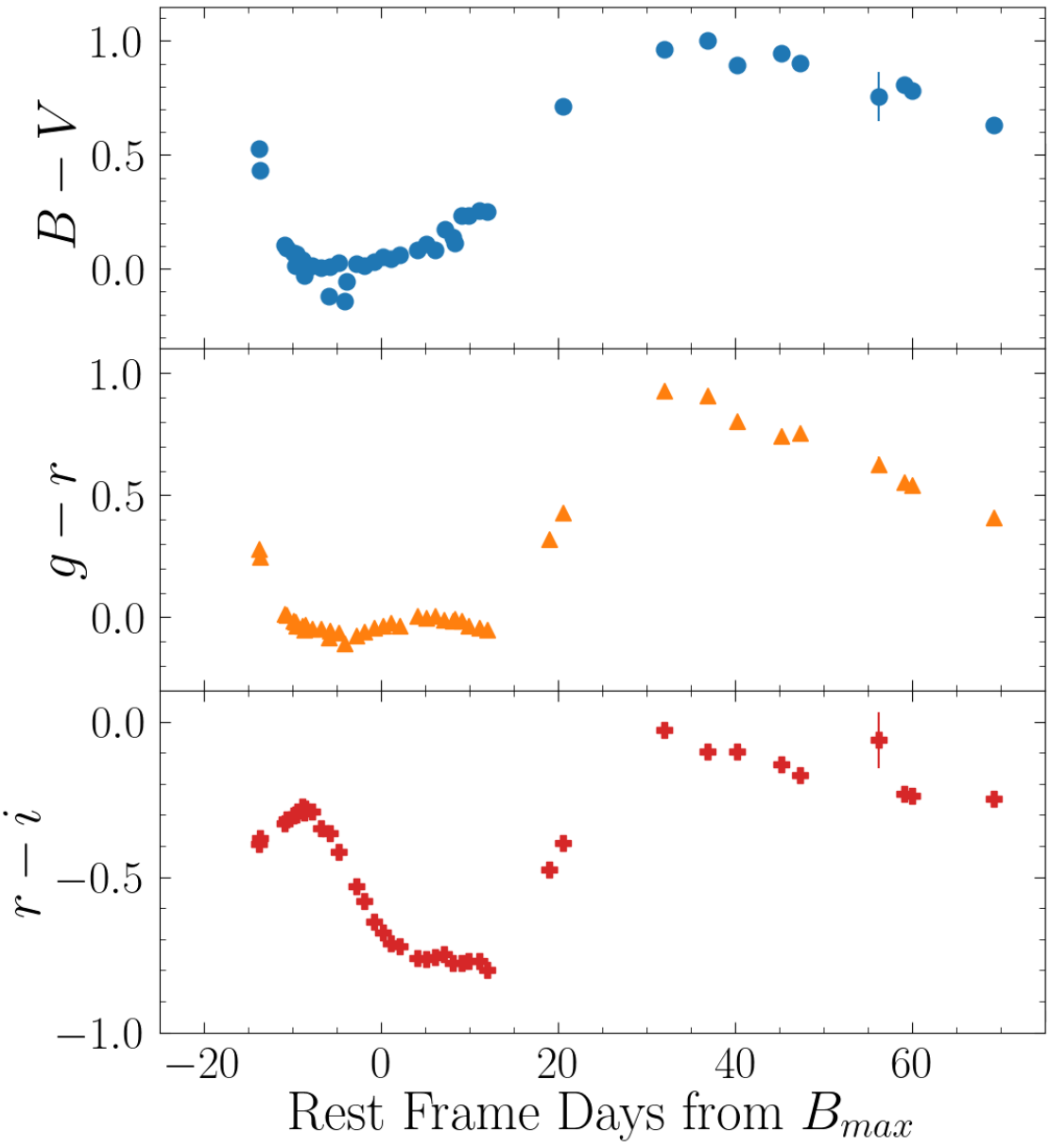

Figure 5.3: $B-V$, $g-r$, and $r-i$ color curves of SN 2021fxy, in the CSP natural system.

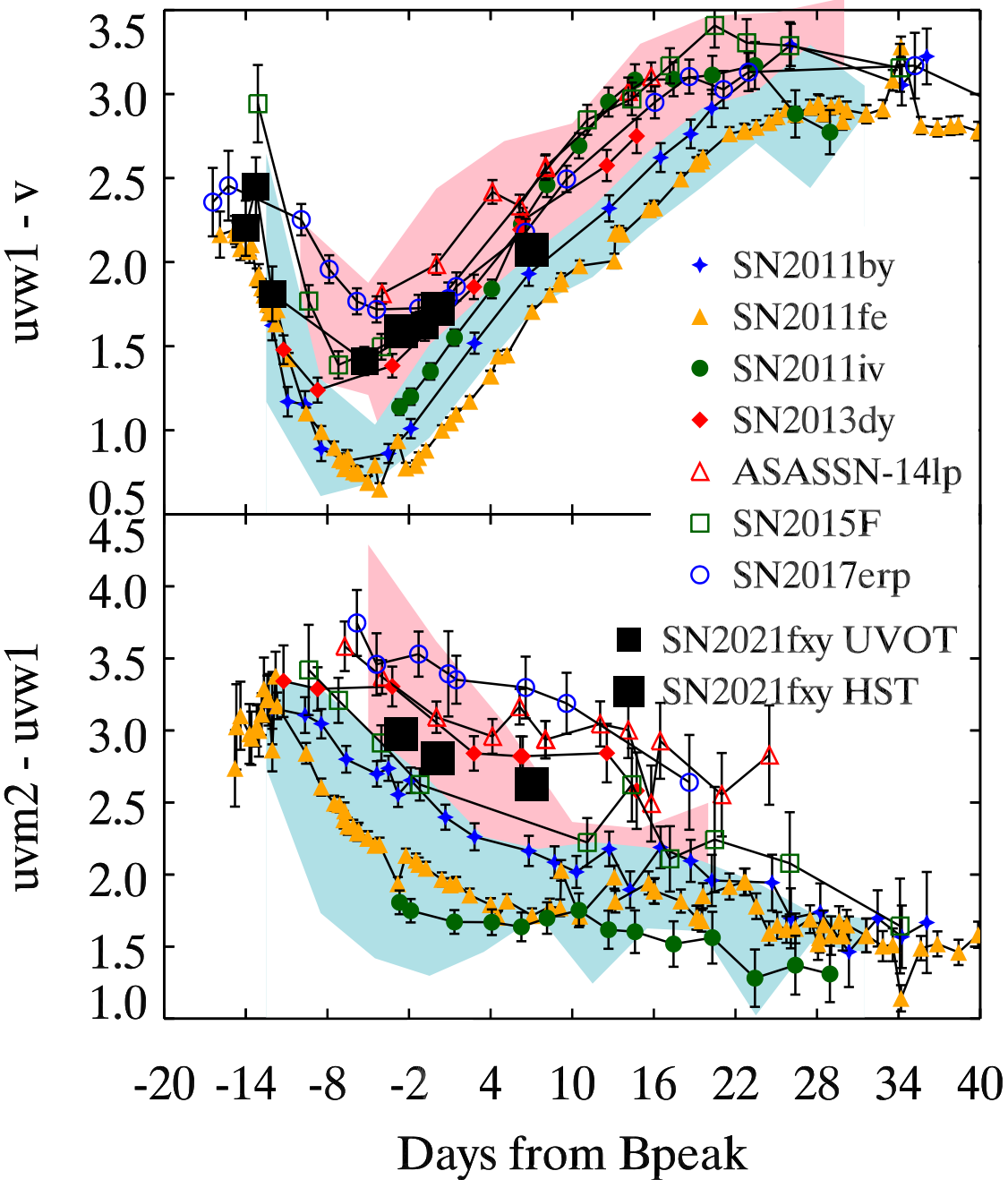

Figure 5.4: UV color evolution of SN 2021fxy compared to other spectroscopically normal SNe Ia with *HST* UV spectroscopy. The pale blue and red polygons define the locations of NUV-blue and NUV-red objects respectively, as defined in Milne et al. (2013). The larger black squares are derived from spectrophotometry derived from *HST*/STIS UV spectral observations.

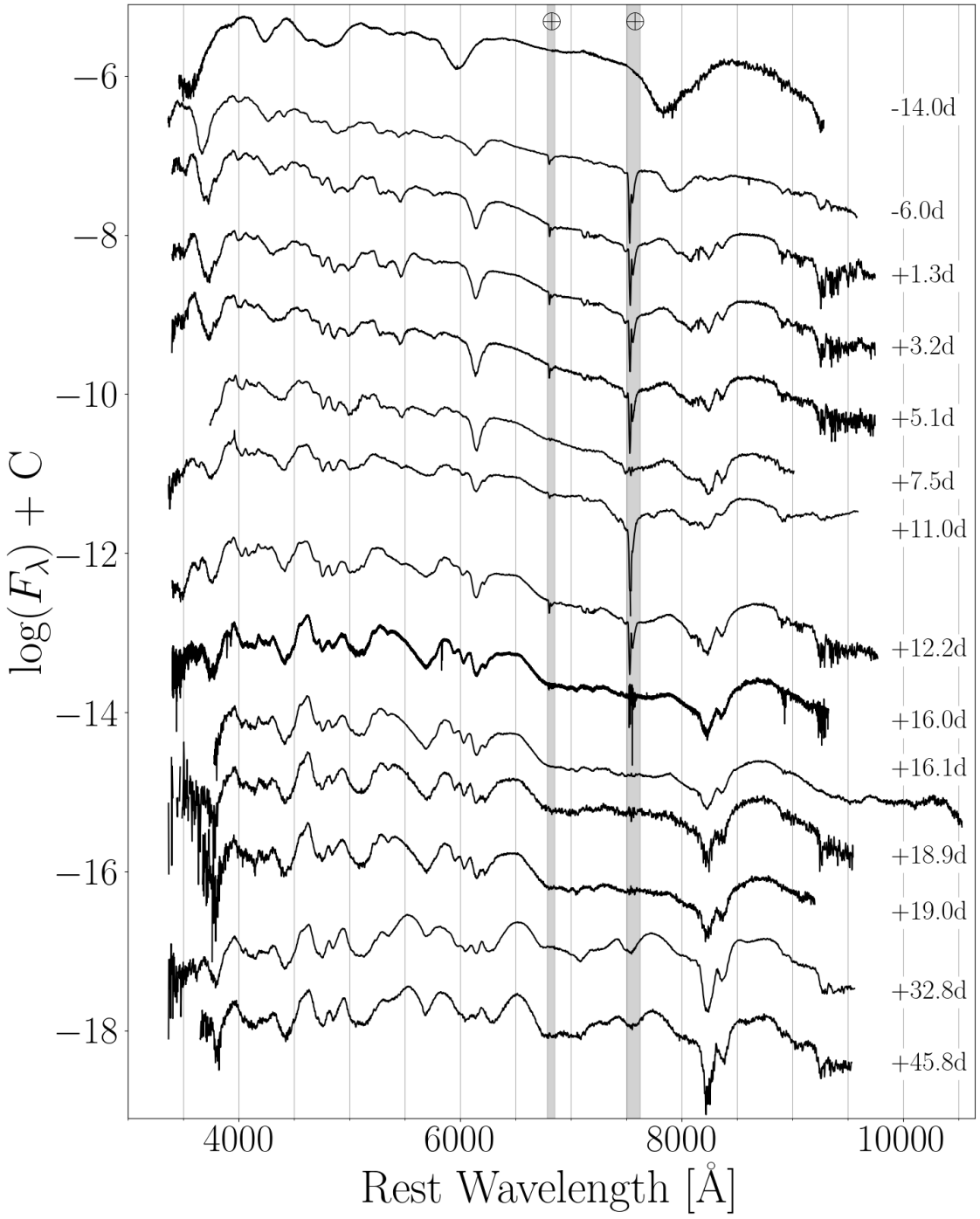

Figure 5.5: Optical spectra of SN 2021fxy corrected for Milky Way extinction. Epoch relative to B-band maximum are shown next to each spectrum. Gray boxes mark regions of strong telluric absorption.

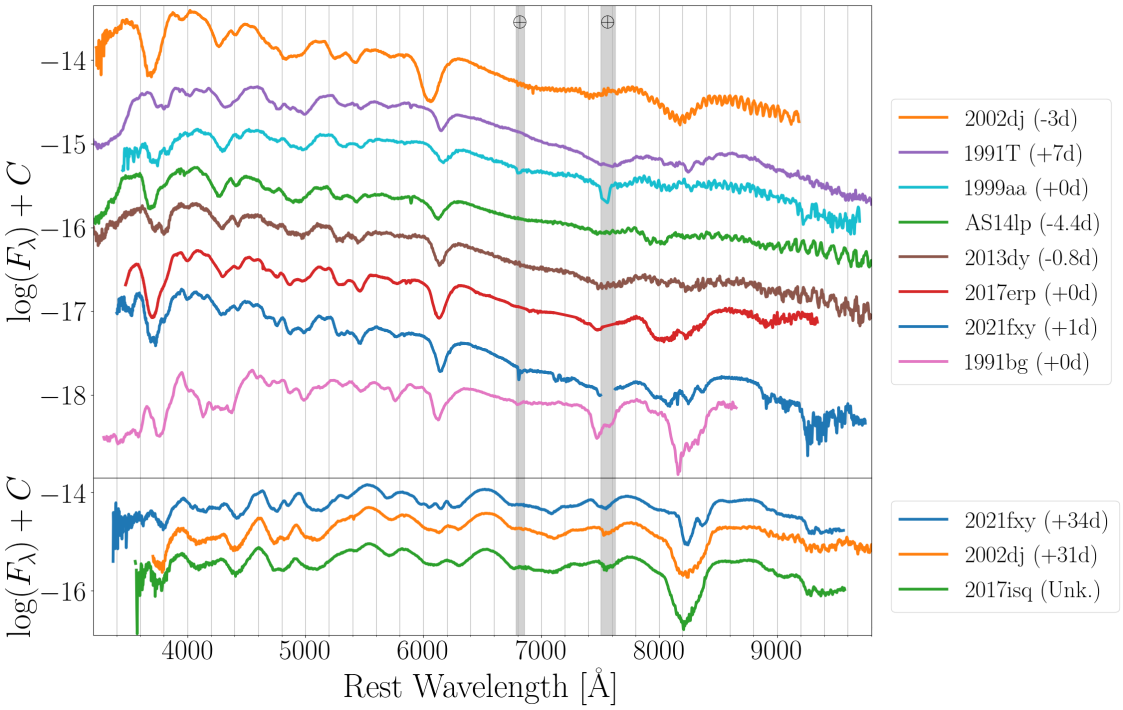

Figure 5.6: *Top Panel*: Comparison of SN 2021fxy near maximum light to its sibling SN 2002dj (BL), SNe 2013dy and 2017erp (CN), SNe 1991T, 1999aa, and ASASSN-14lp (SS), and SN 1991bg (CL). *Bottom Panel*: Comparison of sibling SNe 2002dj and 2021fxy to potential sibling SN 2017isq roughly one month after maximum light.

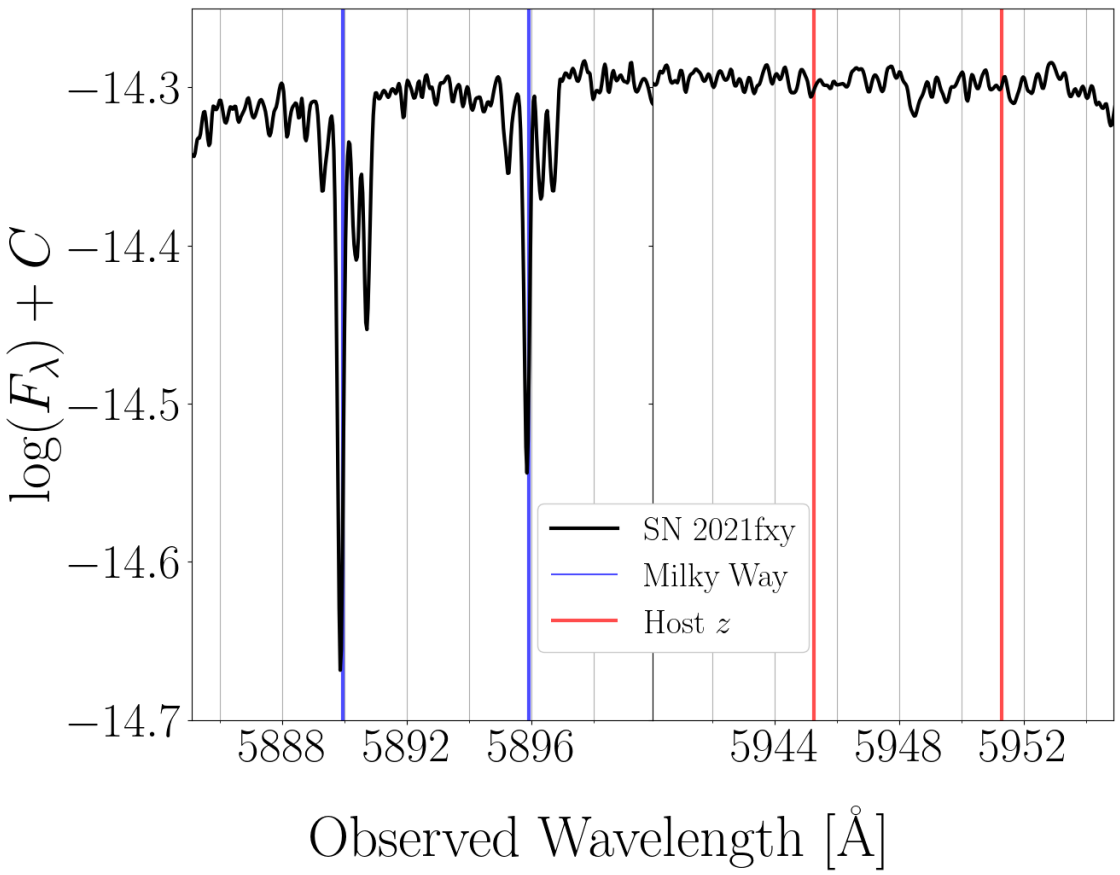

Figure 5.7: High-resolution spectrum of SN 2021fxy at +16.1 days focused on the Na I D doublet. Four distinct sets of doublets are seen corresponding to interstellar clouds within the Milky Way. No detectable Na I D lines are seen at or near the host redshift of $z = 0.009393$.

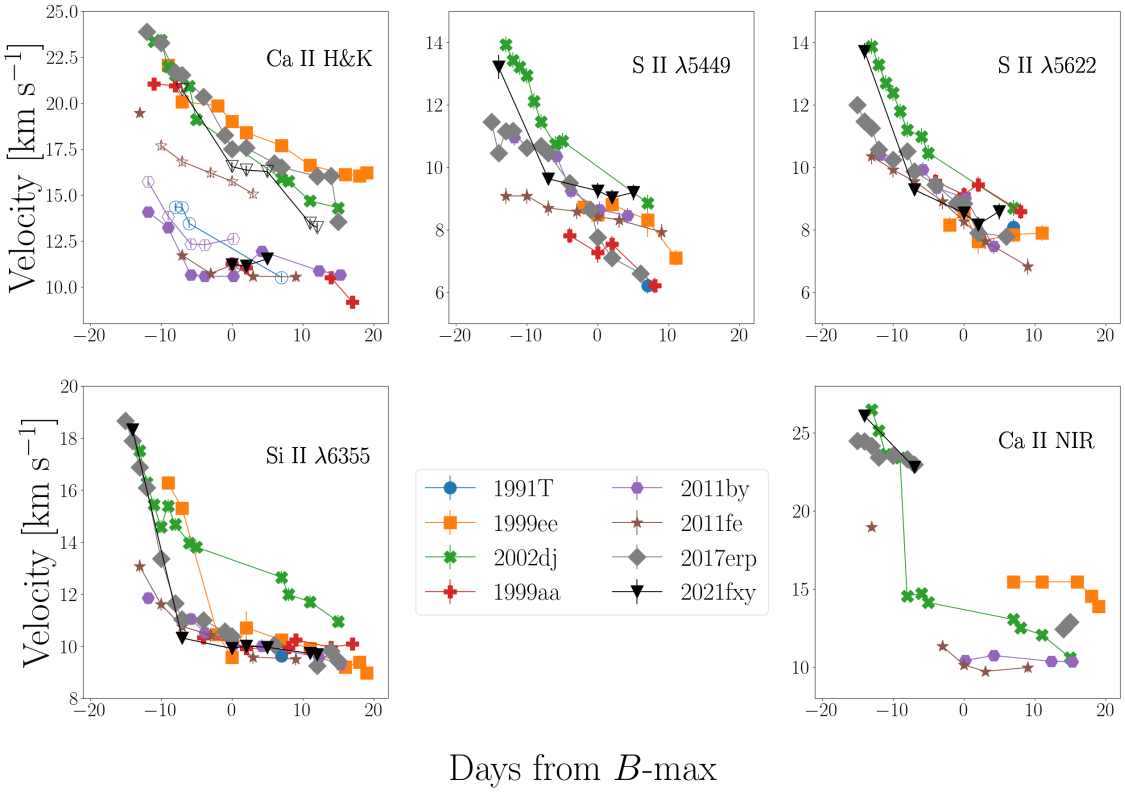

Figure 5.8: Velocities of important SNe Ia features during the photospheric phase as defined in Folatelli et al. (2013). Spectra for SN 2017erp were taken from Brown & Crumpler (2020), and all others were retrieved from the Open Supernova Catalog (Guillochon et al., 2017).

the MCMC sample) to the error derived from the instrumental resolution (assumed to be 6 Å when not provided) in quadrature. These measurements reveal that SN 2021fxy has similar velocities to other well-observed SNe Ia, including the 1991T-like object SN 1991T; SS objects like SNe 1999aa and 1999ee; and CN objects including SNe 2011by, 2011fe, and 2017erp. SN 2021fxy's sibling, SN 2002dj (an 2002bo-like or BL) is also shown for comparison.

Using the Spextractor[9] and SNIaDCA[10] packages of Burrow et al. (2020), we measure the pEW's of the Si II λ5972 and λ6355 features in the +1.3d spectra to classify SN 2021fxy within the Branch scheme. As shown in Figure 5.9, SN 2021fxy falls near the intersection of the 2σ confidence regions of the SS and CN groups, and has as a 64.1% chance of belonging to the SS subgroup, compared to a 35.7% chance of belonging to the CN subgroup. We note that some of the SNe Ia in the Burrow et al. (2020) sample located within a few Å of SN 2021fxy in the Branch diagram change their group membership from CN to SS when additional information like the Si II velocity at max light and maximum B-band magnitude are included in the Gaussian Mixture Model.

[9] https://github.com/anthonyburrow/spextractor
[10] https://github.com/anthonyburrow/SNIaDCA

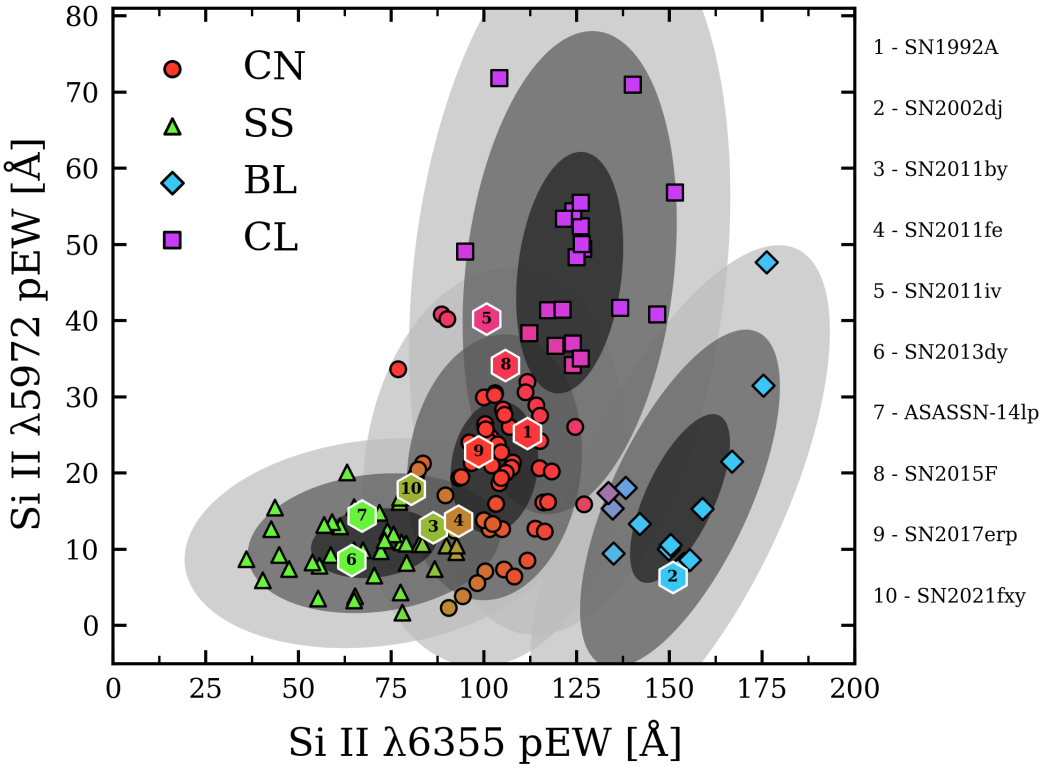

Figure 5.9: Branch Diagram from Burrow et al. (2020) with SNe 2021fxy, 2002dj, and other members of the UV sample of spectroscopically normal SNe Ia over-plotted. The coloring of each point corresponds to the likelihood of membership in a particular subgroup.

Interestingly, SNe Ia such as SNe 2011by and 2011fe, which are typically associated with the core-normals also fall along the border of the CN and SS subgroups. While differences in the spectral epoch, methodology of measuring the pEW's and locations of the boundaries between the different subgroups may vary from diagram to diagram, it is clear that a significant number of "normal" SNe Ia lie along the CN/SS border. While SN 1991T-like objects have been found to be an extreme subset of the SS group (M. Phillips, et al., in preparation), further study of the SNe Ia that reside along the CN/SS boundary of the Branch diagram may reveal information about the underlying physical differences between the two subgroups. Clearly, SNe 2011by, 2011fe, and 2021fxy are not SN 1991T-like objects, but rather belong to a group of objects that are near the middle of the SS/CN continuum.

5.3.2.2. UV Spectra

The UV spectral sequence obtained with *HST*/STIS is shown in Figure 5.10. The UV spectral features are relatively stable across the ∼10 day interval, with the most prominent evolution being

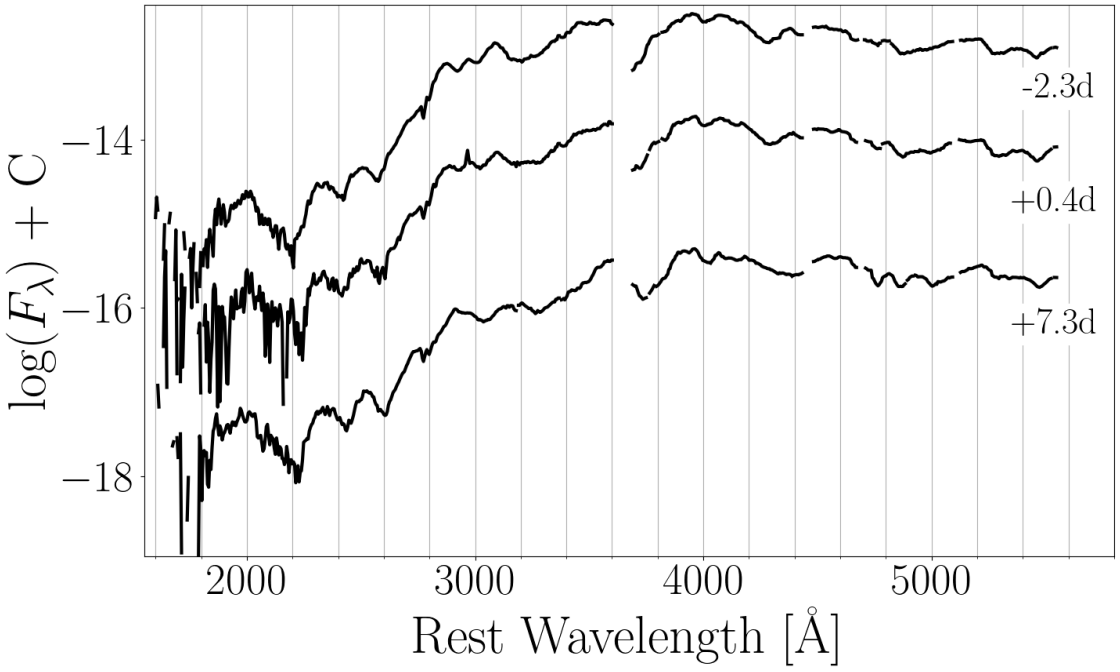

Figure 5.10: *HST*/STIS spectroscopy of SN 2021fxy corrected for Milky Way extinction.

the gradual weakening of the Cr II/Co II/Fe II blends near ∼2950 Å and ∼3200 Å.

Figure 5.11 shows the maximum light spectrum of SN 2021fxy plotted against the spectra of other spectroscopically normal SNe Ia closest to maximum light, including SNe 2011by (Foley & Kirshner, 2013; Graham et al., 2015), 2011fe (Pereira et al., 2013; Mazzali et al., 2014), 2011iv (Foley et al., 2012; Gall et al., 2018a), 2013dy (Pan et al., 2015), ASASSN-14lp (Shappee et al., 2016; Foley et al., 2016), 2015F (Foley et al., 2016; Burns et al., 2018), and 2017erp (Brown & Crumpler, 2020). From this sample, we see that four objects, SNe 2013dy, ASSASN-14lp, 2017erp, and 2021fxy show "suppressed" flux in the mid-UV relative to the other SNe Ia in the sample, which show less variation in their relative fluxes throughout the mid-UV. These four "suppressed" SNe also have mid-UV features which are blue-shifted relative to their un-suppressed counterparts. Both the "suppressed" and "un-suppressed" subsets show no common behaviors in either their near-UV spectral features or flux levels. However, the two subsets do show differences in their Ca II H&K features, with the "suppressed" SNe Ia possessing strong high velocity (HV) components that dominate the H&K feature. Un-suppressed SNe Ia show much weaker HV components and are dominated by the photospheric component. In the cases of the SNe Ia with HST spectra extending to the red half of the optical and NIR, those with MUV suppression (SN 2013dy and ASASSN-14lp) show higher flux levels than the un-suppressed SNe Ia, although it is unclear how much of these flux differences may be due to variations in host reddening. The source of this MUV suppression and its connection to feature locations and the Ca II H&K lines is explored further in Sect. 5.4.1.

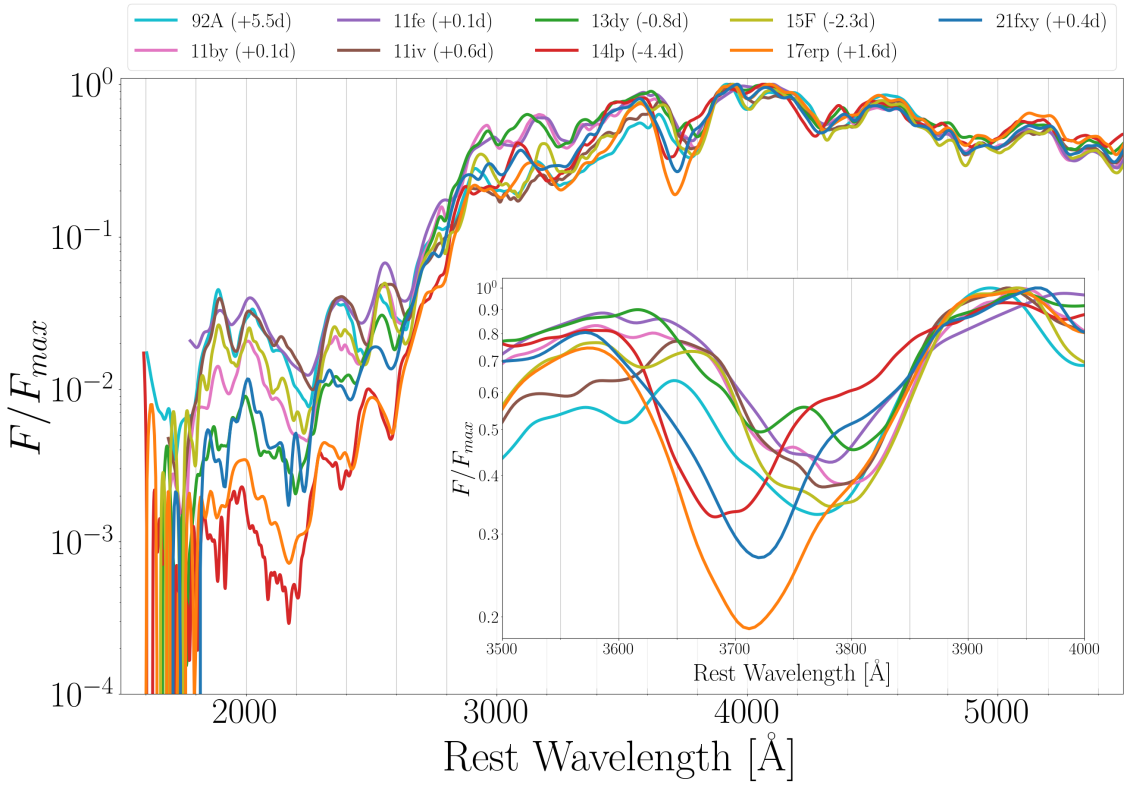

Figure 5.11: Comparison of SN 2021fxy with other spectroscopically normal SNe Ia having *HST*/STIS spectra, corrected for Milky Way extinction. Spectra are normalized relative to the maximum flux, which is located at either the Ca II H&K emission peak or the Si II blend emission peak at $\sim$ 4075 Å. Along with SNe 2013dy, ASASSN-14lp, and 2017erp, SN 2021fxy shows suppressed flux in the mid-UV and blue-shifted mid-UV features relative to SNe Ia without suppressed mid-UV fluxes. *Inset:* Close up of the Ca II H&K features, showing that SNe Ia with MUV flux suppression have strong HV Ca II H&K components which dominate the feature.

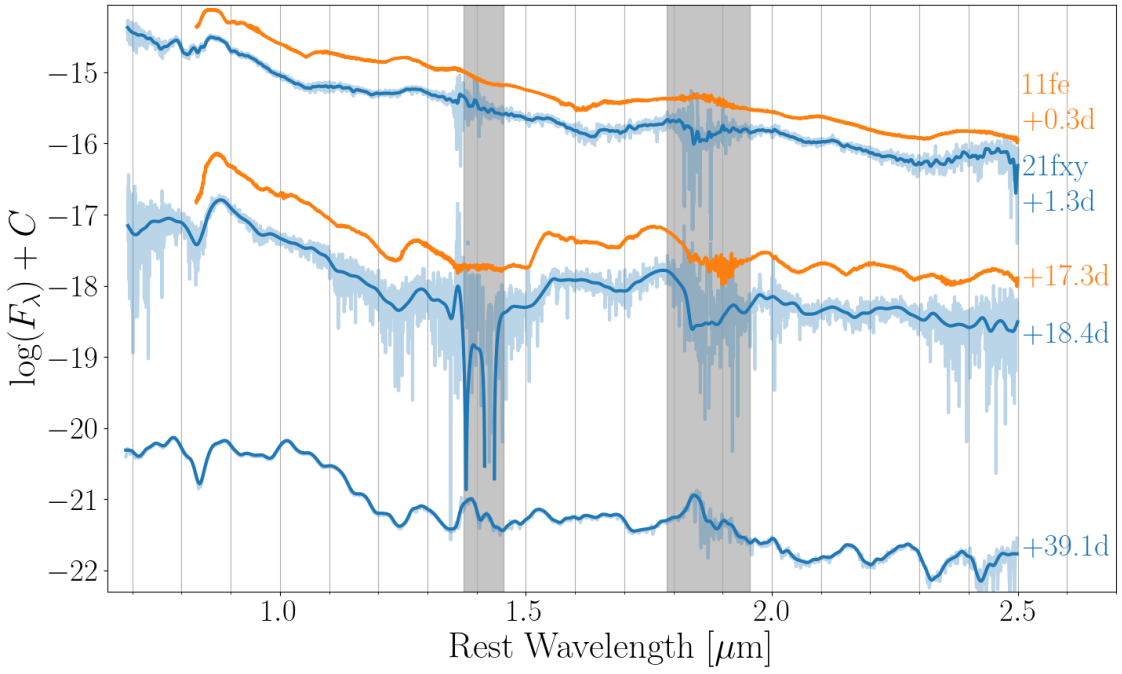

Figure 5.12: NIR spectra of SN 2021fxy. NIR spectra of SN 2011fe from Hsiao et al. (2013) at similar epochs are shown for comparison. Smoothed spectra are plotted in the foreground, with the raw spectra shown behind. The epoch relative to B-band maximum is printed next to each spectrum. Grey boxes mark regions of strong telluric absorption.

5.3.2.3. NIR Spectra

NIR spectra of SN 2021fxy are shown in Figure 5.12. Compared to spectra of SN 2011fe at similar epochs, the $+1.3$ day and $+18.4$ day spectra show broad similarities. Near maximum light, the Mg I and Mg II features between 0.9 μm and 1.1 μm appear significantly weaker in SN 2021fxy. A close examination of the C I $\lambda1.0693$ and Mg II $\lambda1.0927$ blend reveals that the feature is so weak that relative to the noise in the spectrum, we cannot conclusively identify the presence of either line. In the +18.4 day spectrum, high noise levels make identifications of many weak features difficult. The noise also complicates the measurement of the properties of the H-band break, v_{edge}. Using a similar procedure to Ashall et al. (2019a) we measure $v_{edge} = 12500 \pm 54$ km s^{-1}, which is consistent with other measurements of v_{edge} at that epoch in the Ashall sample, including SN 2011fe. We note that the reported error of v_{edge} is the statistical error of the Gaussian center; small variations in the definition of the continuum can alter v_{edge} by $\gtrsim 1000$ km s^{-1}. The IGE emission peaks appear also to be noticeably slower than those in 2011fe across all bands. By $+38$ days the spectra is dominated by IGE lines, similar to other NIR spectra at similar epochs in the sample of Marion et al. (2009).

5.4. Discussion

5.4.1. Mid-UV Suppression

One potential source of the mid-UV suppression is the reddening of the SN by dust in the host galaxy. However, estimating the amount of host extinction can be difficult, with different methods yielding significantly different results (for an example see SN 2017erp in Brown & Crumpler, 2020). Additionally, numerous studies have shown that dust properties vary across different galaxies, and their extinction laws have different forms than that of the Milky Way (see, for example Mathis, 1990; Phillips et al., 2013, and references therein). Therefore, we attempt to correct for the host extinction using the published values of $E(B-V)_{host}$ in combination with R_V values of ($R_V = 3.1$) and ($R_V = 2.1$), representing hosts with Milky Way like extinction and low-metallicity hosts like the SMC (Gordon et al., 2014; Yanchulova Merica-Jones et al., 2021). We also use the supernova light curve to attempt to fit the value of R_V in the host galaxy using SNooPy's "color_model", which simultaneously fits both $E(B-V)_{host}$ and R_V based on the intrinsic SN Ia colors determined by Burns et al. (2014). Since both parameters appear within the same fitting term they are covariant, and in cases where the total host extinction is small, the fit can become insensitive to the value of R_V. If this occurs, we impose a prior derived from a Gaussian Mixture Model and the data is refit using MCMC. The results of these fits are shown in Table 5.2. The host extinction corrected spectra are shown in Figure 5.13.

No matter which choice of R_V we use to correct for host extinction, the suppressed and non-suppressed subsets remain distinct. Corrections for host extinction do however, reduce the spread in relative flux between SNe within each group. After correcting for host extinction, SN 2013dy no longer shows MUV flux suppression, instead showing relative fluxes consistent with unsuppressed SNe Ia. However, SN 2013dy was one of multiple SNe (along with SNe 2011fe, 2011iv, and 2021fxy) with SNooPy fits that were initially insensitive to the value of R_V, but was the only one of this group where the MCMC fitting resulted in significant host extinction. All SNe which required MCMC fits show no evidence of significant host extinction from spectral observations. Therefore it is likely that the values derived by SNooPy represent over-estimates of the host extinction.

As noted in Sect. 5.3.2, those SNe Ia with MUV flux suppression also have feature minima in the mid-UV which are bluer relative to SNe Ia lacking MUV flux suppression. The relationship between the location of the flux minima for three mid-UV features (the Fe II/Co II blend between $2000-2400$ Å, the Fe II feature between $2350-2550$ Å, and the Fe II/Mg II blend between $2500-2700$ Å) and the relative flux at those minima are shown in Figure 5.14. The relationship is strongest in the Fe II/Co II blend, but is present in all three features. Similarly, the correlations are strongest when the spectra are corrected only for MW extinction, but the effect persists for all variations of host extinction corrections shown in Figure 5.13. This effect arises naturally, as

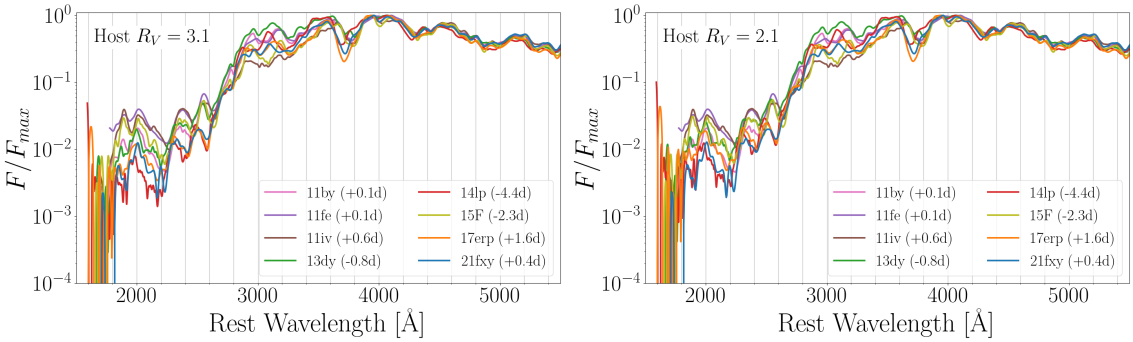

(a) $R_V = 3.1$ (b) $R_V = 2.1$

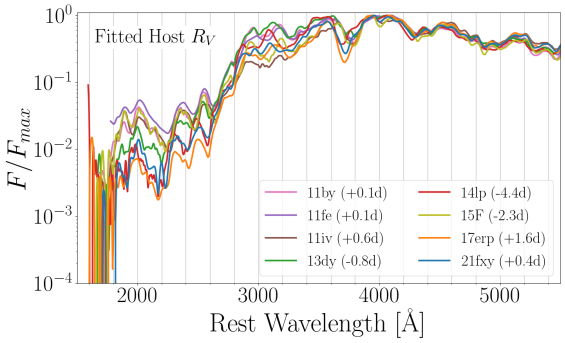

(c) Fitted R_V

Figure 5.13: Same as Figure 5.11, but with corrections for host extinction assuming $R_V = 3.1$ (top left), $R_V = 2.1$ (top right), and the fitted R_V (bottom) SN 1992A is omitted as there is insufficient photometry to generate a robust estimate of $E(B-V)_{host}$ or R_V.

Table 5.2. Host Extinction Fitting with SNooPy

Object	$E(B-V)_{host}$	R_V
2011by	0.191 ± 0.06	3.165 ± 0.52
2011fe*	0.08 ± 0.06	3.10 ± 0.16
2011iv*	-0.02 ± 0.06	3.11 ± 0.06
2013dy*	0.23 ± 0.06	3.10 ± 0.23
ASASSN-14lp	0.34 ± 0.06	2.27 ± 0.17
2015F	0.15 ± 0.06	4.09 ± 0.31
2017erp	0.18 ± 0.06	2.80 ± 0.51
2021fxy*	0.05 ± 0.06	3.11 ± 0.05

Note. — *Objects for which the initial fit was insensitive to R_V.

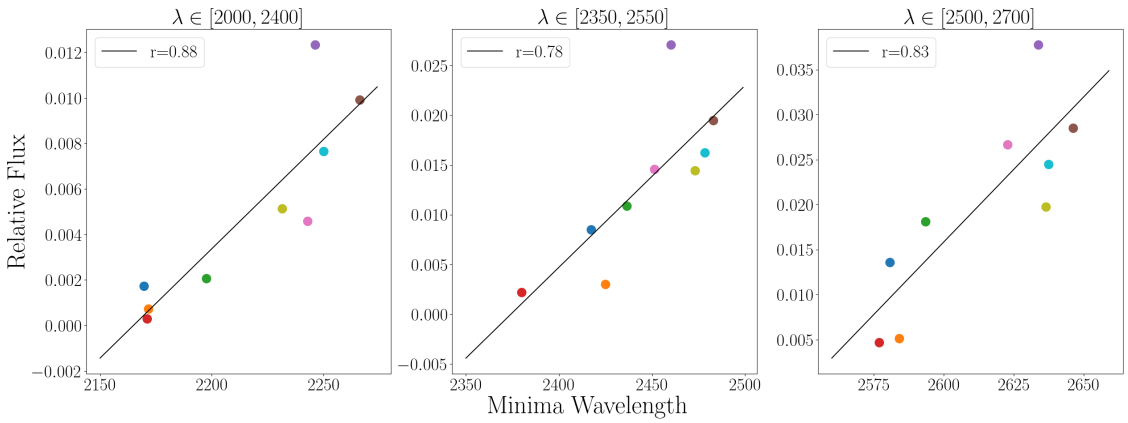

Figure 5.14: Relative flux versus minimum wavelength for three MUV features, with best fitting linear regression, corrected for Milky Way extinction, but not host extinction. Data points share the same coloring as Figure 5.11.

the opacity in the mid-UV originates primarily from the line blanketing of iron group elements (DerKacy et al., 2020), which increase the effective opacity in the mid-UV as their velocity increases (Wang et al., 2012). This same blue-shift in the mid-UV features was achieved by Barna et al. (2021) in their modeling of ASASSN-14lp by using a modified, shallower version of the W7 density profile. Because both shallower density profiles and higher line velocities produce broader lines, it is difficult to distinguish between the two effects as the primary source of the flux suppression from radiative transfer models alone.

Other effects may also play a role in producing MUV flux suppression, including changes in progenitor metallicity. As the amount of metals in the outer ejecta increases, so does the strength of the line blanketing; resulting in the photosphere being located at higher velocities, and thus suppressing flux in the mid-UV. However, large changes in metallicity cannot be responsible for this suppression, as they induce other changes in the broader UV spectrum that are not seen in the observed spectra (see Sect. 5.4.2 for more details). DerKacy et al. (2020) also found that their lower luminosity models produced these same mid-UV features blue-shifted relative to their higher luminosity models; primarily due to temperature variations in the outer portions of the ejecta altering the ionization balance between Fe II and Fe III significantly enough to change the relative composition of the line blends that comprise these mid-UV features.

5.4.2. Common Properties of MUV Suppressed SNe Ia

Examining our sample of SNe Ia with MUV suppression, there are a few commonalities shared across all four members that are easily apparent. The most obvious is the dominance of the HV component of the Ca II H&K lines over the photospheric components. We can quantify this dominance using the R_{HVF} measure established by Childress et al. (2014), originally defined for

Table 5.3. pEW Measurements

Object	HVF pEW [Å]	PVF pEW [Å]
1992A	26.96 ± 0.95	48.75 ± 0.62
2011by	26.43 ± 0.24	48.46 ± 0.25
2011fe	29.29 ± 0.01	48.81 ± 0.01
2011iv	23.88 ± 0.26	42.62 ± 0.24
2013dy	37.18 ± 0.26	37.39 ± 0.26
ASASSN-14lp	58.06 ± 0.14	62.83 ± 0.50
2015F	26.38 ± 0.32	42.33 ± 0.29
2017erp	66.95 ± 0.52	35.83 ± 0.51
2021fxy	68.78 ± 2.36	62.25 ± 1.36

the Ca II NIR triplet but now redefined here for the H&K lines as:

$$R_{HVF} = \frac{pEW(\text{HVF}_{\text{H\&K}})}{pEW(\text{PVF}_{\text{H\&K}})}. \tag{5.1}$$

We find that MUV suppressed SNe have values of $R_{HVF} \gtrsim 1.0$, while non-suppressed SNe have $R_{HVF} \lesssim 0.7$. R_{HVF} correlates with both the minimum wavelength and the relative flux at those minima for the three features specified in Subsection 5.4.1, although it correlates more strongly with the minimum wavelengths. As before, the correlations are strongest in the Fe II/Co II blend, but are present in the other two MUV features, and are still correlated after correcting for host extinction. These correlations are shown in Figure 5.15, with the pEW values shown in Table 5.3.

In Figure 5.11, we see that in the mid-UV, SNe 2013dy and 2021fxy have similar flux values and feature locations. The same is true of ASASSN-14lp and SN 2017erp. However, in the near-UV, SN 2013dy more closely resembles the spectra of SNe 2011fe and 2011iv. Meanwhile, ASASSN-14lp and SN 2021fxy have nearly identical spectra between 3000-3600 Å, with SN 2017erp showing lower NUV fluxes than any other member of the class. Returning to Figure 5.4, all four SNe are members of the NUV-red group, following the same general evolutionary track, albeit with significant scatter. ASASSN14-lp and SN 2017erp generally appear redder than SNe 2013dy and 2021fxy at all epochs.

The picture becomes even less clear when we begin to consider the optical properties of the MUV suppressed SNe. SNe 2013dy, ASASSN-14lp, and 2021fxy are all members of the SS class, while SN 2017erp belongs to the CN class. While the spectral behavior of SN 2013dy and ASASSN-14lp are typical of members of the SS subgroup, SNe 2017erp and 2021fxy share many characteristics, including nearly identical optical spectra and light curve parameters, ($s_{BV,21fxy} = 0.99 \pm 0.03$,

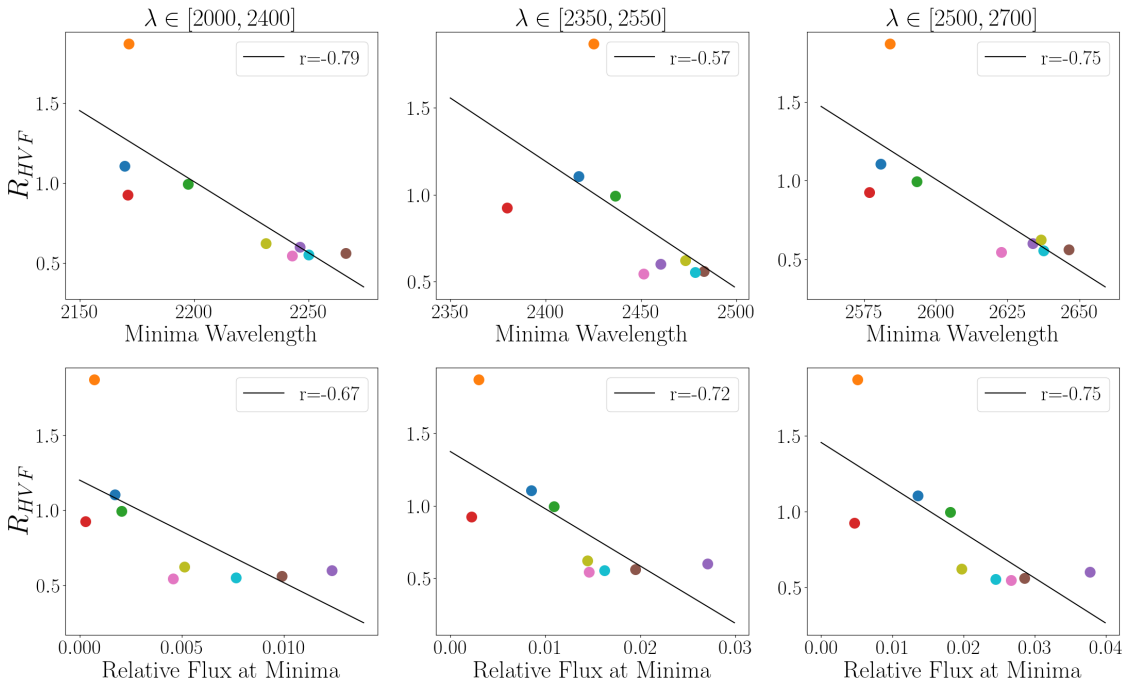

Figure 5.15: *Top Row*: R_{HVF} versus minimum wavelength for three MUV features, with best fit line as determined by linear regression. *Bottom Panel*: The same as the top panel, except for the relative flux at the minimum wavelength. All measurements were performed on spectra corrected for Milky Way extinction, but not host extinction. Data points share the same coloring as Figure 5.11.

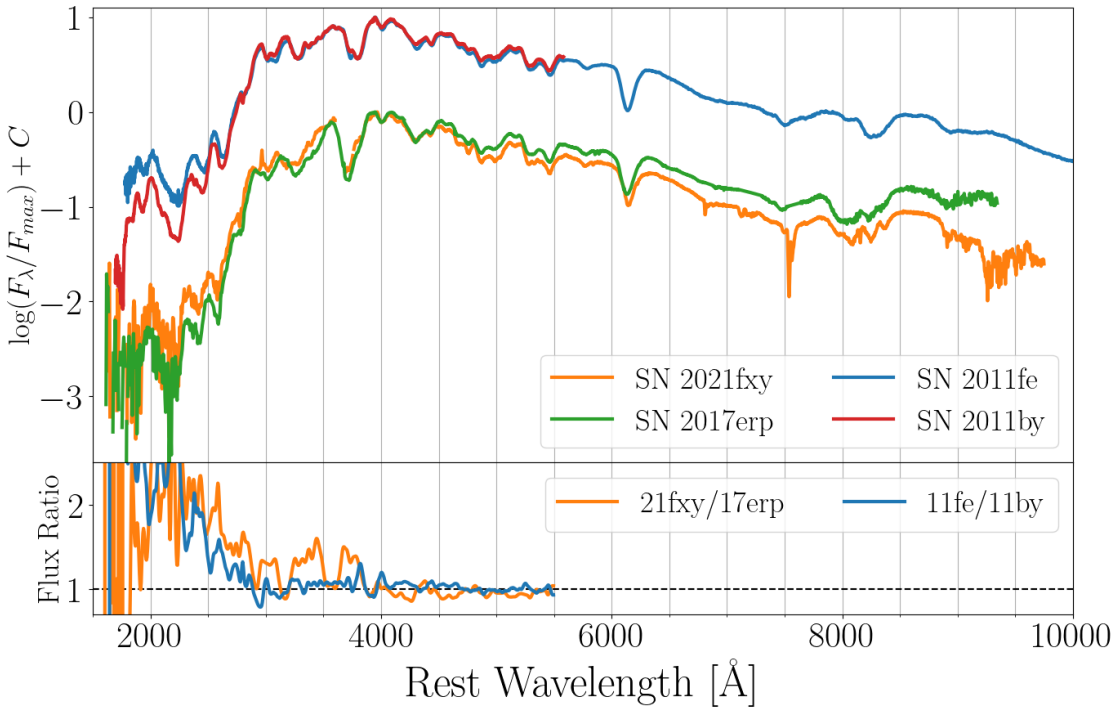

Figure 5.16: *Top Panel*: Combined UV/Optical spectra of SN 2021fxy and 2017erp at maximum light compared to those of SN 2011fe and 2011by. *Bottom Panel*: Flux ratio of SN 2021fxy/2017erp compared to that of SN 2011fe/2011by, as determined from the *HST* portions of the spectra.

$s_{BV,17erp} = 0.993 \pm 0.03$. When we expand this comparison to include spectra both before and after maximum light, we find that both object's spectra show similar feature velocities, line profiles, and line strengths for nearly all of their lines throughout their evolution. The notable exceptions to this being the Si II λ5972 and λ6355 lines. While it is tempting to establish a familial relationship between 2021fxy and 2017erp, given the numerous similarities is their spectral and photometric properties, unlike the "twin" supernovae 2011by and 2011fe, SNe 2017erp and 2021fxy are not members of the same Branch group (see again Figure 5.9, also Section 5.7). SNe 2021fxy and 2017erp also show significantly different continuum levels in the optical, as seen in Figure 5.16, which persists throughout the photospheric phase. Despite these differences, from the *HST* spectra, SN 2021fxy and SN 2017erp produce a flux ratio bluewards of $\sim$ 5600 Å that is comparable to the one between SN 2011fe and SN 2011by at maximum light, as seen in the lower panel of Figure 5.16. As such, we analyze the *HST* spectra of SNe 2017erp and 2021fxy to attempt to determine the source of their UV flux differences.

5.4.3. Comparing SNe 2017erp and 2021fxy

5.4.3.1. Optical Spectra Similarities

Early on, both supernovae show similar high-velocity (HV) Si II lines with the velocity of the feature in SN 2017erp declining from -21,600 km s^{-1} to -18,000 km s^{-1} from the first spectrum taken at -17.0 days to the one taken at -14.1 days. The first spectrum of SN 2021fxy at -14.0 days shows HV Si II at -18,200 km s^{-1}. Roughly a week later, the HV Si II has mostly faded from both supernovae. However, the -6.0d spectrum of SN 2021fxy shows a flat-topped emission peak associated with a feature detached from the underlying photosphere; compared to the traditional P-Cygni profile seen in the -8.5 day spectrum of SN 2017erp, where the feature begins forming at the photosphere (see Section 5.7 for further details). In SN 2021fxy, the Si II remains detached throughout the photospheric phase, until it begin to be polluted by Fe lines, which first appear around +11/+12 days, and are clearly present at +15.7 days. In contrast, the Si II feature in SN 2017erp does not detach from the photosphere until +6 days, and does not begin to show signs of the photosphere entering the Fe-rich inner region until +17 days. All together, these differences support the classification of SN 2021fxy as a SS object. Nugent et al. (1995) showed that the Branch sequence (neglecting BL) is driven by differences in temperature, with CL being coolest and SS being hottest. To zeroth order these temperature differences may be associated with the total amount of ^{56}Ni produced in the explosion. Thus, in a near Chandrasekhar mass progenitor scenario we expect SS to produce somewhat more ^{56}Ni and somewhat less silicon, leading to more rapid evolution in the Si II features for SS as compared with CN supernovae.

5.4.3.2. UV Flux Differences

Spectral formation in the ultraviolet is quite complicated. Several factors, such as metallicity, density structure, and luminosity are known to have strong impacts on the observed spectra. However, all of these factors are interrelated, making the identification of which variable (or combination of variables) is responsible for the observed differences between SNe Ia quite difficult. Host reddening also becomes significant in the UV, as small differences in the estimate of the host R_V can significantly alter the observed flux levels. Therefore, rather than attempt to disentangle these related effects, we examine the flux ratios from a self-consistent set of models, varying one factor at a time, to place limits on the relative differences in each of these variables by assuming the observed UV differences are caused solely by an individual factor.

Using the $t = 15$ day models of Lentz et al. (2000), we can explore differences in the relative progenitor metallicity as the source of the UV differences between the two supernovae. These models are NLTE simulations based on W7, with the abundances of all elements heavier than oxygen in the unburned C+O layer ($v \gtrsim 15000$ km s^{-1}) scaled by factors of ζ = 1/30, 1/10, 1/3, 3, and 10 relative to solar metallicity. As previously noted by Foley & Kirshner (2013), the flux

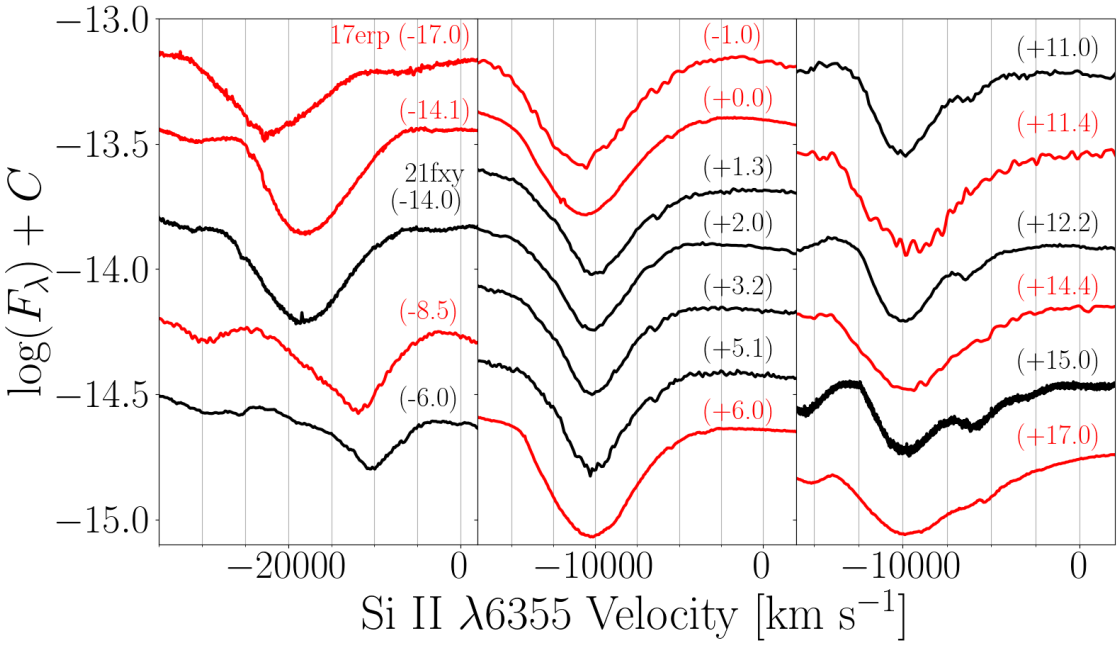

Figure 5.17: Comparison of Si II λ6355 line evolution in SN 2021fxy and SN 2017erp.

ratios from models with the same metallicity ratio produce the same general trend across the UV, and therefore are only able to infer relative metallicities between the two SNe, not differentiate the absolute metallicities of the supernovae. In exploring the impact of relative metallicity differences between SNe 2021fxy and 2017erp, we examine only the region between 2000-2500 Å, as spectral formation in this region is almost entirely determined by iron group elements (see Fig. 8 of DerKacy et al., 2020). No combination of any two Lentz models is able to reproduce the flux ratio of 21fxy/17erp across the entire wavelength range, in part due to the diminishing ability of these models to distinguish between increasingly large differences in the relative metallicity. The best match to the 21fxy/17erp flux ratio is produced by the $\zeta_{1/30}/\zeta_{10}$ curve ($\chi^2 = 166.87$, $\chi^2_\nu = 1.7$), If we instead fit over the entire *HST* spectra with $\lambda > 1800$ Å, we find that we can no longer distinguish between the flux ratios produced by curves produced by the $1/300$ ($\chi^2 = 328.19$), $1/100$ ($\chi^2 = 328.23$), and $1/90$ ($\chi^2 = 341.10$) metallicity ratios. This result matches what we see in the top panel of Figure 5.18, as each of these three curves are virtually indistinguishable redder than 2500 Å, and only distinguished by small variations in the height of a few peaks between $2000 - 2500$ Å where metallicity differences should be most apparent.

The bottom panel of Figure 5.18 shows selected flux ratios of models from DerKacy et al. (2020) compared to the flux ratio of 21fxy/17erp. Analysis of these models reveal that unlike the flux ratios generated from the models of Lentz et al. (2000), the flux ratios generated from the DerKacy et al. (2020) models are sensitive to both the relative luminosity difference and absolute luminosity of the model. This is due to the luminosity differences inducing temperature variations in the outer ejecta

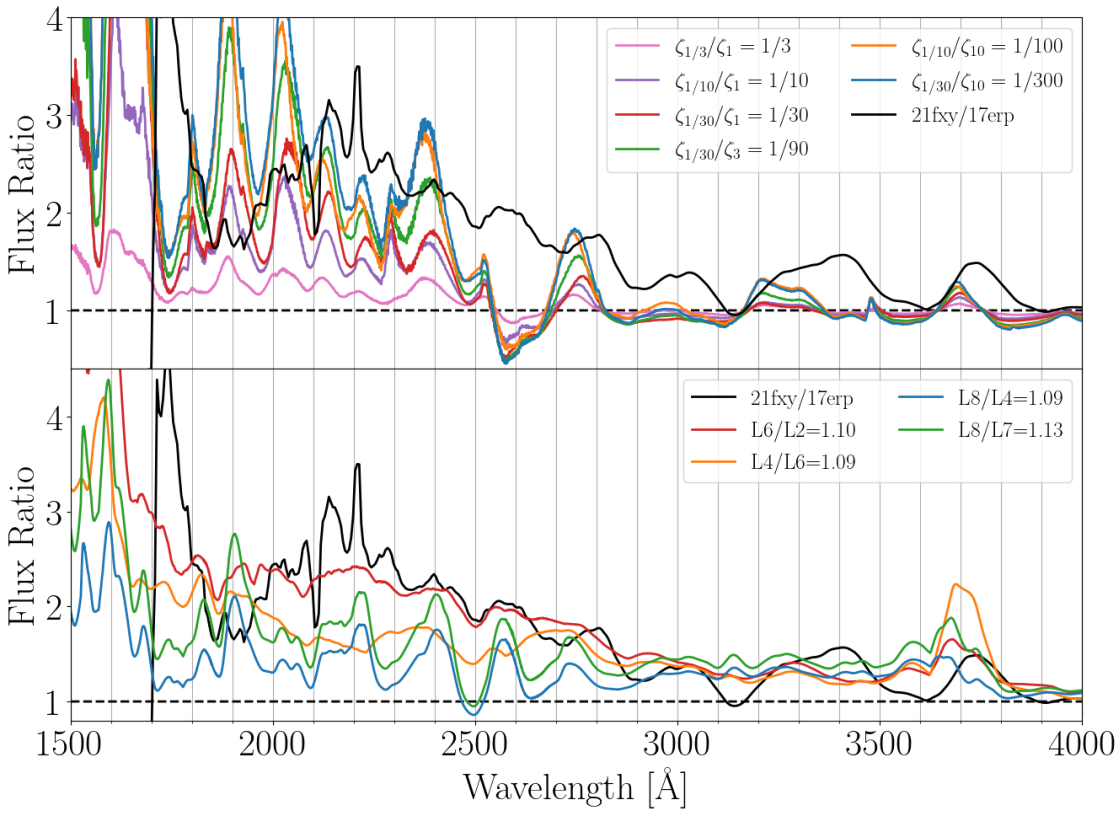

Figure 5.18: *Top Panel*: Flux ratios of the Day 15 spectral models from Lentz et al. (2000) with the flux ratio of SN 2021fxy to SN 2017erp over-plotted. *Bottom Panel*: Flux ratios for selected models of DerKacy et al. (2020) compared to the flux ratio of SN 2021fxy to SN 2017erp.

that alter the shape of the underlying continuum, as well as the excitation and ionization states of the outer ejecta. The differences produce different strengths and locations of spectral features in the ejecta, resulting in unique flux ratio curves dependent on the luminosities of the two spectra in the ratio. In effect this is an application of the Spectral-fitting Expanding Atmosphere Method (SEAM Mitchell et al., 2002; Baron et al., 2004; Dessart & Hillier, 2010) We find good agreement between the flux ratios produced from the L6/L2 models ($\chi^2 = 190.77$, $\chi^2_\nu = 0.25$) and the flux ratio of 21fxy/17erp, implying that SN 2021fxy has a peak bolometric luminosity 10% higher than that of SN 2017erp.

However, we caution against too strong an interpretation of these results as the model and input luminosities used in DerKacy et al. (2020) were only simulated at one epoch and were chosen because they best reproduce SN 2011fe, which is known to have the bluest UV minus optical colors among SNe Ia with UV spectra (Brown et al., 2017; P. Brown, et al., in preparation). Furthermore, both the best fitting luminosity and metallicity ratio curves only broadly capture the observed differences between SNe 2021fxy and 2017erp in the mid-UV, where the differences in both properties are expected to be the greatest. It is only when the differences in flux from the remainder of the UV and optical are examined (see again Figure 5.16), we find that the behavior is more consistent with those expected from differences in luminosity than metallicity (Lentz et al., 2000; DerKacy et al., 2020). Additional work to verify the relationship between UV spectra and SNe Ia properties like metallicity and luminosity across more models and epochs is currently underway.

5.4.4. Sibling's Analysis

Detailed analyses of SNe Ia siblings (e.g. two or more SNe Ia hosted in the same galaxy) allow us to test many of our assumptions about SNe Ia as cosmological distance indicators. By virtue of sharing the same host, many of the factors that increase the scatter in cosmological distance measurements are eliminated, including dependencies on properties of the host galaxy such as host mass and metallicity, and peculiar velocities (Sullivan et al., 2010; Burns et al., 2020; Brown, 2014).

The one confirmed sibling to SN 2021fxy, SN 2002dj, was studied in depth by Pignata et al. (2008), and determined to be a Ia-BL within the Branch scheme with several similarities to SN 2002bo. Using SNooPy, we fit the photometry of SN 2002dj, with the results compared to those of SN 2021fxy in Table 5.4. From the results, we find that the implied distance modulus to NGC 5018 agree to 1.2σ, within the average $\Delta\mu$ of other sibling SNe Ia studied by Burns et al. (2020). Both values are also consistent with the redshift derived value to less than 1σ. The inferred host extinctions are consistent at the 1.3σ level. The different estimates of $E(B-V)$ are likely due to different local environments in the vicinity of the two SNe. SN 2002dj was found to be coincident with an extended emission region appearing as a warped disk covering portions of NGC 5018, and is associated with regions of star formation (Pignata et al., 2008; Goudfrooij et al., 1994). SN 2021fxy

Table 5.4. Comparison of Light Curve Parameters

Parameter	SN 2021fxy	SN 2002dj
t_{max} (MJD)	59305.12 ± 0.34	52450.92 ± 0.35
s_{BV}	0.991 ± 0.04	0.936 ± 0.04
$E(B-V)_{host}$ (mag)	0.017 ± 0.06	0.096 ± 0.06
μ (mag)	32.865 ± 0.09	32.969 ± 0.09

exploded in a part of NGC 5018 unassociated with this emission region.

5.5. Conclusions

We present detailed photometric and spectroscopic followup of of SN 2021fxy, a SN Ia discovered in NGC 5018 for which we also obtained *HST*/STIS UV spectroscopy. The ground-based spectra and photometry were mostly obtained as part of the Precision Observations of Infant Supernova Explosions (POISE, Burns et al. 2021) collaboration. Our observations reveal that SN 2021fxy is a normal-bright SN Ia belonging to the SS group within the Branch scheme. UV spectra show that when compared to other spectroscopically normal SNe Ia, SN 2021fxy is a member of a group of objects with flux suppression in the mid-UV, which cannot be explained by host reddening alone. Objects with MUV flux suppression all belong to the NUV-red group of SNe Ia, possess MUV features that are bluer than their non-suppressed counterparts and HV components in their Ca II H&K lines that are dominant over the photospheric components, as measured by the quantity R_{HVF}. One potential cause of this suppression are an increased effective opacity in the mid-UV from IGE at higher velocities, which would imply a continuous distribution of MUV flux values in SNe Ia. However, the presence of the HV Ca features could indicate that shells of material within the ejecta are responsible for the additional line blanketing. In either case, more UV spectral observations of SNe Ia are needed to determine the physical mechanism responsible for the MUV flux suppression.

Among those SNe Ia with MUV flux suppression, SNe 2021fxy and 2017erp show remarkable similarities despite belonging to the SS and CN Branch subgroups respectively, which allow us to probe the mechanisms responsible for variations between different MUV suppressed objects. We find that the flux differences between SNe 2021fxy and 2017erp in the UV are comparable in size to those between SNe 2011by and 2011fe, but are instead likely due to variations in the intrinsic luminosity differences between the two SNe; not metallicity differences as has been suggested for SNe 2011by and 2011fe. Further modeling to better understand the impact of different physical mechanisms which contribute to UV spectral formation, and which observational quantities best measure this diversity are ongoing.

5.6. Photometric Data

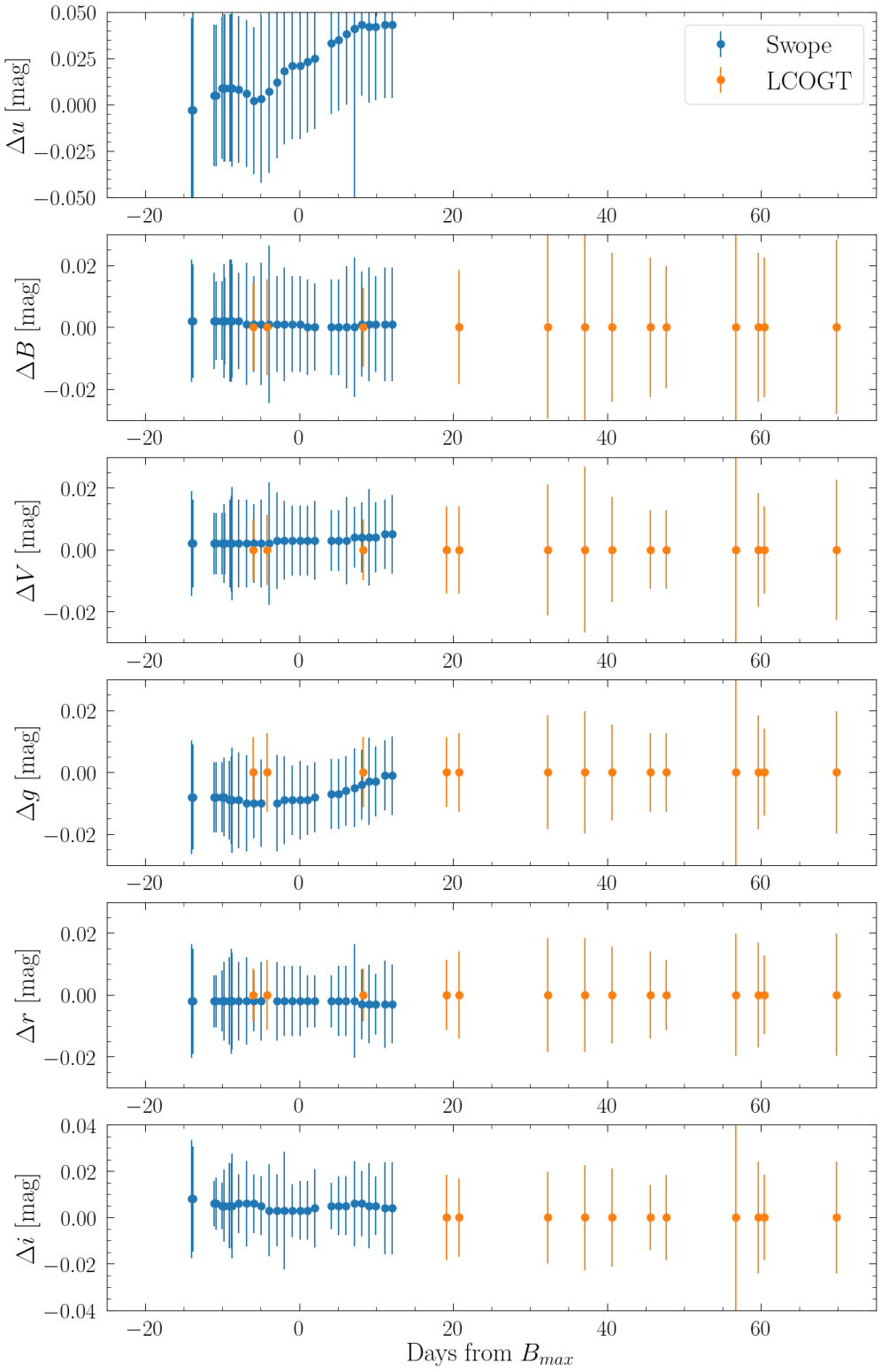

Figure 5.19: S-corrections in $uBVgri$ bands from both the Swope 1-m and Las Cumbres Global 1-m Telescope network.

Table 5.5. Log of *Swift* Photometry for SN 2021fxy

MJD	UVM2 [mag]	UVW1 [mag]	UVW2 [mag]	U [mag]	B [mag]	V [mag]
59291.39	···	···	···	···	···	16.53(0.12)
59291.45	···	18.74(0.11)	···	17.24(0.007)	16.70(0.06)	···
59292.13	···	···	···	···	···	15.85(0.08)
59292.18	···	18.74(0.11)	···	16.89(0.07)	···	···
59292.19	···	···	···	···	16.12(0.06)	···
59293.37	···	17.33(0.13)	···	15.89(0.09)	15.59(0.07)	15.52(0.10)
59300.12	···	15.48(0.06)	17.07(0.09)	13.80(0.04)	14.08(0.04)	14.07(0.06)
59300.24	···	···	17.14(0.11)	···	···	···
59300.32	···	···	17.15(0.07)	···	···	···
59300.35	18.82(0.27)	···	···	···	···	···
59304.59	···	15.40(0.07)	16.81(0.10)	13.73(0.04)	13.91(0.04)	13.78(0.05)
59309.77	···	15.77(0.08)	···	14.06(0.05)	···	···
59309.78	···	···	17.22(0.20)	···	14.03(0.04)	···

Table 5.6. Log of Swope 1-m photometry for SN 2021fxy

MJD	u [mag]	B [mag]	V [mag]	g [mag]	r [mag]	i [mag]
59291.12	18.54(0.04)	17.18(0.01)	16.65(0.01)	16.93(0.01)	16.66(0.01)	17.06(0.02)
59291.32	18.38(0.04)	16.97(0.01)	16.54(0.01)	16.79(0.01)	16.55(0.01)	16.93(0.02)
59294.10	16.18(0.03)	15.27(0.01)	15.16(0.01)	15.21(0.01)	15.20(0.01)	15.53(0.01)
59294.31	16.07(0.03)	15.19(0.01)	15.10(0.01)	15.13(0.01)	15.13(0.01)	15.45(0.01)
59295.11	15.69(0.03)	14.93(0.01)	14.87(0.01)	14.88(0.01)	14.90(0.01)	15.21(0.01)
59295.34	15.61(0.03)	14.81(0.01)	14.80(0.01)	14.78(0.01)	14.80(0.01)	15.11(0.01)
59295.40	15.57(0.03)	14.85(0.01)	14.78(0.01)	14.79(0.01)	14.83(0.01)	15.13(0.01)
59296.09	15.32(0.03)	14.66(0.01)	14.62(0.01)	14.62(0.01)	14.66(0.01)	14.94(0.01)
59296.27	15.25(0.03)	14.54(0.01)	14.57(0.01)	14.55(0.01)	14.61(0.01)	14.91(0.01)
59296.39	15.25(0.03)	14.56(0.01)	14.57(0.01)	14.54(0.01)	14.58(0.01)	14.87(0.02)
59297.25	15.02(0.03)	14.42(0.01)	14.41(0.01)	14.40(0.01)	14.45(0.01)	14.75(0.01)
59298.25	14.85(0.03)	14.27(0.01)	14.27(0.01)	14.24(0.01)	14.30(0.01)	14.65(0.01)
59299.25	14.72(0.03)	14.17(0.01)	14.16(0.01)	14.13(0.01)	14.19(0.01)	14.56(0.01)
59300.20	14.65(0.03)	14.11(0.01)	14.08(0.01)	14.06(0.01)	14.13(0.01)	14.56(0.01)
59301.19	14.59(0.03)	13.96(0.02)	14.01(0.01)	...	...	14.52(0.01)
59302.24	14.55(0.03)	13.96(0.01)	13.94(0.01)	13.94(0.01)	14.02(0.01)	14.56(0.01)
59303.19	14.54(0.03)	13.93(0.01)	13.92(0.01)	13.90(0.01)	13.97(0.01)	14.55(0.02)
59304.23	14.58(0.03)	13.93(0.01)	13.90(0.01)	13.90(0.01)	13.95(0.01)	14.60(0.01)
59305.25	14.57(0.03)	13.95(0.01)	13.90(0.01)	13.89(0.01)	13.94(0.01)	14.62(0.01)
59306.16	14.63(0.03)	13.93(0.01)	13.89(0.01)	13.88(0.01)	13.91(0.01)	14.63(0.01)
59307.14	14.68(0.03)	13.97(0.01)	13.91(0.01)	13.90(0.01)	13.94(0.01)	14.67(0.01)
59309.26	14.81(0.03)	14.03(0.01)	13.95(0.01)	13.96(0.01)	13.96(0.01)	14.72(0.01)
59310.21	14.89(0.03)	14.08(0.01)	13.98(0.01)	14.00(0.01)	14.01(0.01)	14.78(0.01)
59311.23	14.96(0.03)	14.04(0.01)	13.96(0.01)	14.01(0.01)	14.01(0.01)	14.77(0.01)
59312.30	15.10(0.05)	14.21(0.02)	14.04(0.01)	14.09(0.01)	14.10(0.01)	14.85(0.01)
59312.30	15.14(0.08)	14.21(0.02)	14.04(0.01)	14.09(0.01)	14.10(0.01)	14.85(0.01)
59313.23	15.14(0.03)	14.20(0.01)	14.06(0.01)	14.11(0.01)	14.12(0.01)	14.91(0.01)
59314.23	15.26(0.03)	14.36(0.01)	14.13(0.01)	14.21(0.01)	14.23(0.01)	15.01(0.01)
59315.06	15.32(0.03)	14.41(0.01)	14.18(0.01)	14.26(0.01)	14.30(0.01)	15.08(0.01)

Table 5.6 (cont'd)

MJD	u [mag]	B [mag]	V [mag]	g [mag]	r [mag]	i [mag]
59316.29	15.50(0.03)	14.49(0.01)	14.24(0.01)	14.32(0.01)	14.36(0.01)	15.13(0.01)
59317.23	15.62(0.03)	14.52(0.01)	14.28(0.01)	14.37(0.01)	14.42(0.01)	15.22(0.01)

Table 5.7. Log of Los Cumbres Global Telescope 1-m network photometry for SN 2021fxy

MJD	B [mag]	V [mag]	g [mag]	r [mag]	i [mag]
59299.11	14.09(0.01)	14.21(0.01)	14.15(0.01)	14.23(0.01)	···
59300.93	13.89(0.01)	14.03(0.01)	13.97(0.01)	14.08(0.01)	···
59313.46	14.24(0.01)	14.13(0.01)	14.20(0.01)	14.21(0.01)	···
59324.29	···	14.74(0.01)	15.07(0.01)	14.76(0.01)	15.23(0.01)
59325.85	15.53(0.01)	14.82(0.01)	15.18(0.01)	14.75(0.01)	15.14(0.01)
59337.42	16.55(0.02)	15.59(0.01)	16.21(0.01)	15.28(0.01)	15.31(0.01)
59342.27	16.84(0.03)	15.84(0.02)	16.48(0.01)	15.57(0.01)	15.67(0.02)
59345.72	16.89(0.02)	16.00(0.01)	16.55(0.01)	15.75(0.01)	15.84(0.01)
59350.71	17.05(0.02)	16.10(0.01)	16.67(0.01)	15.93(0.01)	16.07(0.01)
59352.79	17.08(0.01)	16.18(0.01)	16.75(0.01)	15.99(0.01)	16.16(0.01)
59361.82	17.12(0.10)	16.37(0.05)	16.92(0.03)	16.29(0.01)	16.35(0.09)
59364.74	17.29(0.02)	16.48(0.01)	16.93(0.01)	16.38(0.01)	16.61(0.02)
59365.58	17.31(0.02)	16.53(0.01)	16.97(0.01)	16.43(0.01)	16.67(0.01)
59374.89	17.39(0.02)	16.76(0.02)	17.10(0.01)	16.69(0.01)	16.94(0.02)

Table 5.8. Log of S-corrected photometry for SN 2021fxy

MJD	u [mag]	B [mag]	V [mag]	g [mag]	r [mag]	i [mag]	Telescope
59291.12	18.54(0.04)	17.18(0.01)	16.65(0.01)	16.94(0.01)	16.66(0.01)	17.06(0.02)	Swope
59291.32	18.38(0.04)	16.97(0.01)	16.54(0.01)	16.79(0.01)	16.55(0.01)	16.92(0.02)	Swope
59294.10	16.17(0.03)	15.27(0.01)	15.16(0.01)	15.22(0.01)	15.20(0.01)	15.53(0.01)	Swope
59294.31	16.06(0.03)	15.19(0.01)	15.10(0.01)	15.14(0.01)	15.13(0.01)	15.44(0.01)	Swope
59295.11	15.68(0.03)	14.93(0.01)	14.86(0.01)	14.88(0.01)	14.90(0.01)	15.20(0.01)	Swope
59295.34	15.60(0.03)	14.81(0.01)	14.80(0.01)	14.79(0.01)	14.81(0.01)	15.10(0.01)	Swope
59295.40	15.56(0.03)	14.85(0.01)	14.78(0.01)	14.79(0.01)	14.83(0.01)	15.13(0.01)	Swope
59296.09	15.31(0.03)	14.66(0.01)	14.62(0.01)	14.63(0.01)	14.66(0.01)	14.93(0.01)	Swope
59296.27	15.24(0.03)	14.54(0.01)	14.57(0.01)	14.56(0.01)	14.61(0.01)	14.91(0.01)	Swope
59296.39	15.24(0.03)	14.56(0.01)	14.57(0.01)	14.55(0.01)	14.58(0.01)	14.86(0.02)	Swope
59297.25	15.01(0.03)	14.42(0.01)	14.41(0.01)	14.41(0.01)	14.46(0.01)	14.75(0.01)	Swope
59298.25	14.85(0.03)	14.27(0.01)	14.27(0.01)	14.25(0.01)	14.30(0.01)	14.64(0.01)	Swope
59299.11	···	14.09(0.01)	14.21(0.01)	14.15(0.01)	14.23(0.01)	···	LCOGT
59299.25	14.72(0.03)	14.17(0.01)	14.16(0.01)	14.14(0.01)	14.19(0.01)	14.55(0.01)	Swope
59300.20	14.65(0.03)	14.10(0.01)	14.08(0.01)	14.07(0.01)	14.13(0.01)	14.55(0.01)	Swope
59300.93	···	13.89(0.01)	14.03(0.01)	13.97(0.01)	14.08(0.01)	···	LCOGT
59301.19	14.59(0.03)	13.96(0.02)	14.01(0.01)	···	···	14.52(0.01)	Swope
59302.24	14.54(0.03)	13.96(0.01)	13.94(0.01)	13.95(0.01)	14.03(0.01)	14.55(0.01)	Swope
59303.19	14.52(0.03)	13.93(0.01)	13.92(0.01)	13.91(0.01)	13.97(0.01)	14.55(0.02)	Swope
59304.23	14.56(0.03)	13.93(0.01)	13.90(0.01)	13.90(0.01)	13.95(0.01)	14.59(0.01)	Swope

Table 5.8 (cont'd)

MJD	u [mag]	B [mag]	V [mag]	g [mag]	r [mag]	i [mag]	Telescope
59305.25	14.55(0.03)	13.95(0.01)	13.90(0.01)	13.90(0.01)	13.94(0.01)	14.62(0.01)	Swope
59306.16	14.61(0.03)	13.93(0.01)	13.88(0.01)	13.89(0.01)	13.91(0.01)	14.63(0.01)	Swope
59307.14	14.66(0.03)	13.97(0.01)	13.91(0.01)	13.91(0.01)	13.94(0.01)	14.67(0.01)	Swope
59309.26	14.78(0.03)	14.03(0.01)	13.94(0.01)	13.96(0.01)	13.96(0.01)	14.72(0.01)	Swope
59310.21	14.86(0.03)	14.08(0.01)	13.98(0.01)	14.01(0.01)	14.01(0.01)	14.78(0.01)	Swope
59311.23	14.92(0.03)	14.04(0.01)	13.96(0.01)	14.02(0.01)	14.01(0.01)	14.77(0.01)	Swope
59312.30	15.06(0.05)	14.21(0.02)	14.04(0.01)	14.09(0.01)	14.10(0.01)	14.85(0.01)	Swope
59313.23	15.10(0.03)	14.20(0.01)	14.06(0.01)	14.12(0.01)	14.13(0.01)	14.90(0.01)	Swope
59313.46	···	14.24(0.01)	14.13(0.01)	14.20(0.01)	14.21(0.01)	···	LCOGT
59314.23	15.22(0.03)	14.36(0.01)	14.12(0.01)	14.22(0.01)	14.23(0.01)	15.01(0.01)	Swope
59315.06	15.27(0.03)	14.41(0.01)	14.17(0.01)	14.27(0.01)	14.30(0.01)	15.07(0.01)	Swope
59316.29	15.45(0.03)	14.49(0.01)	14.24(0.01)	14.32(0.01)	14.36(0.01)	15.13(0.01)	Swope
59317.23	15.58(0.03)	14.52(0.01)	14.27(0.01)	14.37(0.01)	14.42(0.01)	15.22(0.01)	Swope
59324.29	···	···	14.74(0.01)	15.07(0.01)	14.76(0.01)	15.23(0.01)	LCOGT
59325.85	···	15.53(0.01)	14.82(0.01)	15.18(0.01)	14.75(0.01)	15.14(0.01)	LCOGT
59337.42	···	16.55(0.02)	15.59(0.01)	16.21(0.01)	15.28(0.01)	15.31(0.01)	LCOGT
59342.27	···	16.84(0.03)	15.84(0.02)	16.48(0.01)	15.57(0.01)	15.67(0.02)	LCOGT
59345.72	···	16.89(0.02)	16.00(0.01)	16.55(0.01)	15.75(0.01)	15.84(0.01)	LCOGT
59350.71	···	17.05(0.02)	16.10(0.01)	16.67(0.01)	15.93(0.01)	16.07(0.01)	LCOGT
59352.79	···	17.08(0.01)	16.18(0.01)	16.75(0.01)	15.99(0.01)	16.16(0.01)	LCOGT

Table 5.8 (cont'd)

MJD	u [mag]	B [mag]	V [mag]	g [mag]	r [mag]	i [mag]	Telescope
59361.82	···	17.12(0.10)	16.37(0.05)	16.92(0.03)	16.29(0.01)	16.35(0.09)	LCOGT
59364.74	···	17.29(0.02)	16.48(0.01)	16.93(0.01)	16.38(0.01)	16.61(0.02)	LCOGT
59365.58	···	17.31(0.02)	16.53(0.01)	16.97(0.01)	16.43(0.01)	16.67(0.01)	LCOGT
59374.89	···	17.39(0.02)	16.76(0.02)	17.10(0.01)	16.69(0.01)	16.94(0.02)	LCOGT

5.7. SYNOW Fits of SN 2021fxy

SYNOW is a highly parameterized code designed to simulate supernova spectra, to assist in the identification of spectral lines and estimation of the both photospheric velocity and velocity interval of ions within the supernova ejecta. It makes simple assumptions about the supernova, including spherical symmetry, homologous expansion, line formation via resonance scattering in the Sobolev approximation, and a sharp photosphere emitting a blackbody continuum to calculate a synthetic spectra. Key user defined parameters include the temperature of the blackbody continuum, photospheric velocity, and the reference line optical depth, e-folding velocity, velocity extent, and the Boltzmann excitation temperature for each ion included in the fit. The best fitting spectra is then determined via "chi-by-eye", as is the community standard. More information on SYNOW can be found in Jeffery & Branch (1990) and Branch et al. (2005, 2006).

As stated above, SNe 2021fxy and 2017erp show numerous similarities. Both have suppressed flux in the mid-UV and show features that are nearly identical in velocity, line profile, and line depth. However, SN 2021fxy evolves through its photospheric phase faster than 2017erp, as measured by the Si II $\lambda6355$ line, and the two SNe are members of different Branch groups. Using SYNOW, we can investigate just how similar the ejecta of the two SNe are.

Our generalized fitting procedure is as follows. After assuming a blackbody temperature T_{bb}, we fit the Si II features, assuming that the photospheric velocity (v_{phot}) is the same as the v_{min} of Si II. With the photospheric velocity (PV) established, we fit ions of other intermediate mass elements (IMEs), including Ca II, S II, Mg II, etc., including any high velocity (HV) components. Once initial fits of the IMEs are complete, we add the important ions arising from the iron group elements (IGEs), including Fe II, Fe III, Co II, and Ni II, revising our IME parameters as necessary to fit blended features. We assume an excitation temperature of ($T_{exec} = 10000$ K) unless stated otherwise. The full set of input parameters are listed in Tables 5.9 and 5.10. We briefly summarize our important findings below.

As previously shown in Figure 5.17, several epochs of SN 2021fxy show broad, flat topped emission profiles characteristic of line formation occurring in a region detached from the photosphere (Jeffery & Branch, 1990). However, because of our assumption that $v_{phot} = v_{min,Si}$, we only find one epoch of SN 2021fxy where Si II is clearly detached. Most likely, the Si II in the preceding epochs is detached by $\lesssim 1000$ km s^{-1}, as this represents the 3σ error in our velocity measurements. This is supported by the appearance of a weak C II $\lambda6580$ line at $+5.1$ days in SN 2021fxy, which serves to further flatten the emission peak. We find further support for this idea by examining the Si III lines, which is also detached from the photosphere at $+5.1$ days. As none of the Si lines in the SN 2017erp fits are detached, our SYNOW fits support our finding that SN 2021fxy evolves through its photospheric phase faster than SN 2017erp.

The Ca II lines proved particularly difficult to fit well. In addition to many of the NIR triplet features showing flat-topped emission peaks similar to the Si II lines, both the H&K lines and the NIR triplets often required multiple detached or HV components to accurately represent the feature. We were able to distinguish the different HV components through their different v_{max} values. These narrow regions may be indications of a series of shells in the outer layers of the SNe ejecta. Yet, the numerous components often resulted in fits that were not able to reproduce both features accurately. In SN 2021fxy, we were able to obtain good fits to both the Ca II features in all epochs except $+1.3$d and $+11.0$d, where the NIR triplet is preferentially fit. For SN 2017erp, the NIR triplet is preferentially fit in the -17.0d and -14.0d spectra due to incomplete coverage of the H&K features, and is preferentially fit in the -8.5d and -1.0d spectra.

S II lines are present from the earliest epochs in both SNe. The features grow stronger in both SNe, peaking in strength near maximum light before weakening significantly by $\sim +11$ days. The strength of S II is correlated with the photospheric temperature, however the response is both non-monotonic and strongly influenced by NLTE effects (Nugent et al., 1995). Therefore, although the excitation temperatures of the S II lines increase in both SNe, also peaking near maximum light it is difficult to discern whether this accurately captures the physics. C II lines are also present in the early epochs of both SNe. We find agreement with Brown & Crumpler (2020) that the C II lines are present at early times in SN 2017erp, but disappear in our fits after ~ -10 days. We similarly find evidence for a weak C II line in the -14.0 day spectra of SN 2021fxy, which disappears before our next spectrum at -6.0 days. Both SNe show features at the expected location of the O I $\lambda 7773$ line, yet the contamination of this feature by telluric lines and a strong contribution of Mg II $\lambda\lambda 7896, 7877$ doublet (likely overemphasized by our SYNOW fit) in SN 2021fxy makes fitting difficult. As a result, we can only definitively identify O I in the $+5.1$ day spectrum. In order to fit the blue Mg II features in SNe 2021fxy and 2017erp, our fits require that the Mg II be located at high velocities and/or have high excitation temperatures, resulting in the high excitation lines at $\lambda\lambda 7896, 7877$ appearing abnormally strong at the location of the O I lines. Examination of the NIR spectra of SN 2021fxy reveals Mg II lines that are weaker than those found in other NIR spectra of other SNe Ia, likely caused by the MUV suppression preventing the UV photons from exciting the upper states of Mg II.

At early times, the influence of IGEs on the spectra is restricted to HV and PV components of Fe II and Fe III. In SN 2017erp, Fe III is photospheric at all epochs except -17.0 days, while Fe II is consistently found as a high velocity feature. In SN 2021fxy however, the HV Fe III persists until at least the -6.0 day spectrum, while a weak photospheric component of Fe II begins appearing as early as -6.0 days. At later epochs, the influence of Ni II and Co II on the spectra become stronger, as the photosphere recedes into the Fe-rich inner regions of the ejecta.

Table 5.9. SN 2017erp SYNOW Parameters

Ion	Parameter	-17.0 d	-14.1 d	-8.5 d	-1.0 d	-0.0 d	+6.0 d	+11.4 d
	T_{bb} [K]	10500	10500	9500	11000	11000	10000	9800
	v_{phot} [10^3 km s^{-1}]	15.0	13.9	12.5	11.0	11.0	9.8	8.5
	v_{max} [10^3 km s^{-1}]	45.0	45.0	35.0	30.0	25.0	25.0	25.0
C II	τ	···	0.14	···	···	···	···	···
	v_{min}/v_{max}	···	13.9/25.0	···	···	···	···	···
	v_e	···	2.0	···	···	···	···	···
	T_{exec}	···	20000	···	···	···	···	···
HV C II	τ	0.15	···	···	···	···	···	···
	v_{min}/v_{max}	17.5/25.0	···	···	···	···	···	···
	v_e	2.0	···	···	···	···	···	···
	T_{exec}	20000	···	···	···	···	···	···
O I	τ	···	···	···	···	···	0.20	···
	v_{min}/v_{max}	···	···	···	···	···	9.8/25.0	···
	v_e	···	···	···	···	···	1.0	···
	T_{exec}	···	···	···	···	···	20000	···
HV O I	τ	0.30	0.15	···	···	0.20	···	···
	v_{min}/v_{max}	21.0/30.0	18.0/25.0	···	···	13.0/25.0	···	···
	v_e	4.0	4.0	···	···	2.0	···	···
	T_{exec}	10000	10000	···	···	15000	···	···

Table 5.9 (cont'd)

Ion	Parameter	-17.0 d	-14.1 d	-8.5 d	-1.0 d	-0.0 d	+6.0 d	+11.4 d
Na I	τ	···	···	···	···	···	0.4	0.8
	v_{min}/v_{max}	···	···	···	···	···	9.8/25.0	8.5/25.0
	v_e	···	···	···	···	···	1.0	5.0
	T_{exec}	···	···	···	···	···	15000	15000
Mg II	τ	1.0	1.0	···	···	···	0.6	1.0
	v_{min}/v_{max}	15.0/25.0	13.9/25.0	···	···	···	10.0/25.0	8.5/25.0
	v_e	3.0	3.0	···	···	···	3.0	0.50
	T_{exec}	10000	10000	···	···	···	15000	15000
HV Mg II	τ	1.4	2.5	1.0	1.1	1.5	···	···
	v_{min}/v_{max}	20.0/35.0	16.0/30.0	14.0/25.0	13.0/25.0	13.0/25.0	···	···
	v_e	5.0	5.0	5.0	2.0	2.0	···	···
	T_{exec}	5000	5000	8000	15000	20000	···	···
Si II	τ	0.60	1.2	8.0	4.0	5.0	5.0	4.0
	v_{min}/v_{max}	15.0/25.0	13.9/25.0	12.5/25.0	11.0/15.0	11.0/15.0	9.8/25.0	8.5/25.0
	v_e	5.0	7.0	2.0	2.0	2.0	2.0	2.0
	T_{exec}	10000	10000	10000	10000	11000	11000	10000
HV Si II	τ	1.0	1.4	1.4	0.70	1.5	···	···
	v_{min}/v_{max}	23.0/35.0	20.0/28.0	14.0/25.0	14.0/25.0	13.0/25.0	···	···
	v_e	5.0	5.0	4.0	1.0	1.0	···	···
	T_{exec}	10000	10000	20000	10000	10000	···	···

Table 5.9 (cont'd)

Ion	Parameter	-17.0 d	-14.1 d	-8.5 d	-1.0 d	-0.0 d	+6.0 d	+11.4 d
Si III	τ	···	···	4.0	1.9	2.0	1.0	5.0
	v_{min}/v_{max}	···	···	13.0/25.0	11.0/25.0	11.0/25.0	9.8/25.0	8.5/25.0
	v_e	···	···	0.50	1.0	1.0	2.0	0.80
	T_{exec}	···	···	25000	5000	5000	5000	10000
HV Si III	τ	0.5	0.5	···	···	···	···	···
	v_{min}/v_{max}	19.0/25.0	16.0/25.0	···	···	···	···	···
	v_e	3.0	3.0	···	···	···	···	···
	T_{exec}	10000	10000	···	···	···	···	···
S II	τ	···	1.1	1.8	1.7	1.3	2.4	0.30
	v_{min}/v_{max}	···	13.9/25.0	12.5/25.0	11.0/25.0	11.0/25.0	9.8/25.0	8.5/25.0
	v_e	···	2.0	0.80	1.0	2.0	1.0	3.0
	T_{exec}	···	15000	10000	10000	15000	16000	20000
HV S II	τ	0.90	···	···	···	···	···	···
	v_{min}/v_{max}	18.0/25.0	···	···	···	···	···	···
	v_e	2.0	···	···	···	···	···	···
	T_{exec}	25000	···	···	···	···	···	···
Ca II	τ	18	···	15	10(11)	25	70	100
	v_{min}/v_{max}	16.0/25.0	···	12.5/25.0	11.0/15.0 (12.0/20.0)	12.0/15.0	9.8/25.0	8.5/23.0
	v_e	7.0	···	3.0	3.0(2.0)	2.0	3.0	4.0
	T_{exec}	8000	···	10000	11500	11000	20000	10000

Table 5.9 (cont'd)

Ion	Parameter	-17.0 d	-14.1 d	-8.5 d	-1.0 d	-0.0 d	+6.0 d	+11.4 d
HV Ca II	τ	30	120	12	7.0	8.0	30	···
	v_{min}/v_{max}	24.0/30.0	20.0/30.0	19.0/25.0	18.0/30.0	16.5/25.0	12.0/25.0	···
	v_e	7.0	8.0	7.0	6.0	10.0	3.0	···
	T_{exec}	8000	10000	10000	11500	10000	15000	···
	τ	35	50	50	···	···	···	···
	v_{min}/v_{max}	29.0/45.0	23.0/36.5	20.0/30.0	···	···	···	···
	v_e	7.0	7.0	5.0	···	···	···	···
	T_{exec}	8000	10000	6000	···	···	···	···
Fe II	τ	···	···	1.0	0.30	···	···	···
	v_{min}/v_{max}	···	···	13.5/25.0	11.0/15.0	···	···	···
	v_e	···	···	1.0	5.0	···	···	···
	T_{exec}	···	···	10000	11000	···	···	···
HV Fe II	τ	0.30(0.60)	0.60	···	···	0.40	0.80	3.0
	v_{min}/v_{max}	19.0/25.0(25.0/35.0)	22.0/30.0	···	···	17.0/25.0	12.0/25.0	11.0/25.0
	v_e	2.0(10.0)	10.0	···	···	1.0	2.0	2.0
	T_{exec}	10000(8000)	8000	···	···	12000	10000	10000
Fe III	τ	···	···	0.40	···	0.10	1.0	2.0
	v_{min}/v_{max}	···	···	13.0/25.0	···	12.0/25.0	9.8/25.0	8.5/25.0
	v_e	···	···	2.0	···	1.0	1.0	1.0
	T_{exec}	···	···	15000	···	10000	15000	8000

Table 5.9 (cont'd)

Ion	Parameter	-17.0 d	-14.1 d	-8.5 d	-1.0 d	-0.0 d	+6.0 d	+11.4 d
HV Fe III	τ	0.90	0.60	···	0.23	···	···	···
	v_{min}/v_{max}	20.0/25.0	16.0/25.0	···	13.0/25.0	···	···	···
	v_e	1.0	1.5	···	1.0	···	···	···
	T_{exec}	8000	8000	···	8000	···	···	···
Co II	τ	···	···	···	···	1.5	1.0	3.0
	v_{min}/v_{max}	···	···	···	···	12.0/25.0	10.0/25.0	8.5/25.0
	v_e	···	···	···	···	1.0	1.0	4.0
	T_{exec}	···	···	···	···	5000	1000	7000

Table 5.10. SN 2021fxy SYNOW Parameters

Ion	Parameter	-14.0 d	-6.0 d	+1.3 d	+3.2 d	+5.1 d	+11.0 d
	T_{bb} [K]	10500	13000	13000	12000	15000	9300
	v_{phot} [10^3 km s^{-1}]	15.0	10.8	10.0	10.0	9.0	8.0
	v_{max} [10^3 km s^{-1}]	40.0	30.0	25.0	25.0	25.0	25.0
C II	τ	0.18	...	...	...	...	...
	v_{min}/v_{max}	15.0/25.0	...	...	...	...	...
	v_e	2.0	...	...	...	...	...
	T_{exec}	17000	...	...	...	...	...
HV C II	τ	...	...	...	...	0.017	...
	v_{min}/v_{max}	...	...	...	...	17.0/25.0	...
	v_e	...	...	...	...	0.50	...
	T_{exec}	...	...	...	...	10000	...
O I	τ	...	...	...	...	0.30	...
	v_{min}/v_{max}	...	...	...	...	9.0/25.0	...
	v_e	...	...	...	...	2.0	...
	T_{exec}	...	...	...	...	10000	...
Na I	τ	...	1.0	0.50	0.50	0.20	0.30
	v_{min}/v_{max}	...	10.8/25.0	10.0/25.0	10.0/25.0	10.0/25.0	9.0/25.0
	v_e	...	0.6	2.0	2.0	3.0	6.0
	T_{exec}	...	8000	10000	10000	10000	5000

Table 5.10 (cont'd)

Ion	Parameter	-14.0 d	-6.0 d	+1.3 d	+3.2 d	+5.1 d	+11.0 d
Mg II	τ	···	···	···	···	0.60	···
	v_{min}/v_{max}	···	···	···	···	11.0/25.0	···
	v_e	···	···	···	···	2.0	···
	T_{exec}	···	···	···	···	10000	···
HV Mg II	τ	1.2	0.55	0.5	0.01	0.10	···
	v_{min}/v_{max}	18.0/30.0	15.0/30.0	12.0/25.0	13.0/25.0	18.0/25.0	···
	v_e	4.0	5.0	3.0	4.0	2.0	···
	T_{exec}	5000	15000	15000	15000	20000	···
Si II	τ	0.80	0.80	2.85	2.3	3.0	0.25
	v_{min}/v_{max}	15.0/25.0	10.8/30.0	10.0/25.0	10.0/25.0	10.0/25.0	8.0/25.0
	v_e	4.0	2.5	2.0	2.0	1.7	2.0
	T_{exec}	10000	10000	10000	10000	10000	10000
HV Si II	τ	1.6	0.15	0.10	0.05	···	2.0
	v_{min}/v_{max}	19.0/30.0	21.0/30.0	20.0/25.0	22.0/25.0	···	10.5/25.0
	v_e	5.0	0.5	3.0	3.0	···	1.2
	T_{exec}	5000	10000	8000	8000	···	20000
Si III	τ	2.3	1.5	0.80	0.50	0.10	···
	v_{min}/v_{max}	15.0/30.0	10.8/30.0	10.0/25.0	10.0/25.0	10.0/25.0	···
	v_e	3.0	1.5	1.0	1.0	1.0	···
	T_{exec}	10000	18000	5000	12000	12000	···

Table 5.10 (cont'd)

Ion	Parameter	-14.0 d	-6.0 d	+1.3 d	+3.2 d	+5.1 d	+11.0 d
HV Si III	τ	···	···	···	···	···	0.4
	v_{min}/v_{max}	···	···	···	···	···	10.0/25.0
	v_e	···	···	···	···	···	2.0
	T_{exec}	···	···	···	···	···	8000
S II	τ	1.2	0.80	1.6	4.5	2.2	0.05
	v_{min}/v_{max}	16.0/30.0	10.8/30.0	10.0/25.0	10.0/25.0	10.0/25.0	9.0/25.0
	v_e	2.0	1.5	2.0	1.0	1.0	0.5
	T_{exec}	10000	16000	28000	30000	25000	5000
Ca II	τ	15.0	1.0	17.0	21.0	15.0	80.0
	v_{min}/v_{max}	15.0/25.0	10.8/30.0	10.0/25.0	10.0/25.0	10.0/25.0	10.0/25.0
	v_e	6.0	2.0	2.0	2.0	1.0	1.0
	T_{exec}	10000	15000	15000	15000	5000	10000
HV Ca II	τ	23.0	5.0	37.0	55.0	16.0	30.0
	v_{min}/v_{max}	25.0/40.0	22.0/30.0	20.0/25.0	18.5/25.0	15.0/25.0	13.0/25.0
	v_e	10.0	5.0	2.0	1.0	2.0	4.0
	T_{exec}	12000	15000	12000	10000	10000	10000
	τ	20.0	···	···	···	22.0	10.0
	v_{min}/v_{max}	23.0/30.0	···	···	···	18.0/25.0	15.0/25.0
	v_e	10.0	···	···	···	2.0	2.0
	T_{exec}	10000	···	···	···	10000	8000

Table 5.10 (cont'd)

Ion	Parameter	-14.0 d	-6.0 d	+1.3 d	+3.2 d	+5.1 d	+11.0 d
Fe II	τ	···	0.10	···	0.30	0.70	1.0
	v_{min}/v_{max}	···	10.8/30.0	···	10.0/25.0	10.0/25.0	8.0/25.0
	v_e	···	2.0	···	2.0	2.8	2.0
	T_{exec}	···	10000	···	10000	10000	10000
HV Fe II	τ	1.0(1.5)	0.50	0.60	0.80	0.50	···
	v_{min}/v_{max}	22.0/30.0(23.5/35.0)	16.5/30.0	17.0/25.0	19.0/25.0	18.0/25.0	···
	v_e	4.0(3.0)	1.0	2.0	2.0	1.5	···
	T_{exec}	10000(9000)	10000	11000	8000	10000	···
Fe III	τ	1.5	0.30	0.10	0.10	0.50	···
	v_{min}/v_{max}	16.0/30.0	10.8/30.0	10.0/25.0	10.0/25.0	9.0/25.0	···
	v_e	2.0	4.0	2.0	2.0	2.0	···
	T_{exec}	10000	15000	10000	5000	15000	···
HV Fe III	τ	···	0.20	···	···	···	···
	v_{min}/v_{max}	···	15.0/30.0	···	···	···	···
	v_e	···	4.0	···	···	···	···
	T_{exec}	···	15000	···	···	···	···
Co II	τ	···	···	0.80	2.0	1.0	2.0
	v_{min}/v_{max}	···	···	10.0/25.0	10.0/25.0	9.0/25.0	8.0/25.0
	v_e	···	···	1.0	2.0	2.0	2.0
	T_{exec}	···	···	7000	7000	7000	7000

Table 5.10 (cont'd)

Ion	Parameter	-14.0 d	-6.0 d	+1.3 d	+3.2 d	+5.1 d	+11.0 d
Ni II	τ	···	0.50	1.0	0.50	1.0	···
	v_{min}/v_{max}	···	10.8/30.0	10.0/25.0	10.0/25.0	9.0/25.0	···
	v_e	···	3.0	3.0	3.0	2.0	···
	T_{exec}	···	4500	4500	4500	7000	···

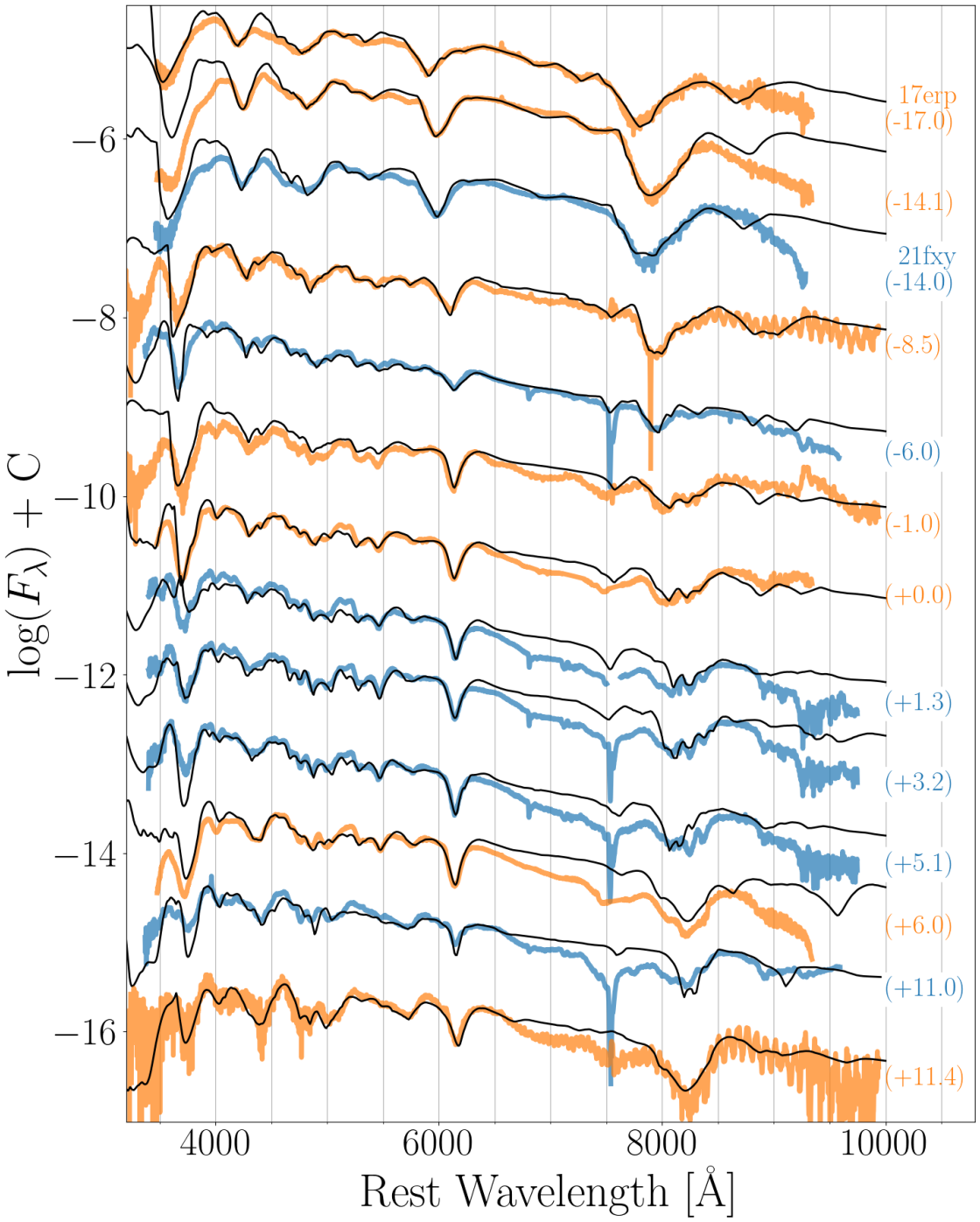

Figure 5.20: Optical sequences of SN 2017erp (orange) and SN 2021fxy (blue), with SYNOW fits overlaid in black.

CHAPTER 6

Conclusions

This work has shown the utility of both the theoretical and observational applications of radiative transfer models in differential comparisons focusing on the UV spectra of Type Ia supernovae. In Chapter 3, I simulated a suite of PHOENIX models to the $+3.4$ day UV spectrum of SN 2011fe, showing that delayed detonation models are capable of reproducing the observed UV spectra. From our best fit model, we were able to identify the ions responsible for forming all the major UV features; including the first identifications of C IV and Si IV in the far-UV spectrum of an SNe Ia. This suite of models also illustrates the the impact differences in bolometric luminosity have on the UV spectra. Models with lower bolometric luminosities show lower flux in the UV, but higher flux in the NIR relative to those models with higher bolometric luminosities. A possible cause of this variation in flux levels is the different Fe III/Fe II levels found in the outer layers of these models. Additionally, the bolometric luminosities have the ability to alter the balance of the ions responsible for forming features in the UV, causing their strengths and minimum wavelengths to shift.

Using the above models, we were able to deduce that in the case of SNe 2021fxy and 2017erp, these two related SNe Ia appear different in a manner that is consistent with a 10% difference in bolometric luminosity and not metalicity as has been previously suggested in cases of previous sets of objects with optical similarities but UV differences. When comparing SNe 2021fxy and 2017erp to the broader sample of spectrscopically normal SNe Ia with UV spectra obtained with *HST*, we find that both objects are part of an emerging class of SNe Ia with suppressed flux in the mid-UV. Investigating the connections between this suppressed flux and other observed properties of the UV spectra, we find that those SNe Ia with suppressed flux show mid-UV features that are blueshifted relative to those in non-suppressed SNe Ia. Additionally, SNe Ia with MUV suppression show strong high velocity Ca II H&K lines. The ratio of the pEWs between the high velocity component of these line to the photospheric component are correlated with the both the location of and relative flux at the minima of the MUV features.

Looking forward, we are limited by both a lack of spectral models and observations in our quest to better understand spectral formation in the ultraviolet in SNe Ia, and by extension SNe Ia themselves. Current efforts are underway to simulate more SNe Ia spectra tuned to the UV from a broad range of models across many epochs. These models will help to illuminate the underlying physics which drive spectral formation in the UV. From these spectra, we can perform differential comparisons to show the relative impact of changes in individual parameters. One application

where these comparisons will be especially helpful is determining which factors most impact the diversity of UV colors observed in SNe Ia. More advanced statistical analysis, including aspects of machine learning and artificial intelligence can potentially distinguish between models where multiple parameters are varied. If these methods prove effective, it may allow us to infer important physical parameters of the supernova from the observed spectra.

As the *Hubble Space Telescope* nears the end of its life, the astronomical community has begun to contemplate its replacement; which was deemed the highest priority in the recent Astro 2020 Decadal Survey. Further work into understanding the UV spectra of SNe Ia will guide not only the observational goals of the supernova community, but potentially even the instrumental design parameters of the next generation of large multi-purpose space telescopes. Because the UV spectra of SNe Ia have been understudied, they represent an important new window into the study of SNe Ia, one which has the potential to greatly improve our understanding of the physics that govern their observed diversity and improve our use of them as cosmological probes.

Bibliography

Anderson, J. P., González-Gaitán, S., Hamuy, M., et al. 2014, ApJ, 786, 67, doi: 10.1088/0004-637X/786/1/67

Anderson, J. P., Gutiérrez, C. P., Dessart, L., et al. 2016, A&A, 589, A110, doi: 10.1051/0004-6361/201527691

Arnett, W. D. 1982, ApJ, 253, 785, doi: 10.1086/159681

Ashall, C., Hsiao, E. Y., Hoeflich, P., et al. 2019a, ApJL, 875, L14, doi: 10.3847/2041-8213/ab1654

Ashall, C., Hoeflich, P., Hsiao, E. Y., et al. 2019b, ApJ, 878, 86, doi: 10.3847/1538-4357/ab204b

Ashall, C., Lu, J., Shappee, B. J., et al. 2022, ApJL, 932, L2, doi: 10.3847/2041-8213/ac7235

Barna, B., Pereira, T., Taubenberger, S., et al. 2021, MNRAS, 506, 415, doi: 10.1093/mnras/stab1736

Baron, E., Branch, D., Hauschildt, P. H., Filippenko, A. V., & Kirshner, R. P. 1999, ApJ, 527, 739, doi: 10.1086/308107

Baron, E., Hauschildt, P. H., Nugent, P., & Branch, D. 1996, MNRAS, 283, 297, doi: 10.1093/mnras/283.1.297

Baron, E., Höflich, P., Krisciunas, K., et al. 2012, ApJ, 753, 105, doi: 10.1088/0004-637X/753/2/105

Baron, E., Nugent, P. E., Branch, D., & Hauschildt, P. H. 2004, ApJL, 616, L91, doi: 10.1086/426506

Baron, E., Hoeflich, P., Friesen, B., et al. 2015, MNRAS, 454, 2549, doi: 10.1093/mnras/stv1951

Bellm, E. C., Kulkarni, S. R., Graham, M. J., et al. 2019, PASP, 131, 018002, doi: 10.1088/1538-3873/aaecbe

Benetti, S., Callis, E., Fraser, M., Dong, S., & Losada, I. R. 2017, Transient Name Server Classification Report, 2017-1381, 1

Benetti, S., Cappellaro, E., Mazzali, P. A., et al. 2005, ApJ, 623, 1011, doi: 10.1086/428608

Bersten, M. C., & Mazzali, P. A. 2017, in Handbook of Supernovae, ed. A. W. Alsabti & P. Murdin (Cham: Springer International Publishing), 1–13, doi: 10.1007/978-3-319-20794-0_25-1

Bloom, J. S., Kasen, D., Shen, K. J., et al. 2012, ApJL, 744, L17, doi: 10.1088/2041-8205/744/2/L17

Bongard, S., Baron, E., Smadja, G., Branch, D., & Hauschildt, P. H. 2008, ApJ, 687, 456, doi: 10.1086/590107

Bostroem, K. A., Valenti, S., Horesh, A., et al. 2019, MNRAS, 485, 5120, doi: 10.1093/mnras/stz570

Branch, D., Baron, E., Hall, N., Melakayil, M., & Parrent, J. 2005, PASP, 117, 545, doi: 10.1086/430135

Branch, D., & Venkatakrishna, K. L. 1986, ApJL, 306, L21, doi: 10.1086/184696

Branch, D., & Wheeler, J. C. 2017, Supernova Explosions (Berlin: Springer), doi: 10.1007/978-3-662-55054-0

Branch, D., Dang, L. C., Hall, N., et al. 2006, PASP, 118, 560, doi: 10.1086/502778

Brown, P. 2014, in Proceedings of Swift: 10 Years of Discovery (SWIFT 10, 125. https://arxiv.org/abs/1505.01368

Brown, P. J., Baron, E., Milne, P., Roming, P. W. A., & Wang, L. 2015, ApJ, 809, 37, doi: 10.1088/0004-637X/809/1/37

Brown, P. J., Breeveld, A. A., Holland, S., Kuin, P., & Pritchard, T. 2014, Ap&SS, 354, 89, doi: 10.1007/s10509-014-2059-8

Brown, P. J., & Crumpler, N. R. 2020, ApJ, 890, 45, doi: 10.3847/1538-4357/ab66b3

Brown, P. J., Landez, N. J., Milne, P. A., & Stritzinger, M. D. 2017, ApJ, 836, 232, doi: 10.3847/1538-4357/aa5f5a

Brown, P. J., Perry, J. M., Beeny, B. A., Milne, P. A., & Wang, X. 2018, ApJ, 867, 56, doi: 10.3847/1538-4357/aae1ad

Bulla, M., Miller, A. A., Yao, Y., et al. 2020, ApJ, 902, 48, doi: 10.3847/1538-4357/abb13c

Burke, J., Arcavi, I., Howell, D. A., et al. 2019, The Astronomer's Telegram, 12719

Burns, C., Hsiao, E., Suntzeff, N., et al. 2021, The Astronomer's Telegram, 14441, 1

Burns, C. R., Stritzinger, M., Phillips, M. M., et al. 2011, AJ, 141, 19, doi: 10.1088/0004-6256/141/1/19

—. 2014, ApJ, 789, 32, doi: 10.1088/0004-637X/789/1/32

Burns, C. R., Parent, E., Phillips, M. M., et al. 2018, ApJ, 869, 56, doi: 10.3847/1538-4357/aae51c

Burns, C. R., Ashall, C., Contreras, C., et al. 2020, ApJ, 895, 118, doi: 10.3847/1538-4357/ab8e3e

Burrow, A., Baron, E., Ashall, C., et al. 2020, ApJ, 901, 154, doi: 10.3847/1538-4357/abafa2

Buton, C., Copin, Y., Aldering, G., et al. 2013, A&A, 549, A8, doi: 10.1051/0004-6361/201219834

Childress, M. J., Filippenko, A. V., Ganeshalingam, M., & Schmidt, B. P. 2014, MNRAS, 437, 338, doi: 10.1093/mnras/stt1892

Childress, M. J., Hillier, D. J., Seitenzahl, I., et al. 2015, MNRAS, 454, 3816, doi: 10.1093/mnras/stv2173

Chu, M. R., Cikota, A., Baade, D., et al. 2022, MNRAS, 509, 6028, doi: 10.1093/mnras/stab3392

Cushing, M. C., Vacca, W. D., & Rayner, J. T. 2004, PASP, 116, 362, doi: 10.1086/382907

Dall'Ora, M., Botticella, M. T., Pumo, M. L., et al. 2014, ApJ, 787, 139, doi: 10.1088/0004-637X/787/2/139

de Jaeger, T., González-Gaitán, S., Hamuy, M., et al. 2017, ApJ, 835, 166, doi: 10.3847/1538-4357/835/2/166

de Vaucouleurs, G., de Vaucouleurs, A., Corwin, Herold G., J., et al. 1991, Third Reference Catalogue of Bright Galaxies (Berlin: Springer)

DerKacy, J. 2021, Transient Name Server Classification Report, 2021-447, 1

DerKacy, J. M., Baron, E., Branch, D., et al. 2020, ApJ, 901, 86, doi: 10.3847/1538-4357/abae67

Dessart, L., & Hillier, D. J. 2010, MNRAS, 405, 2141, doi: 10.1111/j.1365-2966.2010.16611.x

Dessart, L., Gutierrez, C. P., Hamuy, M., et al. 2014, MNRAS, 440, 1856, doi: 10.1093/mnras/stu417

Dimitriadis, G., Foley, R. J., Rest, A., et al. 2019, ApJL, 870, L1, doi: 10.3847/2041-8213/aaedb0

Domínguez, I., Höflich, P., & Straniero, O. 2001, ApJ, 557, 279, doi: 10.1086/321661

Dong, S., Katz, B., Kushnir, D., & Prieto, J. L. 2015, MNRAS, 454, L61, doi: 10.1093/mnrasl/slv129

Ellis, R. S., Sullivan, M., Nugent, P. E., et al. 2008, ApJ, 674, 51, doi: 10.1086/524981

Folatelli, G., Morrell, N., Phillips, M. M., et al. 2013, ApJ, 773, 53, doi: 10.1088/0004-637X/773/1/53

Foley, R. J., & Kirshner, R. P. 2013, ApJL, 769, L1, doi: 10.1088/2041-8205/769/1/L1

Foley, R. J., Filippenko, A. V., Kessler, R., et al. 2012, AJ, 143, 113, doi: 10.1088/0004-6256/143/5/113

Foley, R. J., Pan, Y.-C., Brown, P., et al. 2016, MNRAS, 461, 1308, doi: 10.1093/mnras/stw1440

Friesen, B., Baron, E., Parrent, J. T., et al. 2017, MNRAS, 467, 2392, doi: 10.1093/mnras/stx241

Fuller, J. 2017, MNRAS, 470, 1642, doi: 10.1093/mnras/stx1314

Gall, C., Stritzinger, M. D., Ashall, C., et al. 2018a, A&A, 611, A58, doi: 10.1051/0004-6361/201730886

Gall, E. E. E., Kotak, R., Leibundgut, B., et al. 2018b, A&A, 611, A25, doi: 10.1051/0004-6361/201731271

Gordon, K. D., Roman-Duval, J., Bot, C., et al. 2014, ApJ, 797, 85, doi: 10.1088/0004-637X/797/2/85

Goudfrooij, P., Hansen, L., Jorgensen, H. E., & Norgaard-Nielsen, H. U. 1994, A&AS, 105, 341

Graham, M. L., Foley, R. J., Zheng, W., et al. 2015, MNRAS, 446, 2073, doi: 10.1093/mnras/stu2221

Guillochon, J., Parrent, J., Kelley, L. Z., & Margutti, R. 2017, ApJ, 835, 64, doi: 10.3847/1538-4357/835/1/64

Guy, J., Astier, P., Nobili, S., Regnault, N., & Pain, R. 2005, A&A, 443, 781, doi: 10.1051/0004-6361:20053025

Hachinger, S., Mazzali, P. A., Sullivan, M., et al. 2013, MNRAS, 429, 2228, doi: 10.1093/mnras/sts492

Hauschildt, P. H., & Baron, E. 1999, Journal of Computational and Applied Mathematics, 109, 41. https://arxiv.org/abs/astro-ph/9808182

Hoeflich, P., & Khokhlov, A. 1996, ApJ, 457, 500, doi: 10.1086/176748

Hoeflich, P., Khokhlov, A. M., & Wheeler, J. C. 1995, ApJ, 444, 831, doi: 10.1086/175656

Hoeflich, P., Hsiao, E. Y., Ashall, C., et al. 2017, ApJ, 846, 58, doi: 10.3847/1538-4357/aa84b2

Höflich, P. 1995, ApJ, 443, 89, doi: 10.1086/175505

—. 2002, NewAR, 46, 475, doi: 10.1016/S1387-6473(02)00186-0

—. 2006, NuPhA, 777, 579, doi: 10.1016/j.nuclphysa.2004.12.038

Hosseinzadeh, G., Sand, D. J., Valenti, S., et al. 2017, ApJL, 845, L11, doi: 10.3847/2041-8213/aa8402

Hosseinzadeh, G., Sand, D. J., Lundqvist, P., et al. 2022, arXiv e-prints, arXiv:2205.02236. https://arxiv.org/abs/2205.02236

Hoyle, F., & Fowler, W. A. 1960, ApJ, 132, 565, doi: 10.1086/146963

Hsiao, E. Y., Marion, G. H., Phillips, M. M., et al. 2013, ApJ, 766, 72, doi: 10.1088/0004-637X/766/2/72

Iben, I., J., & Tutukov, A. V. 1984, ApJS, 54, 335, doi: 10.1086/190932

Ilkov, M., & Soker, N. 2012, MNRAS, 419, 1695, doi: 10.1111/j.1365-2966.2011.19833.x

Itagaki, K. 2021, Transient Name Server Discovery Report, 2021-785, 1

Iwamoto, K., Brachwitz, F., Nomoto, K., et al. 1999, ApJS, 125, 439, doi: 10.1086/313278

Jacobson-Galán, W. V., Margutti, R., Kilpatrick, C. D., et al. 2020, ApJ, 898, 166, doi: 10.3847/1538-4357/ab9e66

Jeffery, D. J., & Branch, D. 1990, in Supernovae, Jerusalem Winter School for Theoretical Physics, ed. J. C. Wheeler, T. Piran, & S. Weinberg, Vol. 6, 149

Jeffery, D. J., Ketchum, W., Branch, D., et al. 2007, ApJS, 171, 493, doi: 10.1086/518423

Jerkstrand, A., Fransson, C., Maguire, K., et al. 2012, A&A, 546, A28, doi: 10.1051/0004-6361/201219528

Jerkstrand, A., Smartt, S. J., Fraser, M., et al. 2014, MNRAS, 439, 3694, doi: 10.1093/mnras/stu221

Jerkstrand, A., Smartt, S. J., Sollerman, J., et al. 2015, MNRAS, 448, 2482, doi: 10.1093/mnras/stv087

Jha, S. W., Sand, D., Valenti, S., Hiramatsu, D., & Groenewald, D. 2021, Transient Name Server Classification Report, 2021-813, 1

Jiang, J.-A., Doi, M., Maeda, K., et al. 2017, Nature, 550, 80, doi: 10.1038/nature23908

Kasen, D. 2010, ApJ, 708, 1025, doi: 10.1088/0004-637X/708/2/1025

Kashi, A., & Soker, N. 2011, MNRAS, 417, 1466, doi: 10.1111/j.1365-2966.2011.19361.x

Kawabata, M., Maeda, K., Yamanaka, M., et al. 2020, ApJ, 893, 143, doi: 10.3847/1538-4357/ab8236

Kirshner, R. P., Jeffery, D. J., Leibundgut, B., et al. 1993, ApJ, 415, 589, doi: 10.1086/173188

Kochanek, C. S., Shappee, B. J., Stanek, K. Z., et al. 2017, PASP, 129, 104502, doi: 10.1088/1538-3873/aa80d9

Krisciunas, K., Contreras, C., Burns, C. R., et al. 2017, AJ, 154, 211, doi: 10.3847/1538-3881/aa8df0

Kutsuna, M., & Shigeyama, T. 2015, PASJ, 67, 54, doi: 10.1093/pasj/psv028

Lentz, E. J., Baron, E., Branch, D., Hauschildt, P. H., & Nugent, P. E. 2000, ApJ, 530, 966, doi: 10.1086/308400

Li, W., Wang, X., Van Dyk, S. D., et al. 2007, ApJ, 661, 1013, doi: 10.1086/516747

Li, W., Leaman, J., Chornock, R., et al. 2011, MNRAS, 412, 1441, doi: 10.1111/j.1365-2966.2011.18160.x

Li, W., Wang, X., Vinkó, J., et al. 2019, ApJ, 870, 12, doi: 10.3847/1538-4357/aaec74

Lin, W. L., Wang, X. F., Li, W. X., et al. 2020, MNRAS, 497, 318, doi: 10.1093/mnras/staa1918

Lira, P., Suntzeff, N. B., Phillips, M. M., et al. 1998, AJ, 115, 234, doi: 10.1086/300175

Livne, E., & Glasner, A. S. 1990, ApJ, 361, 244, doi: 10.1086/169189

—. 1991, ApJ, 370, 272, doi: 10.1086/169813

Livneh, R., & Katz, B. 2022, MNRAS, 511, 2994, doi: 10.1093/mnras/stab3787

Lothringer, J. D., Fu, G., Sing, D. K., & Barman, T. S. 2020, ApJL, 898, L14, doi: 10.3847/2041-8213/aba265

Lundqvist, P., Kundu, E., Pérez-Torres, M. A., et al. 2020, ApJ, 890, 159, doi: 10.3847/1538-4357/ab6dc6

Maeda, K., Kutsuna, M., & Shigeyama, T. 2014, ApJ, 794, 37, doi: 10.1088/0004-637X/794/1/37

Maeda, K., Benetti, S., Stritzinger, M., et al. 2010, Nature, 466, 82

Maguire, K., Sullivan, M., Ellis, R. S., et al. 2012, MNRAS, 426, 2359, doi: 10.1111/j.1365-2966.2012.21909.x

Maoz, D., Mannucci, F., & Nelemans, G. 2014, ARA&A, 52, 107, doi: 10.1146/annurev-astro-082812-141031

Marietta, E., Burrows, A., & Fryxell, B. 2000, ApJS, 128, 615, doi: 10.1086/313392

Marion, G. H., Höflich, P., Gerardy, C. L., et al. 2009, AJ, 138, 727, doi: 10.1088/0004-6256/138/3/727

Mathis, J. S. 1990, ARA&A, 28, 37, doi: 10.1146/annurev.aa.28.090190.000345

Mazzali, P. A., & Lucy, L. B. 1993, A&A, 279, 447

Mazzali, P. A., Röpke, F. K., Benetti, S., & Hillebrandt, W. 2007, Science, 315, 825

Mazzali, P. A., Sullivan, M., Hachinger, S., et al. 2014, MNRAS, 439, 1959, doi: 10.1093/mnras/stu077

McCully, C., Turner, M., Volgenau, N., et al. 2018, Lcogt/Banzai: Initial Release, 0.9.4, Zenodo, Zenodo, doi: 10.5281/zenodo.1257560

Meng, X., & Podsiadlowski, P. 2013, ApJL, 778, L35, doi: 10.1088/2041-8205/778/2/L35

Milne, P. A., Brown, P. J., Roming, P. W. A., Bufano, F., & Gehrels, N. 2013, ApJ, 779, 23, doi: 10.1088/0004-637X/779/1/23

Milne, P. A., Foley, R. J., Brown, P. J., & Narayan, G. 2015, ApJ, 803, 20, doi: 10.1088/0004-637X/803/1/20

Mitchell, R. C., Baron, E., Branch, D., et al. 2002, ApJ, 574, 293, doi: 10.1086/340928

Modjaz, M., Li, W., Butler, N., et al. 2009, ApJ, 702, 226, doi: 10.1088/0004-637X/702/1/226

Morozova, V., Piro, A. L., & Valenti, S. 2017, ApJ, 838, 28, doi: 10.3847/1538-4357/aa6251

Mould, J. R., Huchra, J. P., Freedman, W. L., et al. 2000, ApJ, 529, 786, doi: 10.1086/308304

Muthukrishna, D., Parkinson, D., & Tucker, B. E. 2019, ApJ, 885, 85, doi: 10.3847/1538-4357/ab48f4

Nakar, E., Poznanski, D., & Katz, B. 2016, ApJ, 823, 127, doi: 10.3847/0004-637X/823/2/127

Nomoto, K. 1980, in Texas Workshop on Type I Supernovae, ed. J. C. Wheeler, 164–181

Nomoto, K. 1987, ApJ, 322, 206, doi: 10.1086/165716

Nomoto, K., Sparks, W. M., Fesen, R. A., et al. 1982, Nature, 299, 803, doi: 10.1038/299803a0

Nomoto, K., Thielemann, F. K., & Yokoi, K. 1984, ApJ, 286, 644, doi: 10.1086/162639

Nomoto, K., Thielemann, F.-K., & Yokoi, K. 1984, apj, 286, 644

Nugent, P., Baron, E., Branch, D., Fisher, A., & Hauschildt, P. H. 1997, ApJ, 485, 812, doi: 10.1086/304459

Nugent, P., Phillips, M., Baron, E., Branch, D., & Hauschildt, P. 1995, ApJL, 455, L147, doi: 10.1086/309846

Nugent, P. E., Sullivan, M., Cenko, S. B., et al. 2011, Nature, 480, 344, doi: 10.1038/nature10644

Pakmor, R., Kromer, M., Röpke, F. K., et al. 2010, Nature, 463, 61, doi: 10.1038/nature08642

Pakmor, R., Kromer, M., Taubenberger, S., et al. 2012, ApJL, 747, L10, doi: 10.1088/2041-8205/747/1/L10

Pakmor, R., Kromer, M., Taubenberger, S., & Springel, V. 2013, ApJL, 770, L8, doi: 10.1088/2041-8205/770/1/L8

Pan, Y. C., Foley, R. J., Jones, D. O., Filippenko, A. V., & Kuin, N. P. M. 2020, MNRAS, 491, 5897, doi: 10.1093/mnras/stz3391

Pan, Y. C., Foley, R. J., Kromer, M., et al. 2015, MNRAS, 452, 4307, doi: 10.1093/mnras/stv1605

Parrent, J. T., Howell, D. A., Friesen, B., et al. 2012, ApJL, 752, L26, doi: 10.1088/2041-8205/752/2/L26

Passegger, V. M., Wende-von Berg, S., & Reiners, A. 2016, A&A, 587, A19, doi: 10.1051/0004-6361/201322261

Passegger, V. M., Bello-García, A., Ordieres-Meré, J., et al. 2020, A&A, 642, A22, doi: 10.1051/0004-6361/202038787

Patra, K. C., Yang, Y., Brink, T. G., et al. 2022, MNRAS, 509, 4058, doi: 10.1093/mnras/stab3136

Peacock, S., Barman, T., Shkolnik, E. L., et al. 2019, ApJ, 886, 77, doi: 10.3847/1538-4357/ab4f6f

Pellegrino, C., Howell, D. A., Sarbadhicary, S. K., et al. 2020, ApJ, 897, 159, doi: 10.3847/1538-4357/ab8e3f

Pereira, R., Thomas, R. C., Aldering, G., et al. 2013, A&A, 554, A27, doi: 10.1051/0004-6361/201221008

Perlmutter, S., Aldering, G., Goldhaber, G., et al. 1999, ApJ, 517, 565, doi: 10.1086/307221

Phillips, M. M. 1993, ApJL, 413, L105, doi: 10.1086/186970

Phillips, M. M., Lira, P., Suntzeff, N. B., et al. 1999, AJ, 118, 1766, doi: 10.1086/301032

Phillips, M. M., Simon, J. D., Morrell, N., et al. 2013, ApJ, 779, 38, doi: 10.1088/0004-637X/779/1/38

Phillips, M. M., Contreras, C., Hsiao, E. Y., et al. 2019, PASP, 131, 014001, doi: 10.1088/1538-3873/aae8bd

Pian, E., & Mazzali, P. A. 2017, in Handbook of Supernovae, ed. A. W. Alsabti & P. Murdin (Cham: Springer International Publishing), 1–16, doi: 10.1007/978-3-319-20794-0_40-1

Pignata, G., Benetti, S., Mazzali, P. A., et al. 2008, MNRAS, 388, 971, doi: 10.1111/j.1365-2966.2008.13434.x

Piro, A. L. 2012, ApJ, 759, 83, doi: 10.1088/0004-637X/759/2/83

Piro, A. L., & Morozova, V. S. 2016, ApJ, 826, 96, doi: 10.3847/0004-637X/826/1/96

Polin, A., Nugent, P., & Kasen, D. 2019, ApJ, 873, 84, doi: 10.3847/1538-4357/aafb6a

Poludnenko, A. Y., Chambers, J., Ahmed, K., Gamezo, V. N., & Taylor, B. D. 2019, Science, 366, aau7365, doi: 10.1126/science.aau7365

Poznanski, D., Prochaska, J. X., & Bloom, J. S. 2012, MNRAS, 426, 1465, doi: 10.1111/j.1365-2966.2012.21796.x

Rabinak, I., & Waxman, E. 2011, ApJ, 728, 63, doi: 10.1088/0004-637X/728/1/63

Rayner, J. T., Toomey, D. W., Onaka, P. M., et al. 2003, PASP, 115, 362, doi: 10.1086/367745

Riess, A. G., Filippenko, A. V., Challis, P., et al. 1998, AJ, 116, 1009, doi: 10.1086/300499

Riess, A. G., Yuan, W., Macri, L. M., et al. 2021, arXiv e-prints, arXiv:2112.04510. https://arxiv.org/abs/2112.04510

Rodríguez, Ó., Meza, N., Pineda-García, J., & Ramirez, M. 2021, MNRAS, 505, 1742, doi: 10.1093/mnras/stab1335

Rosswog, S., Kasen, D., Guillochon, J., & Ramirez-Ruiz, E. 2009, ApJL, 705, L128, doi: 10.1088/0004-637X/705/2/L128

Rothberg, B., & Joseph, R. D. 2006, AJ, 131, 185, doi: 10.1086/498452

Sai, H., Wang, X., Elias-Rosa, N., et al. 2022, MNRAS, doi: 10.1093/mnras/stac1525

Sauer, D. N., Mazzali, P. A., Blondin, S., et al. 2008, MNRAS, 391, 1605, doi: 10.1111/j.1365-2966.2008.14018.x

Scalzo, R. A., Childress, M., Tucker, B., et al. 2014, MNRAS, 445, 30, doi: 10.1093/mnras/stu1723

Schlafly, E. F., & Finkbeiner, D. P. 2011, ApJ, 737, 103, doi: 10.1088/0004-637X/737/2/103

Schlegel, D. J., Finkbeiner, D. P., & Davis, M. 1998, ApJ, 500, 525, doi: 10.1086/305772

Shappee, B. J., Prieto, J. L., Grupe, D., et al. 2014, ApJ, 788, 48, doi: 10.1088/0004-637X/788/1/48

Shappee, B. J., Piro, A. L., Holoien, T. W. S., et al. 2016, ApJ, 826, 144, doi: 10.3847/0004-637X/826/2/144

Shappee, B. J., Holoien, T. W. S., Drout, M. R., et al. 2019, ApJ, 870, 13, doi: 10.3847/1538-4357/aaec79

Shen, K. J., Blondin, S., Kasen, D., et al. 2021, ApJL, 909, L18, doi: 10.3847/2041-8213/abe69b

Shen, K. J., Kasen, D., Miles, B. J., & Townsley, D. M. 2018, ApJ, 854, 52, doi: 10.3847/1538-4357/aaa8de

Smartt, S. 2009a, ARA&A, 47, 63

Smartt, S. J. 2009b, ARA&A, 47, 63, doi: 10.1146/annurev-astro-082708-101737

—. 2015a, PASA, 32, e016, doi: 10.1017/pasa.2015.17

—. 2015b, PASA, 32, e016, doi: 10.1017/pasa.2015.17

Smith, N. 2014, ARA&A, 52, 487, doi: 10.1146/annurev-astro-081913-040025

Smith, N., & Arnett, W. D. 2014, ApJ, 785, 82, doi: 10.1088/0004-637X/785/2/82

Smith, N., Li, W., Filippenko, A. V., & Chornock, R. 2011, MNRAS, 412, 1522, doi: 10.1111/j.1365-2966.2011.17229.x

Soker, N., García-Berro, E., & Althaus, L. G. 2014, MNRAS, 437, L66, doi: 10.1093/mnrasl/slt142

Soker, N., Kashi, A., García-Berro, E., Torres, S., & Camacho, J. 2013, MNRAS, 431, 1541, doi: 10.1093/mnras/stt271

Soumagnac, M. T., Ofek, E. O., Gal-yam, A., et al. 2019, ApJ, 872, 141, doi: 10.3847/1538-4357/aafe84

Stritzinger, M., Hamuy, M., Suntzeff, N. B., et al. 2002, AJ, 124, 2100, doi: 10.1086/342544

Stritzinger, M. D., Anderson, J. P., Contreras, C., et al. 2018a, A&A, 609, A134, doi: 10.1051/0004-6361/201730842

Stritzinger, M. D., Shappee, B. J., Piro, A. L., et al. 2018b, ApJL, 864, L35, doi: 10.3847/2041-8213/aadd46

Stritzinger, M. D., Taddia, F., Holmbo, S., et al. 2020, A&A, 634, A21, doi: 10.1051/0004-6361/201936619

Sullivan, M., Conley, A., Howell, D. A., et al. 2010, MNRAS, 406, 782, doi: 10.1111/j.1365-2966.2010.16731.x

Teffs, J. J., Prentice, S. J., Mazzali, P. A., & Ashall, C. 2021, MNRAS, 502, 3829, doi: 10.1093/mnras/stab258

Thielemann, F. K., Nomoto, K., & Yokoi, K. 1986, A&A, 158, 17

Tody, D. 1986, in Society of Photo-Optical Instrumentation Engineers (SPIE) Conference Series, Vol. 627, Instrumentation in astronomy VI, ed. D. L. Crawford, 733, doi: 10.1117/12.968154

Tody, D. 1993, in Astronomical Society of the Pacific Conference Series, Vol. 52, Astronomical Data Analysis Software and Systems II, ed. R. J. Hanisch, R. J. V. Brissenden, & J. Barnes, 173

Tonry, J., Stalder, B., Denneau, L., et al. 2017, Transient Name Server Discovery Report, 2017-1371, 1

Tonry, J. L., Denneau, L., Heinze, A. N., et al. 2018, PASP, 130, 064505, doi: 10.1088/1538-3873/aabadf

Tucker, M. A., Shappee, B. J., & Wisniewski, J. P. 2019, ApJL, 872, L22, doi: 10.3847/2041-8213/ab0286

Tucker, M. A., Shappee, B. J., Vallely, P. J., et al. 2020, MNRAS, 493, 1044, doi: 10.1093/mnras/stz3390

Tutukov, A. V., Yungelson, L. R., & Iben, Icko, J. 1992, ApJ, 386, 197, doi: 10.1086/171005

Valenti, S., Howell, D. A., Stritzinger, M. D., et al. 2016, MNRAS, 459, 3939, doi: 10.1093/mnras/stw870

Vallely, P. J., Tucker, M. A., Shappee, B. J., et al. 2020, MNRAS, 492, 3553, doi: 10.1093/mnras/staa003

van Dokkum, P. G. 2001, PASP, 113, 1420, doi: 10.1086/323894

Walker, E. S., Hachinger, S., Mazzali, P. A., et al. 2012, MNRAS, 427, 103, doi: 10.1111/j.1365-2966.2012.21928.x

Wang, X., Wang, L., Filippenko, A. V., Zhang, T., & Zhao, X. 2013, Science, 340, 170

Wang, X., Li, W., Filippenko, A. V., et al. 2009, ApJ, 697, 380, doi: 10.1088/0004-637X/697/1/380

Wang, X., Wang, L., Filippenko, A. V., et al. 2012, ApJ, 749, 126, doi: 10.1088/0004-637X/749/2/126

Webbink, R. F. 1984, ApJ, 277, 355, doi: 10.1086/161701

Whelan, J., & Iben, Icko, J. 1973, ApJ, 186, 1007, doi: 10.1086/152565

Woosley, S. E., & Weaver, T. A. 1994, ApJ, 423, 371, doi: 10.1086/173813

Xiang, D., Wang, X., Mo, J., et al. 2019, ApJ, 871, 176, doi: 10.3847/1538-4357/aaf8b0

Yanchulova Merica-Jones, P., Sandstrom, K. M., Johnson, L. C., et al. 2021, ApJ, 907, 50, doi: 10.3847/1538-4357/abc48b

Yaron, O., Perley, D. A., Gal-Yam, A., et al. 2017, Nature Physics, 13, 510, doi: 10.1038/nphys4025

Yoon, S. C., & Langer, N. 2004, A&A, 419, 645, doi: 10.1051/0004-6361:20035823

Zhang, J., Wang, X., József, V., et al. 2020, MNRAS, 498, 84, doi: 10.1093/mnras/staa2273

Zhang, X., Wang, X., Sai, H., et al. 2022a, MNRAS, 509, 2013, doi: 10.1093/mnras/stab3007

—. 2022b, MNRAS, 513, 4556, doi: 10.1093/mnras/stac1166

CHAPTER A

Work in Progress: SN 2019ein

SN 2019ein is a SN Ia, notable for its broad lines at high velocities throughout its photospheric phase (the first ~ 40 days after explosion). What makes these high velocity lines interesting is that their emission peaks are also blue shifted relative to the rest wavelengths, as seen in Figure A.1. The ability to apply a simple Doppler shift to the spectra of SN 2011fe to reproduce the observed peculiarities in SN 2019ein, suggests that the two SNe have very similar ejecta. We seek to explore these similarities and determine the physical mechanism that causes the differences between these two supernovae in the hope that they can provide insight into any potential variations in the underlying progenitors that may lead to this behavior.

If we use the velocity of the Si II $\lambda 6355$ line as a proxy for the photospheric velocity, we see that SN 2019ein does not have significantly different velocities to other Ia-BL around maximum light. However, at early times and the later epochs of the photospheric phase, SN 2019ein is faster than both SN 2011fe and other Ia-BL.

Using the same model as Baron et al. (2015) and DerKacy et al. (2020), we plan to simulate the spectra of SN 2011fe at a variety of epochs to study the conditions in the ejecta as a function of time. Similarly, for SN 2019ein we can generate synthetic spectra from the model of Baron et al. (2012) previously used to model SN 2001ay, another SN Ia-BL. Once we have a suite of time series models for both our CN and BL objects, we can compare the properties of the ejecta to determine which ones are responsible for the observed blue-shift in the spectral features.

`SYNOW` fits to the spectra of SNe 2011fe and 2019ein can direct us towards some of the important properties to examine in our `PHOENIX` models. Using the parameters from Parrent et al. (2012) to generate `SYNOW` spectra of SN 2011fe, we compare them to those generated for SN 2019ein. We find that while a simple Doppler shift is able to produce good matches between the observed spectra, it is not able to do so with our simple model spectra, assuming both features are photospheric (Z. Yarbrough et al., in prep). Instead, our fits to SNe 2011fe and 2019ein reveal that at early times, when the strength of this Doppler shift effect is strongest, SN 2019ein has multiple detached components, which produce a line profile similar in shape to that of SN 2011fe when it is Doppler shifted. The presence of multiple detached components in SN 2019ein suggests that these lines are forming in a high density shell with similar composition to that of SN 2011fe.

Figure A.3 shows the density structures of the two models used to simulate SNe 2011fe and 2019ein. The only significant difference between the two models is the density enhancement in the

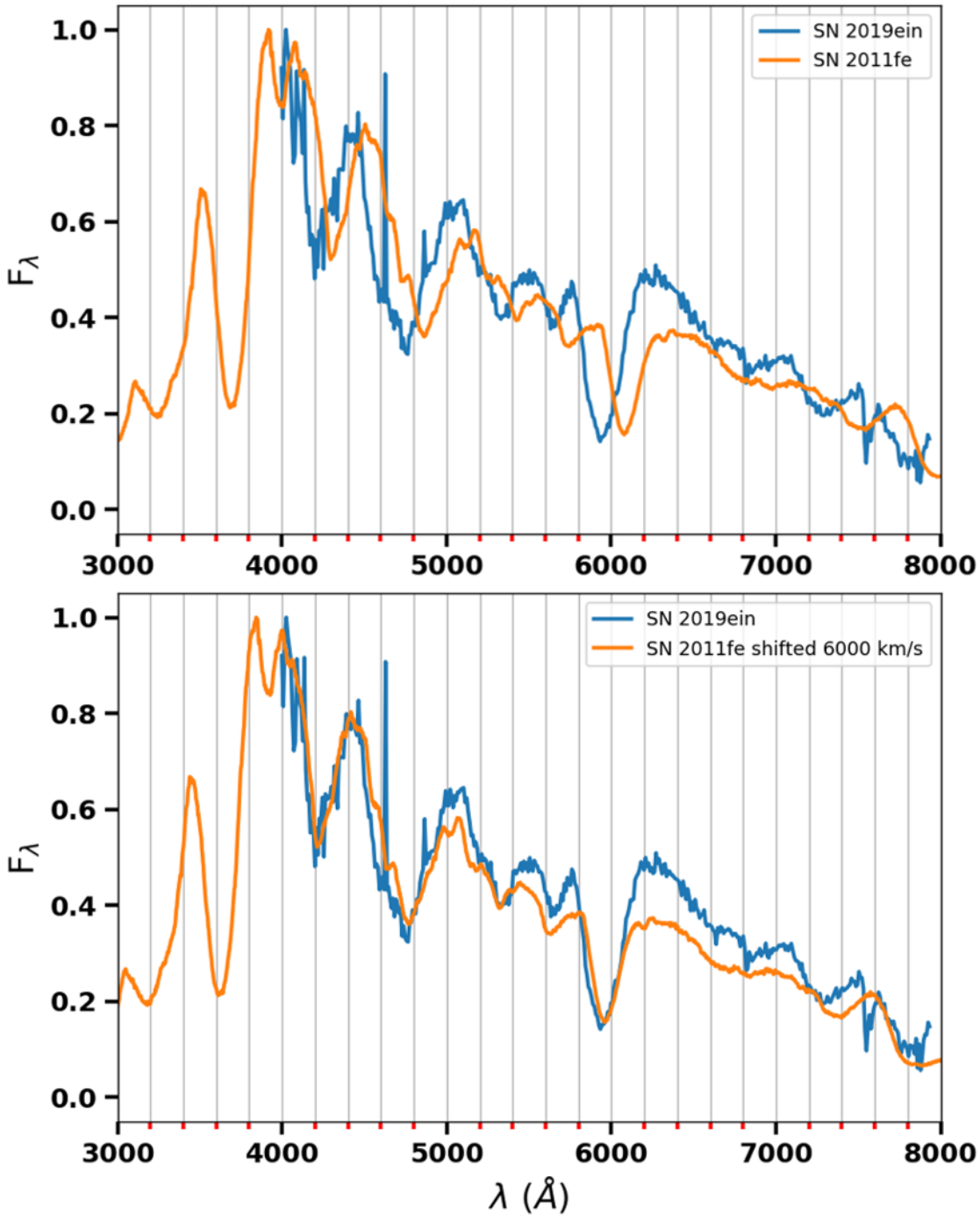

Figure A.1: *Top Panel:* Spectra of SNe 2011fe and 2019ein at similar epochs corrected to their rest wavelengths. *Bottom Panel:* The same spectra from the top panel, with a 6000 km s^{-1} Doppler shift applied to the SN 2011fe spectrum.

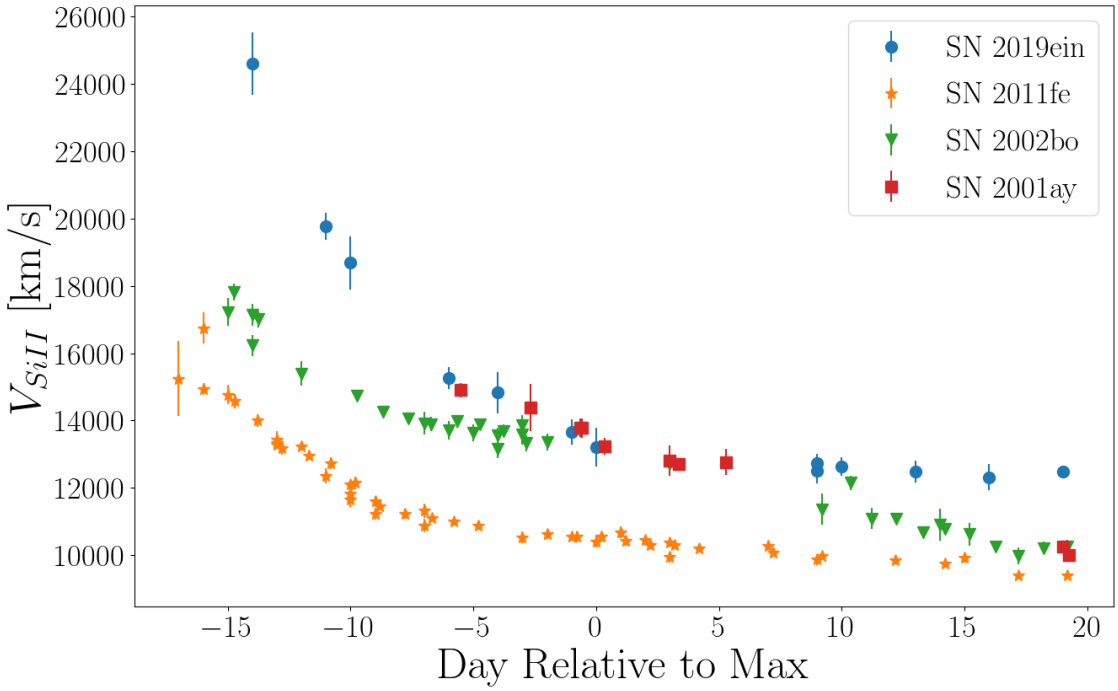

Figure A.2: Si II λ6355 velocities in SNe Ia-BL 2001ay, 2002bo, and 2019ein compared to those of SN Ia-CN 2011fe. All three of SNe 2001ay, 2002bo, and 2019ein show broad, high velocity features in their pre-max and max light spectra.

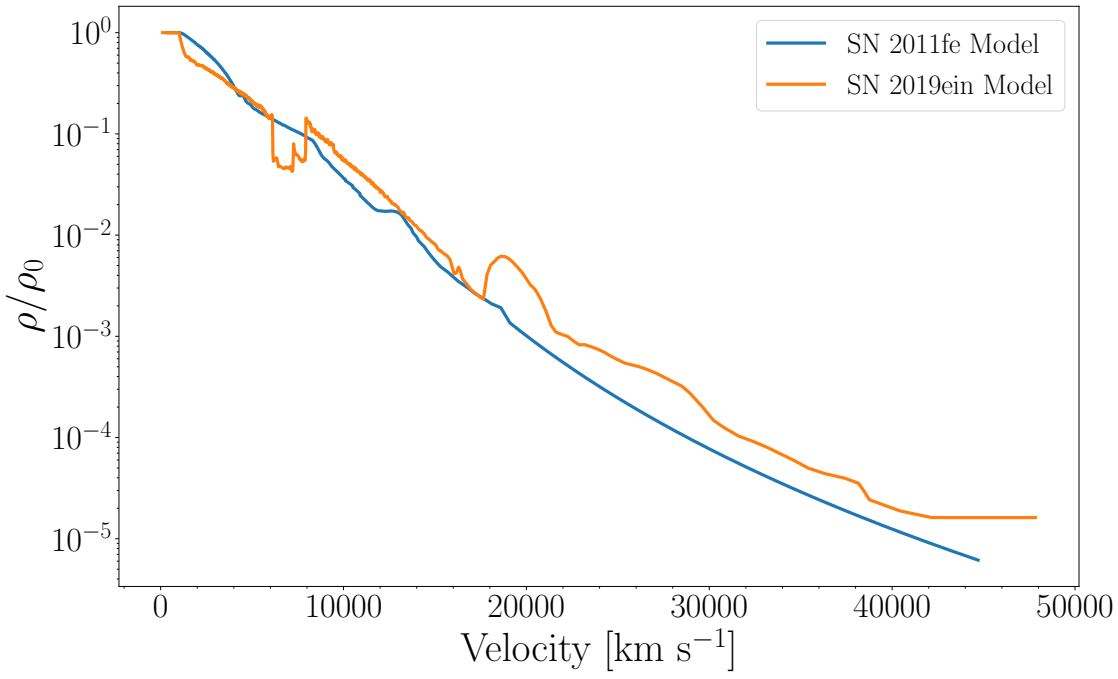

Figure A.3: Density profiles of the hydrodynamic models of SNe 2011fe and 2019ein.

PDD model, corresponding to the dense shell. Preliminary results are compared to the observed spectra of SN 2019ein taken at APO during May 2019 in Figure A.4. While the models show general agreement with the spectra of both SNe at day 12, both SNe are not currently reproduced at day 34. However, unlike the models of DerKacy et al. (2020), we have not yet completed our survey of luminosity space in order to determine which values are necessary to achieve good fits. Further modeling at other epochs from the time of explosion to the disappearance of the Si II lines from the spectra are currently underway. Once our full time series of spectral models is complete, only then can we begin to analyze the properties of the line forming regions in the ejecta to see if we can reproduce the observed Doppler shift, and what physical mechanisms are responsible.

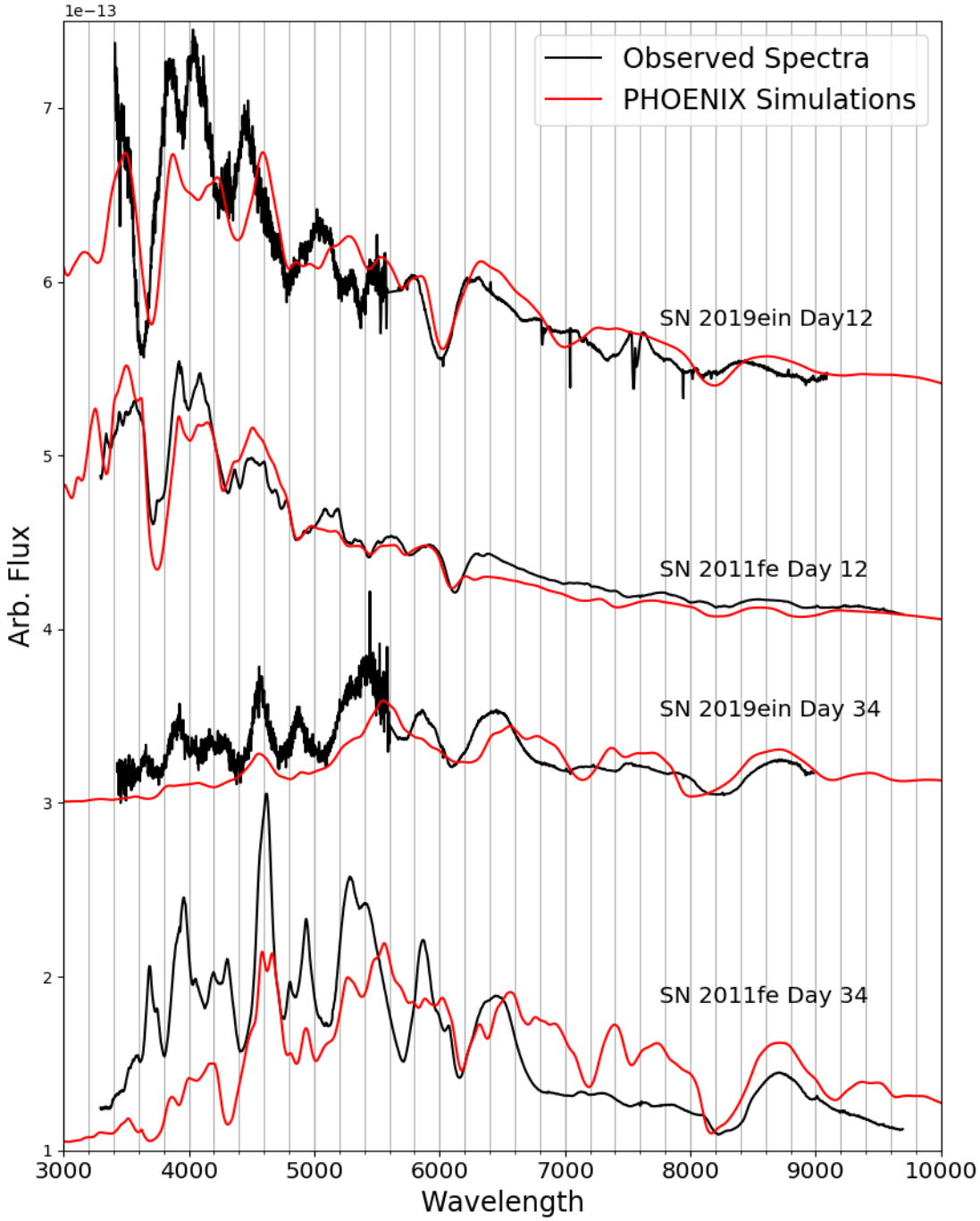

Figure A.4: Preliminary PHOENIX models of SNe 2011fe and 2019ein compared to observations at the same epoch.